NASA Technical Paper 1070

Computation of Transonic Boattail Flow With Separation

Richard G. Wilmoth

DECEMBER 1977

NASA

N#5 1,60: 1070

NASA Technical Paper 1070

Computation of Transonic Boattail Flow With Separation

Richard G. Wilmoth
Langley Research Center
Hampton, Virginia

SUMMARY

The relaxation procedure of South and Jameson for the full potential transonic flow equation has been coupled to a modified Reshotko-Tucker integral boundary-layer technique with an empirical model for separated flow. The viscous and inviscid flows are solved iteratively until convergence is obtained. This iterative method has been applied to the subsonic and transonic flow over a series of axisymmetric circular-arc boattails with solid jet plume simulators. Comparisons of theoretical and experimental surface pressures and boattail drag are presented over a free-stream Mach number range of 0.40 to 0.96. Measured and predicted pressures agree well for Mach numbers below 0.90. This numerical method correctly predicts the qualitative variation of boattail drag with free-stream Mach number and boattail angle well into the region of transonic drag rise although it significantly underpredicts the absolute drag levels. For separated flows, the empirical discriminating streamline model gives good results up to a free-stream Mach number of about 0.90 and allows reasonable predictions for shock-induced separation if the proper separation location and separation turning angle are known.

INTRODUCTION

Current analytical methods for predicting nozzle afterbody flows generally employ what is usually called the patched viscous-inviscid technique. For example, Reubush and Putnam (ref. 1) combine iteratively a conventional boundary-layer technique with a linearized potential flow computation to account for the viscous-inviscid interaction. In spite of the relative complexity of the flow even for isolated boattails, these approximate methods successfully predict the qualitative trends of boattail drag with Mach number and Reynolds number. However, the use of a linearized potential flow analysis limits the prediction capability to fully subsonic flows. The need to extend this capability to transonic speeds is prompted by the current interest in afterbody performance at supercritical speeds for which wall-interference-free wind-tunnel results are difficult to obtain.

Recently, South and Jameson (ref. 2) have developed a numerical procedure for solving the full potential equation with exact boundary conditions for inviscid, transonic flow. This procedure permits compressibility effects to be fully included and thus allows the extension of patched viscous-inviscid predictions into the transonic regime. A number of similar approaches for coupling this inviscid technique with a boundary-layer procedure have been reported recently (refs. 3 to 7). These approaches differ

principally in the method of coupling the viscous and inviscid techniques and in the particular boundary-layer solution procedure used. However, due to the difficulty in modeling shock-induced separation, only very limited calculations have been reported at transonic speeds (mixed subsonic-supersonic flow) with separated flow regions. At supersonic speeds, numerical solutions to the Navier-Stokes equations have been obtained by Holst (ref. 8) and agree well with the experimental data of Reubush (ref. 9). Holst's solutions required from 1 to 2.5 hours on the Control Data Cyber 175 computer; with his procedure, subsonic cases would probably require even greater computer time since the computational boundaries must be placed at a larger distance from the body. Thus, a current need exists for prediction methods, even if approximate, which have smaller computer time requirements. When properly coupled to include boundary-layer thickness, separation, and jet plume effects, the full potential inviscid solution should provide a valid engineering method for predicting boattail drag at transonic speeds.

The present study combines the relaxation procedure of South and Jameson (ref. 2) for the full potential flow equation with the turbulent boundary-layer integral method of reference 10. It then determines the accuracy of this approximate viscous-inviscid iterative technique for predicting boattail pressures and drag on axisymmetric nozzles at subsonic and transonic flow speeds. Effects of flow separation were included by means of an empirical model of the separation bubble. Results from the present numerical method are compared with surface pressures and boattail drag obtained experimentally by Reubush (ref. 9) for several circular-arc boattail configurations with solid plume simulators. Calculations were performed over a free-stream Mach number range of 0.40 to 0.96 under conditions ranging from fully attached flow to largely separated flow. Comparisons with the experimental results and with inviscid theory are given to show explicitly the magnitude of the viscous effects. The onset of shock-induced separation is also examined within the framework of the empirical separation model. Finally, the sensitivity of the numerical solution to grid size is discussed.

SYMBOLS

A boattail cross-sectional area, cm^2

A_{max} model maximum cross-sectional area, cm^2

C_D boattail-pressure drag coefficient, $\dfrac{1}{A_{max}} \displaystyle\int_0^x C_p \, dA$

$C_{D,\beta}$ total boattail-pressure drag coefficient, $\dfrac{1}{A_{max}} \displaystyle\int_0^{x_l} C_p \, dA$

C_p static-pressure coefficient, $\dfrac{p - p_\infty}{q_\infty}$

C_p^* static-pressure coefficient corresponding to local sonic flow

d_b nozzle base diameter, cm

d_m model maximum diameter, cm

L length of forebody from nose to start of boattail, cm

M Mach number

p static pressure, Pa

q dynamic pressure, Pa

R_c radius of curvature of circular-arc boattail, cm

S,R indicate separation and reattachment points in figures

x axial distance aft from start of boattail, cm

β_c boattail chord angle, deg

δ^* boundary-layer displacement thickness, cm

θ_s angle between body surface and discriminating streamline at separation, deg

ξ, η inviscid computational coordinate system

Subscripts:

l end of boattail

r reattachment

s separation

∞ free stream

3

NUMERICAL METHOD

The numerical method used in this study is an extension to transonic speeds of the subsonic viscous-inviscid iterative method of Reubush and Putnam (ref. 1). Figure 1 illustrates the basic model of the afterbody flow field, and table I gives the various geometrical parameters of the configurations for which the calculations were made. These configurations are the same as the circular-arc boattails for which surface pressures were measured experimentally by Reubush (ref. 9). The external flow field is assumed to be inviscid, and the viscous layer is taken into account by adding to the body shape the boundary-layer displacement thickness δ^*. The method iterates between the external flow and viscous solutions until convergence is achieved. Even in the presence of boundary-layer separation, this approximate technique appears to be a viable one as demonstrated by the good agreement between theory and experiment obtained by Bauer, et al. (ref. 11) and Bavitz (ref. 12) for the flow over various supercritical airfoils. In the present technique, the separation bubble is replaced by an empirically derived conical discriminating streamline which is treated as a solid boundary by both the inviscid and boundary-layer solution methods. Since the study is limited to afterbodies with solid plume simulators, the jet plume is represented as a solid cylinder extending downstream to infinity. In the experiments conducted by Reubush, the solid cylinder had a finite length; however, this effect has been shown by Putnam and Abeyounis (ref. 13) to have only a small effect on the boattail pressure distribution.

Inviscid Flow Solution

For the inviscid external flow, the relaxation technique for the full potential flow equation developed by South and Jameson (ref. 2) is used. The computer program which utilizes this technique is referred to as RAXBOD, and its usage is described by Keller and South in reference 14. For bodies with an open or finite base, this technique employs a body-normal coordinate system (ξ, η) on the forebody up to the first horizontal tangent and a sheared cylindrical coordinate system aft of this point. A typical computational grid in physical space for a cone-cylinder forebody $\left(L/d_m = 8\right)$ with a circular-arc boattail is shown in figure 2. This forebody shape is the same as that used by Reubush (ref. 9). For this study, the initial grid was 39 by 20 grid points in the streamwise and normal directions, respectively. A single grid-halving then resulted in a final grid size of 77 by 39. This grid extends to infinity in physical space and is mapped onto a finite rectangular computational plane by a set of coordinate stretching functions described in reference 14. These functions provide considerable flexibility in obtaining the desired distribution of grid points in the flow field. For example, smaller grid spacing may be used in a region where better accuracy is desired such as, for this study, on the boattail. However, the grid aspect ratio $\Delta\xi/\Delta\eta$ varies throughout the flow field (see fig. 2). This

4

variation can result in computational stability problems in the vicinity of shocks for the coupled viscous-inviscid solution. The sensitivity of the solution to various grid parameters is discussed in this report.

The computer program, RAXBOD, was modified slightly for coupling with the boundary-layer solution by using simple numerical differencing rather than the original cubic spline curve fits to obtain the derivatives of the body coordinates. The modified program generally gave results identical to the original program but was found to be less sensitive to large boundary-layer displacement thickness changes that occasionally tended to cause the inviscid solution to diverge.

Viscous Flow Solution

The boundary-layer displacement thickness is obtained from the integral form of the boundary-layer equations for turbulent flow given by Reshotko and Tucker (ref. 15). The von Kármán momentum integral equation and the moment-of-momentum integral equation are solved simultaneously for the momentum thickness and for the incompressible shape factor with a Ludwieg-Tillmann relation for the skin-friction coefficient. The shear integral in the moment-of-momentum equation is the modified form given in reference 10. The modified form allows a wider range of shape factors than that allowed by the simple relation for the shear integral given by Reshotko and Tucker (ref. 15). A Runge-Kutta procedure is used to integrate the set of ordinary differential equations. The integration step size was the same as the streamwise grid size on the body surface used in the inviscid calculation. The details of the Runge-Kutta procedure and the modifications to the shear integral are given in reference 10.

Viscous-Inviscid Iteration

Since the boundary-layer solution technique requires that the pressure distribution be specified, an inviscid calculation is first performed on the original body shape. The resulting inviscid pressure distribution is then specified to the boundary-layer solution method for calculating the displacement thickness distribution along the body. An underrelaxation technique whereby the calculated displacement thicknesses for the current and previous boundary-layer computations are averaged and added to the body radius is used to correct the body geometry. (Although the boundary-layer integration is performed in the streamwise direction and thus the displacement thickness is normal to the local body surface, the error created by adding the displacement thickness to the body radius is negligible in the present study because of the small body slopes encountered.) The corrected body geometry is then specified for the inviscid flow solution method and the entire process repeated until convergence is achieved. A total of 15 iterations (including inviscid grid refinements) between the inviscid and boundary-layer solutions

was generally found to be sufficient for convergence (less than 0.1-percent change between successive iterations) on both the displacement thickness and surface pressure distributions. The grid-halving for the inviscid calculation is performed between the fifth and sixth boundary-layer computations. A total of 20 iterations were used within the relaxation solution to obtain the inviscid pressure distribution needed for each boundary-layer computation. Calculations made with larger numbers of inviscid iterations indicate that 20 inviscid iterations between each boundary-layer computation give a boattail drag generally within 2 percent of its converged value.

SEPARATED FLOW APPROXIMATION

The boundary-layer procedure used in the present analysis does not allow for reverse flow regions of separation. Therefore, the reverse flow region must be handled in a manner different from the attached boundary-layer procedure. This is usually accomplished by determining a streamline which divides the reverse flow region from the outer boundary-layer flow region and across which there is no mass flow. This streamline can then be treated as an effective solid boundary which models the separation bubble. Alber, et al. (ref. 16) have applied the concept of a discriminating (or dividing) streamline to obtain good agreement between theory and experiment for transonic, separated flows over two-dimensional shapes. Thus the application of this concept to axisymmetric, transonic flows seems justified. The following sections describe the method by which these discriminating streamline shapes were estimated for use in the present study and discuss the validity of these estimates for shock-induced separation.

Discriminating Streamline Estimate

Presz (ref. 17) modeled the discriminating streamline as a conical surface which diverges from the afterbody surface at an angle θ_s. His control volume analysis between the separation point x_s and the reattachment point x_r showed this angle to depend primarily on the local Mach number at the separation point. For their subsonic calculations, Reubush and Putnam (ref. 1) used a straight line fit to the experimental data of Presz together with the empirical separation location method of Page (ref. 18) to determine this angle. In principle, the same approach could be used in the present method; that is, the values of x_s and θ_s could be calculated from the results of the inviscid calculation using the same empirical separation models. However, these empirical models do not account for shock-interaction effects encountered at transonic speeds. Furthermore, the need to find two additional parameters can cause convergence problems since the viscous-inviscid interactions are quite large at transonic speeds. Thus the calculations are simplified considerably if x_s and θ_s are taken as a priori and held constant during the viscous-inviscid iterations. Since no adequate theory currently exists

6

for making such a priori predictions, x_s and θ_s had to be deduced from available experimental data.

The separation location x_s was taken from oil-flow studies obtained by Abeyounis (ref. 19) on the same circular-arc boattails listed in table I. The reattachment point x_r was then assumed to occur at the point of maximum pressure on the solid simulator. This assumption seems reasonable in view of the experimental data of references 16 and 17. Figure 3 illustrates a typical experimental pressure distribution obtained by Reubush (ref. 9) including pressures measured on the solid simulator. For the given boattail geometry, the discriminating streamline separation angle was determined by connecting the separation and reattachment points as shown in figure 3. For comparison, the streamline determined using the empirical data of Presz (ref. 17) is also shown. Note that reattachment for the Presz streamline occurs well downstream of the point of maximum pressure in sharp contrast to the experimental results of Alber, et al. (ref. 16) who found reattachment to occur slightly upstream of the maximum pressure point.

The variation of the present empirical results for θ_s with the local Mach number at separation is shown in figure 4 for the four configurations analyzed. The range of data contained in reference 17 is given for comparison. The present results show good agreement with Presz's data for $M_s < 0.80$ for configurations 2 and 6. However, configuration 1 indicates a more rapid decrease in θ_s with increasing M_s than the decrease reported in reference 17. The large turning angles obtained for configuration 4 reflect the error in determining θ_s in the manner shown in figure 3 for the smaller boattail angles since the extent of separation is very small for both configurations 4 and 6. However, the most significant conclusion to be drawn from these results is that, for all configurations analyzed, θ_s approaches a value of about 3° as M_s approaches unity. This value is in reasonable agreement with the turning angle through an oblique shock indicated by the dashed line in figure 4 which was calculated using the pressure jump required to satisfy the Page (ref. 18) separation criterion $\left(\text{in ref. 18, } \Delta C_p = 0.38\right.$ between the minimum pressure location and the separation point; C_p based on local dynamic pressure $\left.\right)$.

A comparison of some typical experimental pressure distributions with the theoretical prediction obtained using experimentally derived x_s and θ_s is shown in figure 5. Also given are the predictions obtained (1) using the experimental x_s and Presz's predicted θ_s and (2) using x_s predicted by Page's method and θ_s predicted by Presz's method. These results are for configuration 1 which had the most extensive separated region of any of the configurations analyzed. Obviously, the use of solely experimental x_s and θ_s in describing the separated region gives much better agreement with the measured pressures than either of the other methods. The good agreement even up to $M_\infty = 0.90$ achieved by using experimental x_s and θ_s indicates that the basic con-

7

cept of the existence of a discriminating streamline is reasonably valid even when shock interaction effects are present. However, using the larger separation angles predicted by Presz tends to move the expansion-compression region forward on the boattail. Using Page's separation criterion together with the predicted θ_S does not improve the agreement with experiment significantly; thus, the flow is probably more sensitive to θ_S than to x_S. An improvement in the results obtained by combining Page's and Presz's separation predictions might be achieved with additional iterations on both x_S and θ_S. The results of this combined method (see fig. 5) were obtained by updating the x_S and θ_S predictions only at the beginning of each grid refinement. However, the Page criterion did not predict separation at all the free-stream conditions for which separation was observed experimentally by Abeyounis. As a result, the separation and reattachment locations deduced from experiment were used in the calculations presented in the remainder of this report.

Shock-Induced Separation

The transition to shock-induced separation is evident from the sharp drop in discriminating streamline turning angle as the flow ahead of separation approaches supersonic speeds (see fig. 4). Typical regions of supersonic flow determined by RAXBOD for the configurations studied are shown in figure 6. Note that a region of supersonic flow extends over a significant portion of the boattail and ends at a point where the flow generally separates. At sufficiently high transonic speeds a nearly normal shock will form along the rear sonic line of this supersonic region. (Although a well-defined shock wave may not be present at all transonic speeds, the term "shock" will be used in this paper to denote the rear sonic line for all cases which have a supersonic bubble on the boattail.) The variations in the predicted shock location and the experimental separation location with free-stream Mach number are shown in figure 7 for configuration 1. For $M_\infty \gtrsim 0.91$, the shock region merges with the separation region and separation occurs upstream of the predicted shock location indicating a transition to shock-induced separation. The two distinct types of shock and boundary-layer interaction are illustrated by the flow sketches inserted in this figure. The fact that the predicted shock location lies downstream of the separation point for $M_\infty \gtrsim 0.91$ does not agree with the experimental results of reference 16 where the separation point was found to coincide with the shock location for shock-induced separation. However, the predicted shock locations given in figure 7 were obtained with a relatively coarse computational grid and thus could not be resolved with great accuracy. It is anticipated that the use of a finer grid in this region (which unfortunately was not possible in the present case because of stability problems with the viscous-inviscid interaction) would move the predicted shock locations upstream in better agreement with the results of reference 16. Thus, the transition to shock-induced separation shown in figure 7 should be viewed only as a qualitative picture.

8

Strong shock and boundary-layer interactions would obviously have a significant effect on the external flow, and approximating the discriminating streamline as a straight line between separation and reattachment for shock-induced separation is indeed subject to question. The sensitivity of the predicted pressure and cumulative drag distributions to the shape of the discriminating streamline is shown in figure 8. Here the results calculated with a modified discriminating streamline shape are compared with both experiment and the result calculated with a straight discriminating streamline. For both sets of calculated results, x_s and x_r were held constant. The modified discriminating streamline shape consists simply of extending the streamline at the angle predicted by Presz to the end of the boattail and then fitting a straight line to the experimental reattachment point. The resulting streamline thus consists of two straight-line segments (actually conical in three dimensions) as shown by the insert in figure 8. (The modified streamline is exaggerated for clarity in the sketch.) The rationale for this shape was based on the idea that the longitudinal pressure gradient at the start of the separated region tends to promote mixing and thus increases the initial separation angle. The significantly improved agreement with experiment shown in the figure indicates that the modified streamline is at least qualitatively correct. Thus, a more rigorous treatment of the longitudinal pressure gradient in a control volume analysis (like Presz's, ref. 17) should result in better predictions for shock-induced separation.

RESULTS AND DISCUSSION

Comparison of Theory and Experiment

Afterbody pressure distributions throughout the interaction region and cumulative pressure drag distributions up to the boattail-simulator juncture are presented in figures 9 to 13 for the five configurations analyzed. Calculations were made over the free-stream Mach number range from 0.40 to 0.96 provided experimental separation location was known from reference 19. The cumulative drag is shown since it indicates where the errors arise in the prediction of total boattail drag. For those cases with separated flow, the experimentally determined separation and reattachment points are indicated in the figures by the symbols S and R. The results are presented in order of increasing boattail angle with a corresponding increase in the extent of separation. Configuration 3 (fig. 9) did not indicate any separation over the free-stream Mach number range analyzed while configuration 1 (fig. 13) showed separation over the entire Mach number range.

The results in figures 9 to 13 show generally very good agreement between theoretical and experimental pressures up to a Mach number of about 0.90. For attached flow conditions the calculated pressures are somewhat higher than the measured values near the end of the boattail, and the disagreement is most pronounced for configurations 6

9

and 4 (figs. 10 and 11, respectively). Yaros (ref. 5) obtained a similar result for configuration 3 at Mach numbers of 0.40, 0.70, and 0.96.

For separated flow conditions, theory and experiment also agree quite well except near the end of the boattail. Addition of the discriminating streamline tends to smooth the boattail-simulator discontinuity and thereby lower the pressures although the calculated pressures in the separated region are still somewhat higher than the measured values. Comparable results were obtained by Yaeger (ref. 7) for configurations 1 and 2 at Mach numbers of 0.40 and 0.70. The generally good agreement for the location of the maximum pressure on the solid simulator indicates that the assumption that reattachment occurs at this point is reasonable. Above a Mach number of 0.90, significant disagreement is seen in the region of minimum pressure for both attached and separated flows due to shock and boundary-layer interactions. Flow predictions in regions of extensive separation at these higher Mach numbers were quite sensitive both to the location of the separation point and to the angle of the discriminating streamline and generally give significantly higher pressures than the experiments (see figs. 12(c) and 12(d) and 13(c) and 13(d)).

The predicted cumulative drag distributions shown in figures 9 to 13 are in good agreement with experiment in almost every case up to the point of maximum drag except at the higher Mach numbers where the cumulative drag continues to increase to the end of the boattail. The predicted curve, however, always drops off too rapidly near the end of the boattail, and significant underprediction of the total drag results. The errors in the pressures described in the previous paragraph all seem to be additive because they all lead to underprediction of the drag. Even in those cases (subsonic, attached flow) where the pressures agree within the experimental uncertainties, the error in predicted pressures is toward higher values and thus lower drag.

Despite these discrepancies, the viscous-inviscid method predicts the correct qualitative behavior for the total pressure-drag variation with Mach number. A comparison of theory and experiment is given in figure 14. Although it underpredicts the absolute drag levels, the full potential transonic theory correctly predicts the location and generally the shape of the transonic drag rise. Also, the increase in drag with increasing boattail angle is correctly predicted at Mach numbers greater than 0.90. At Mach numbers below 0.90, both the theory and experiment show little variation with boattail angle except for configuration 1 which had extensive separation at all Mach numbers. The experimental drag values plotted in figure 14 were obtained by integrating the experimental pressure distributions in a slightly different manner than that used in reference 9 and thus are generally slightly higher than those reported in reference 9.

It is also observed that obtaining drag coefficients by integration of the pressure distributions over the finite boattail length tends to magnify the error in the total boattail

drag coefficient. That is, the total boattail drag coefficient is essentially the difference between a region of drag $\left(\text{negative } C_p\right)$ and a region of thrust $\left(\text{positive } C_p\right)$ both of which are large positive numbers. Thus a small error in either region may lead to a large error in the difference.

Viscous-Inviscid Interactions

The most significant effects of viscous-inviscid interaction on the external flow were found in regions of (1) shocks, (2) boattail-simulator juncture, and (3) separated flow. For attached flow, the first two effects may be seen more clearly in figure 15 where the calculated viscous-inviscid result for $M_\infty = 0.96$ is compared with experiment and with that for a purely inviscid calculation. The difference between the two theoretical curves shows the large effect of the shock and boundary-layer interaction on the recompression of the flow. As noted before, the viscous-inviscid theory generally predicts higher pressures in this region than those measured experimentally. These higher pressures are believed to result from the use of nonconservative differencing in the inviscid solution which causes a spurious mass source at the shock and results in a displacement of the surface streamline away from the body downstream of the shock (see ref. 20). When coupled with the viscous solution, this streamline displacement tends to overcompensate for boundary-layer displacement effects, and a weakening of the expansion and/or recompression of the flow results. In fact, the inviscid calculation alone gives better agreement with experiment in this region than does the viscous-inviscid method. Therefore, conservative differencing may be necessary in viscous-inviscid solutions with strong shocks. This conclusion may also apply to separated flows although it is difficult to distinguish between the effects due to nonconservative differencing and effects due to inaccuracies in the separation model.

The effect of "smoothing" the rear stagnation point at the boattail-simulator juncture is also shown in figure 15. Although the viscous-inviscid method overpredicts the pressures in this region, substantially improved agreement with experiment is obtained over the inviscid result. The overprediction of the pressures results because the discontinuity is not completely canceled by the addition of the boundary layer. The successful marching of the boundary-layer technique through a region of such relatively large displacement thicknesses $\left(\delta^*/d_m \approx 0.08\right.$ at the boattail-simulator juncture for the case shown in fig. 15$\right)$ depends on the numerical "smoothing" of the inviscid pressure distribution due to the relatively coarse grid. Thus, to cancel the discontinuity exactly would require special treatment of this region. For separated flows, the boattail-simulator juncture is "hidden" from the outer viscous and inviscid flows. Discontinuities are introduced at the separation and reattachment points with the present approximate technique; however, the resulting changes in effective body slope are less than those at the boattail-simulator juncture.

11

Sensitivity to Computational Grid Size

The accuracy of the flow solution over the boattail was found to depend on the grid step sizes, $\Delta \xi$ and $\Delta \eta$, particularly in the vicinity of shocks. Decreasing $\Delta \xi$ below about 0.05 of the body diameter caused divergence of the boundary-layer solution due to the large pressure gradients calculated by the inviscid flow solution. Furthermore, grid aspect ratios less than 0.5 or greater than 10 in the region of shocks tended to increase the streamline displacement resulting from nonconservative differencing. For the calculations presented in this paper, this aspect ratio was kept near unity over the entire boattail flow field. Parametric calculations in which $\Delta \xi$ and $\Delta \eta$ were varied separately showed that a value of unity tended both to minimize the residual error in the inviscid solution and to eliminate divergence of the boundary-layer solution.

CONCLUSIONS

The relaxation procedure of South and Jameson for the full potential flow equation has been coupled to a modified Reshotko-Tucker integral boundary-layer technique with an empirical model for separated flow. The method has been applied to the subsonic and transonic flow over a series of axisymmetric circular-arc boattails with solid jet plume simulators. Comparisons of theoretical and experimental surface pressures and boattail drag show the following:

1. The transonic viscous-inviscid method gives reasonable agreement with experimental boattail surface pressures except in regions of strong shock and boundary-layer interactions. The results suggest that conservative differencing may be necessary in obtaining the numerical inviscid solution to account properly for these interactions.

2. The concept of a discriminating streamline is shown to offer a reasonable representation of a separated region provided that the points of separation and reattachment are known. In the present calculations, these values were determined from experimental data since the discriminating streamline separation data of Presz were found to be inadequate for transonic flow.

3. The present results show a large sensitivity in the computed pressure distribution to the location and angle of the prescribed discriminating streamline. This sensitivity clearly indicates the need to develop a method in which the separation and reattachment points are found as part of the solution and are allowed to charge as the viscous-inviscid iteration proceeds.

4. The variations of predicted boattail drag with free-stream Mach number and boattail angle were qualitatively correct well into the region of transonic drag rise. Predicted cumulative drag distributions agreed well with experiment over most of the boattail length. However, absolute total drag levels were substantially underpredicted due to

12

the higher pressures calculated near the end of the boattail. The errors are attributed primarily to inaccuracies in accounting for shock effects, modeling of the boattail-simulator juncture, and modeling the separated region.

Langley Research Center
National Aeronautics and Space Administration
Hampton, VA 23665
November 4, 1977

REFERENCES

1. Reubush, David E.; and Putnam, Lawrence E.: An Experimental and Analytical Investigation of the Effect on Isolated Boattail Drag of Varying Reynolds Number up to 130×10^6. NASA TN D-8210, 1976.

2. South, Jerry C., Jr.; and Jameson, Antony: Relaxation Solutions for Inviscid Axisymmetric Transonic Flow Over Blunt or Pointed Bodies. AIAA Computational Fluid Dynamics Conference, July 1973, pp. 8-17.

3. Chow, Wen L.; Bober, Lawrence J.; and Anderson, Bernhard H.: Numerical Calculation of Transonic Boattail Flow. NASA TN D-7984, 1975.

4. Wilmoth, R. G.: Analytical Study of Viscous Effects on Transonic Flow Over Boattail Nozzles. AIAA Paper No. 77-223, Jan. 1977.

5. Yaros, S. F.: Prediction of Pressure Distributions on Axisymmetric Bodies in Transonic Flow. AIAA Paper No. 77-226, Jan. 1977.

6. Cosner, R. R.; and Bower, W. W.: A Patched Solution of the Transonic Flowfields About an Axisymmetric Boattail. AIAA Paper No. 77-227, Jan. 1977.

7. Yaeger, L. S.: Transonic Flow Over Afterbodies Including the Effects of Jet-Plume and Viscous Interactions With Separation. AIAA Paper No. 77-228, Jan. 1977.

8. Holst, T. L.: Numerical Solution of Axisymmetric Boattail Fields With Plume Simulators. AIAA Paper No. 77-224, Jan. 1977.

9. Reubush, David E.: Experimental Study of the Effectiveness of Cylindrical Plume Simulators for Predicting Jet-On Boattail Drag at Mach Numbers up to 1.30. NASA TN D-7795, 1974.

10. User's Manual for the External Drag and Internal Nozzle Performance Deck (Deck XI) – Supersonic Flow Analysis (Applicable to Deck VI). PWA-3465, Suppl. F, Pt. I (Contract No. AF33(615)-3128), Pratt & Whitney Aircraft, Sept. 1, 1968.

11. Bauer, Frances; Garabedian, Paul; Korn, David; and Jameson, Antony: Supercritical Wing Sections II, Volume 108 of Lecture Notes in Economics and Mathematical Systems, Springer-Verlag, 1975.

12. Bavitz, Paul C.: An Analysis for Two-Dimensional Transonic Viscous Flow. NASA TN D-7718, 1975.

13. Putnam, Lawrence E.; and Abeyounis, William K.: Experimental and Theoretical Study of Flow Fields Surrounding Boattail Nozzles at Subsonic Speeds. AIAA Paper No. 76-675, July 1976.

14. Keller, James D.; and South, Jerry C., Jr.: RAXBOD: A Fortran Program for Inviscid Transonic Flow Over Axisymmetric Bodies. NASA TM X-72831, 1976.

15. Reshotko, Eli; and Tucker, Maurice: Approximate Calculation of the Compressible Turbulent Boundary Layer With Heat Transfer and Arbitrary Pressure Gradient. NACA TN 4154, 1957.

16. Alber, Irwin E.; Bacon, John W.; Masson, Bruce S.; and Collins, Donald J.: An Experimental Investigation of Turbulent Transonic Viscous-Inviscid Interactions. AIAA J., vol. 11, no. 5, May 1973, pp. 620-627.

17. Presz, Walter Michael, Jr.: Turbulent Boundary Layer Separation of Axisymmetric Afterbodies. Ph. D. Thesis, Univ. of Connecticut, 1974.

18. Page, R. H.: A Theory for Incipient Separation Developments in Mechanics, Vol. 1, J. E. Lay and L. E. Malvern, eds., Plenum Press, 1961, pp. 563-577.

19. Abeyounis, William Kelly: Boundary Layer Separation on Isolated Boattail Nozzle. M.S. Thesis, The George Washington University, May 1977. (Available as NASA CR-152703.)

20. Newman, Perry A.; and South, Jerry C., Jr.: Conservative Versus Nonconservative Differencing: Transonic Streamline Shape Effects. NASA TM X-72827, 1976.

TABLE I.- BOATTAIL GEOMETRIC PARAMETERS
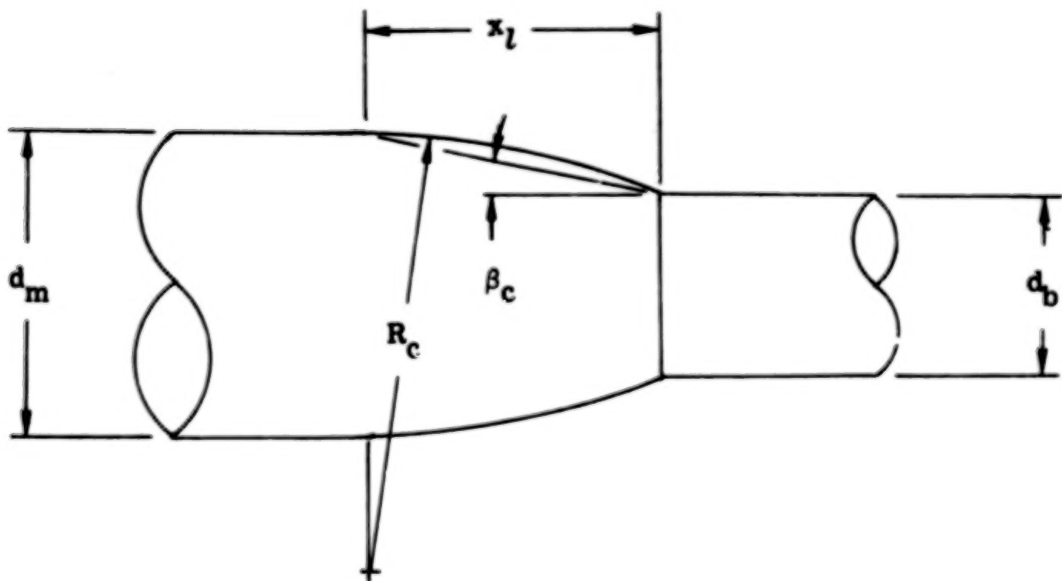
Configuration	x_l/d_m	d_b/d_m	R_c/d_m	β_c, deg
1	0.800	0.51	1.429	17.027
2	1.000	.51	2.163	13.766
3	1.768	.51	6.500	7.891
4	1.000	.61	2.662	11.034
6	1.000	.71	3.521	8.250
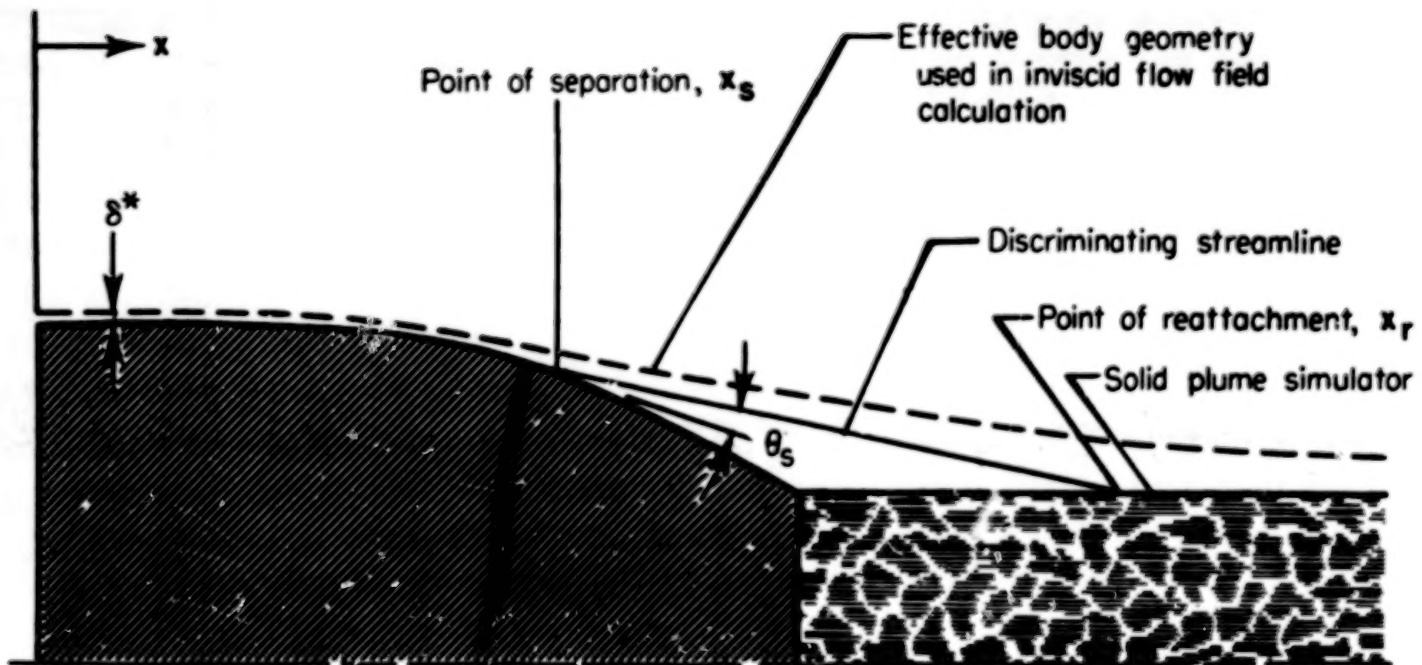
Figure 1.- Model of afterbody flow field.

17.
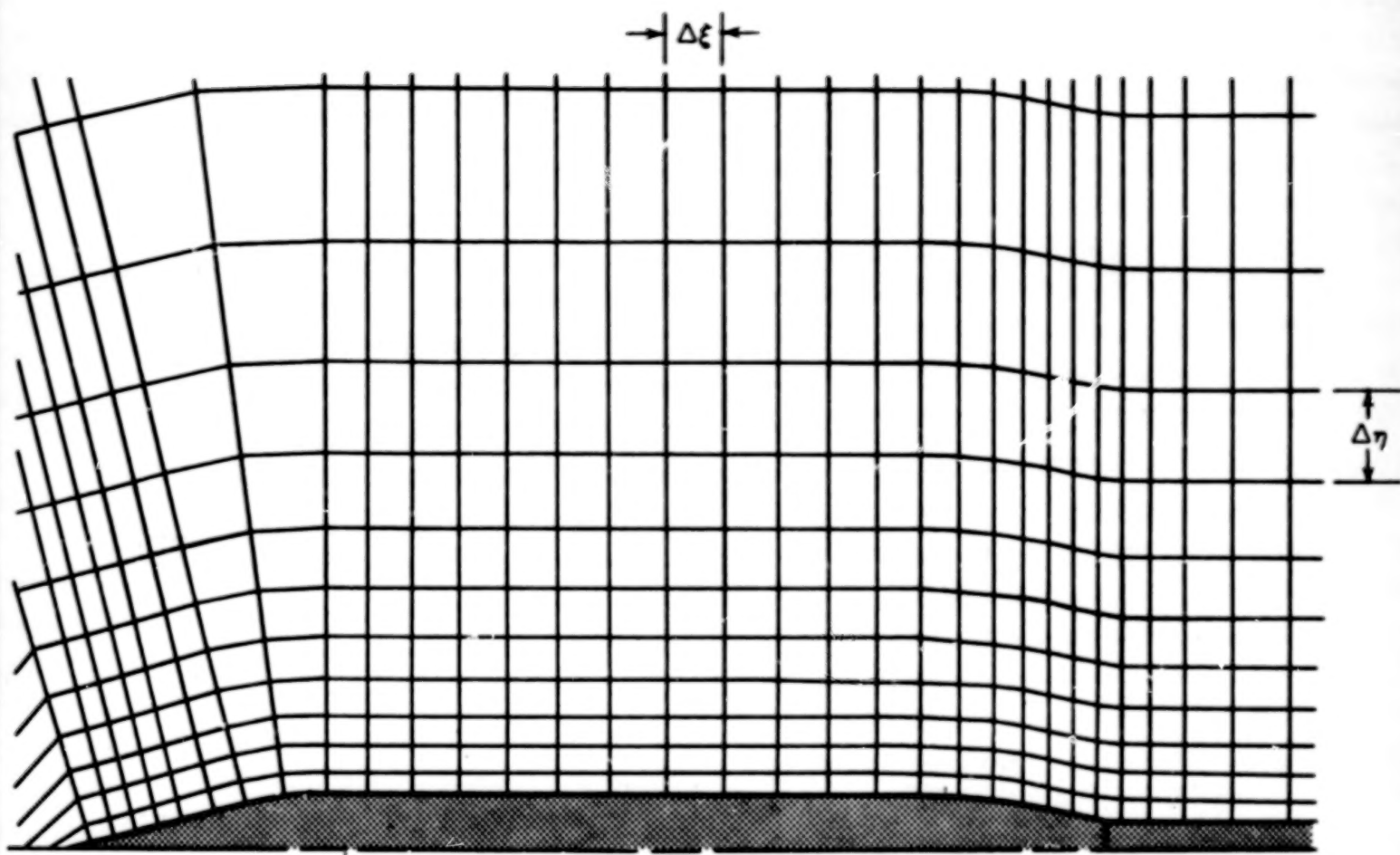
Figure 2.- Typical computational grid for cone-cylinder forebody $\left(L/d_m = 8\right)$ with circular-arc boattail.

18.
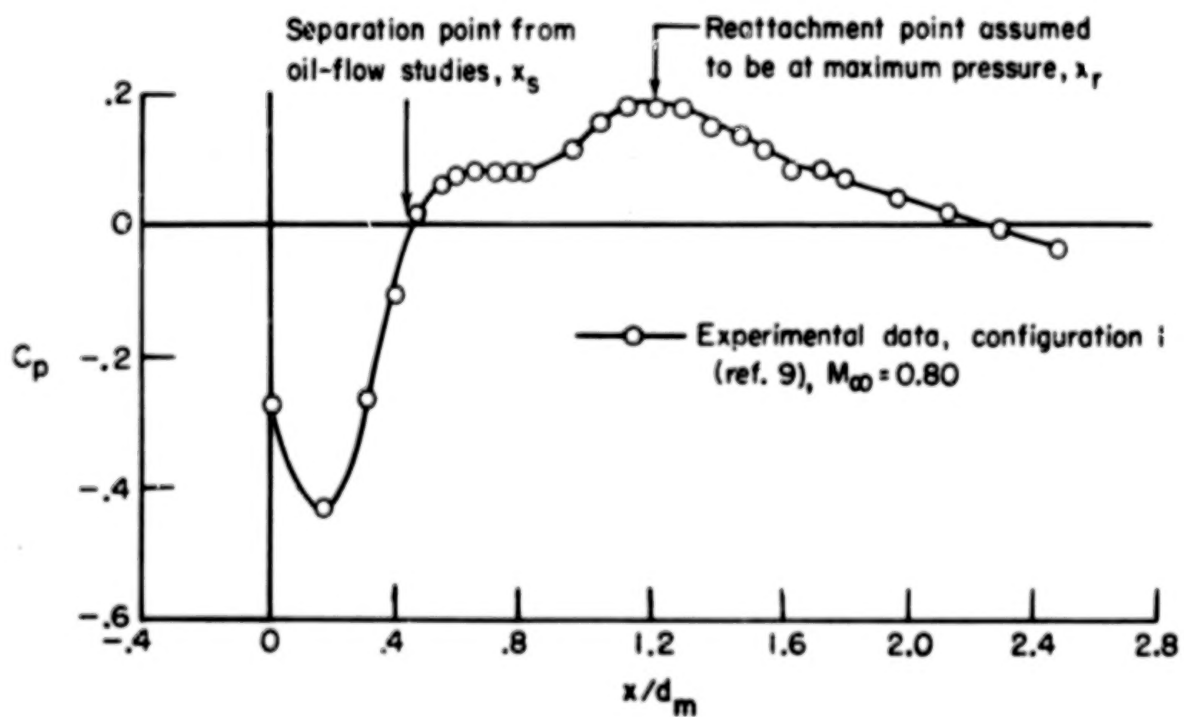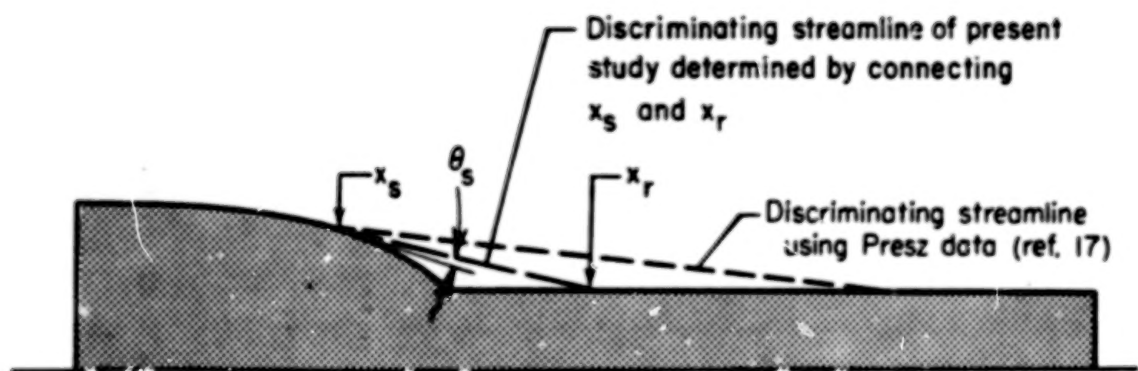
Figure 3.- Determination of discriminating streamline separation angle.

19.
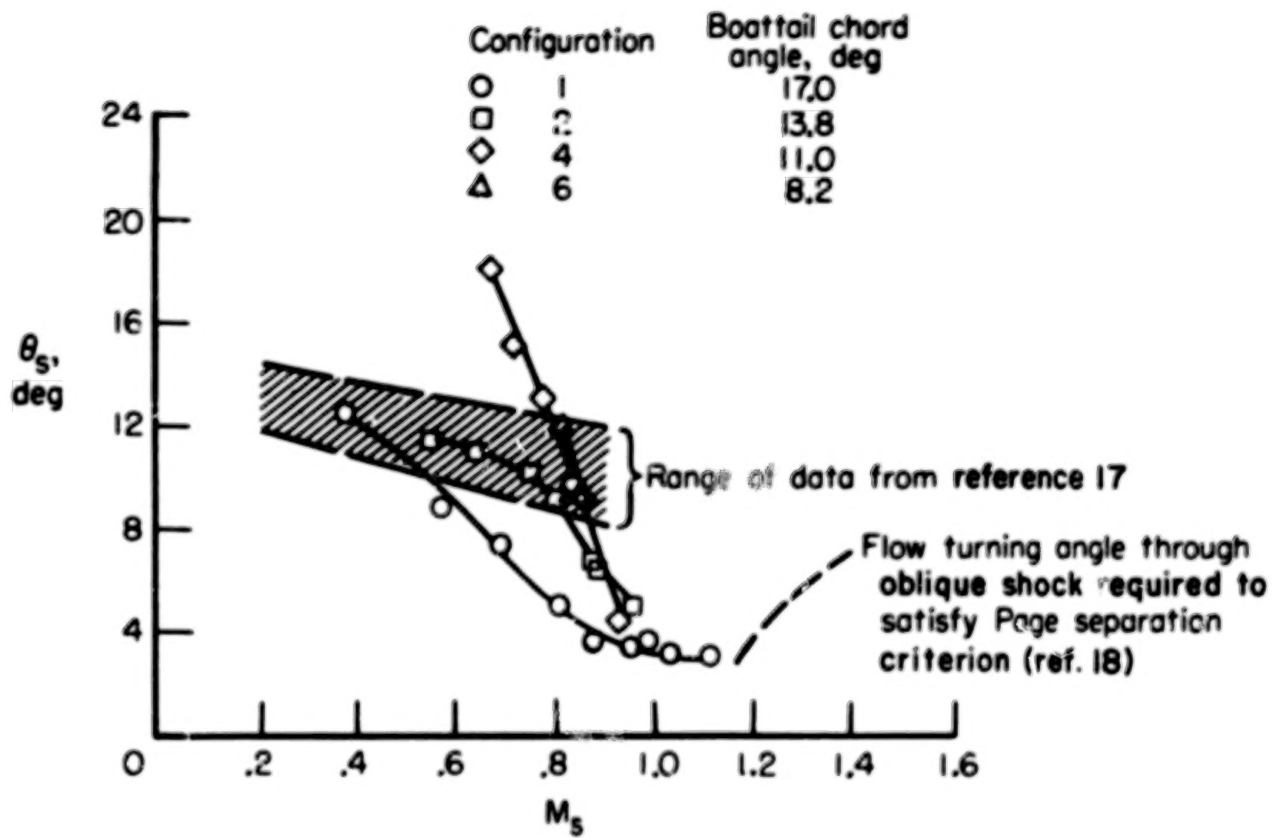
Figure 4.- Variation of discriminating streamline separation angle with local Mach number at separation.

20.
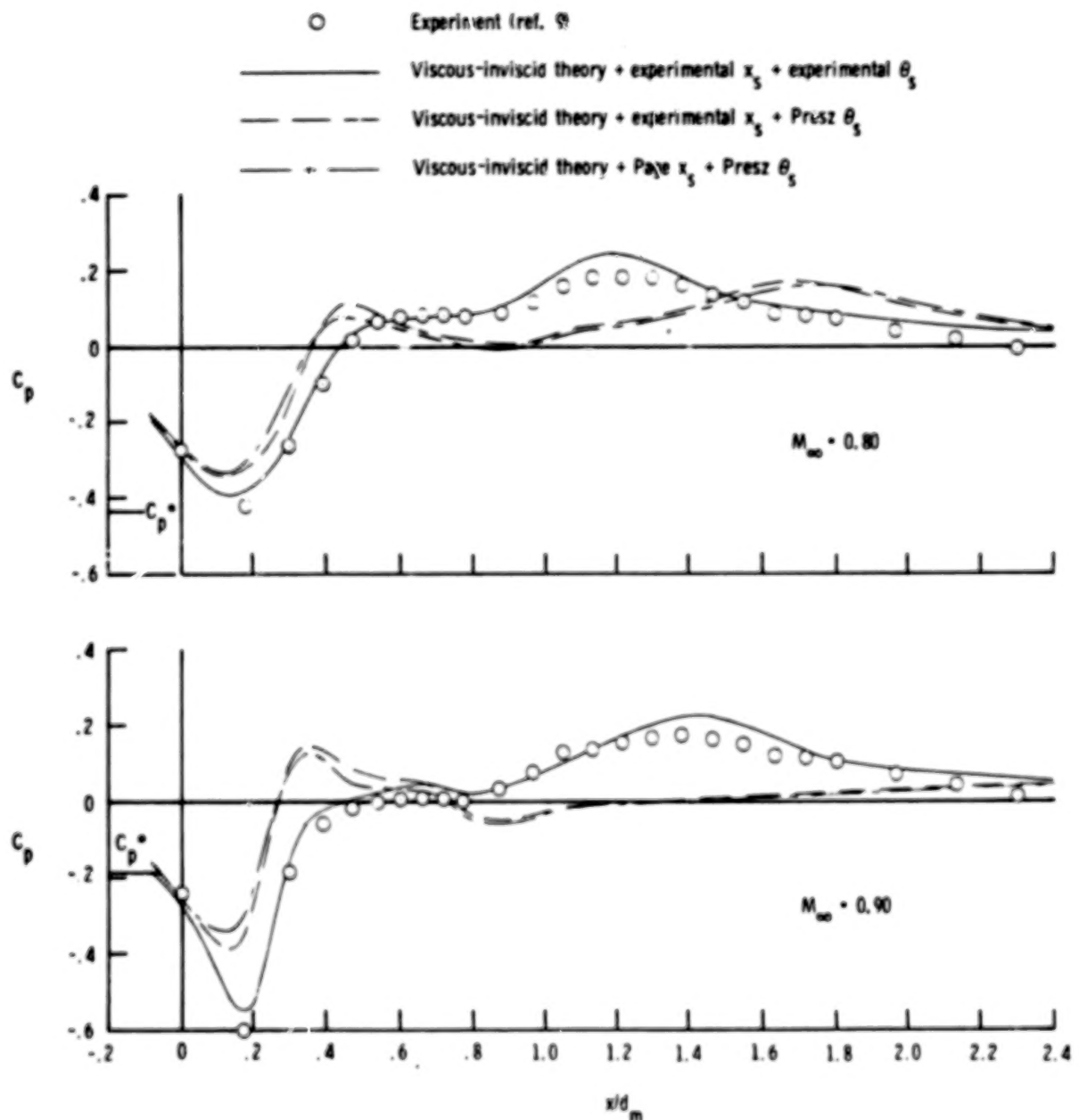
Figure 5.- Comparison of experimental pressure distributions with theoretical predictions based on various models of separated region. Configuration 1.

21.
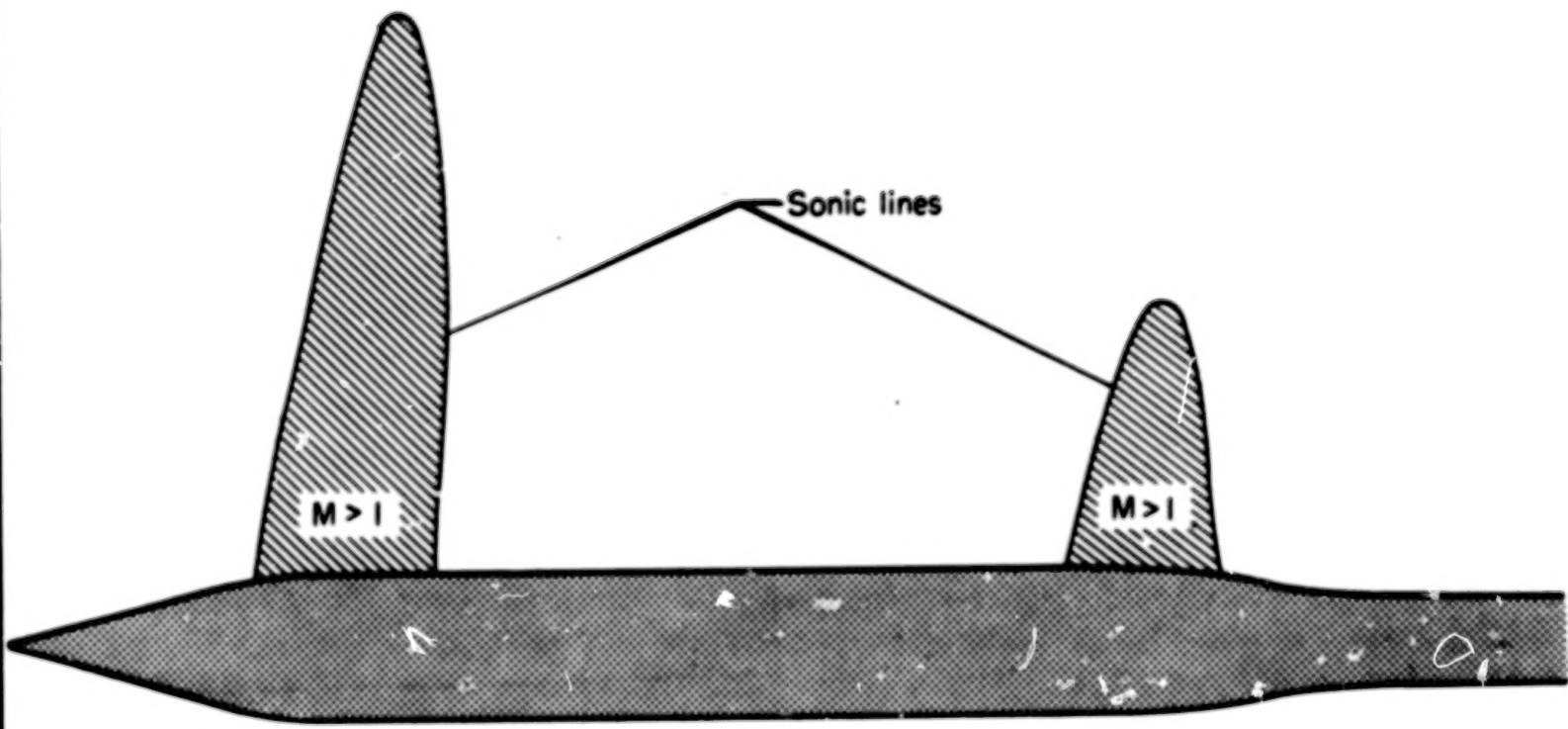
Figure 6.- Regions of local supersonic flow. $M_{\infty} = 0.96$.

22.
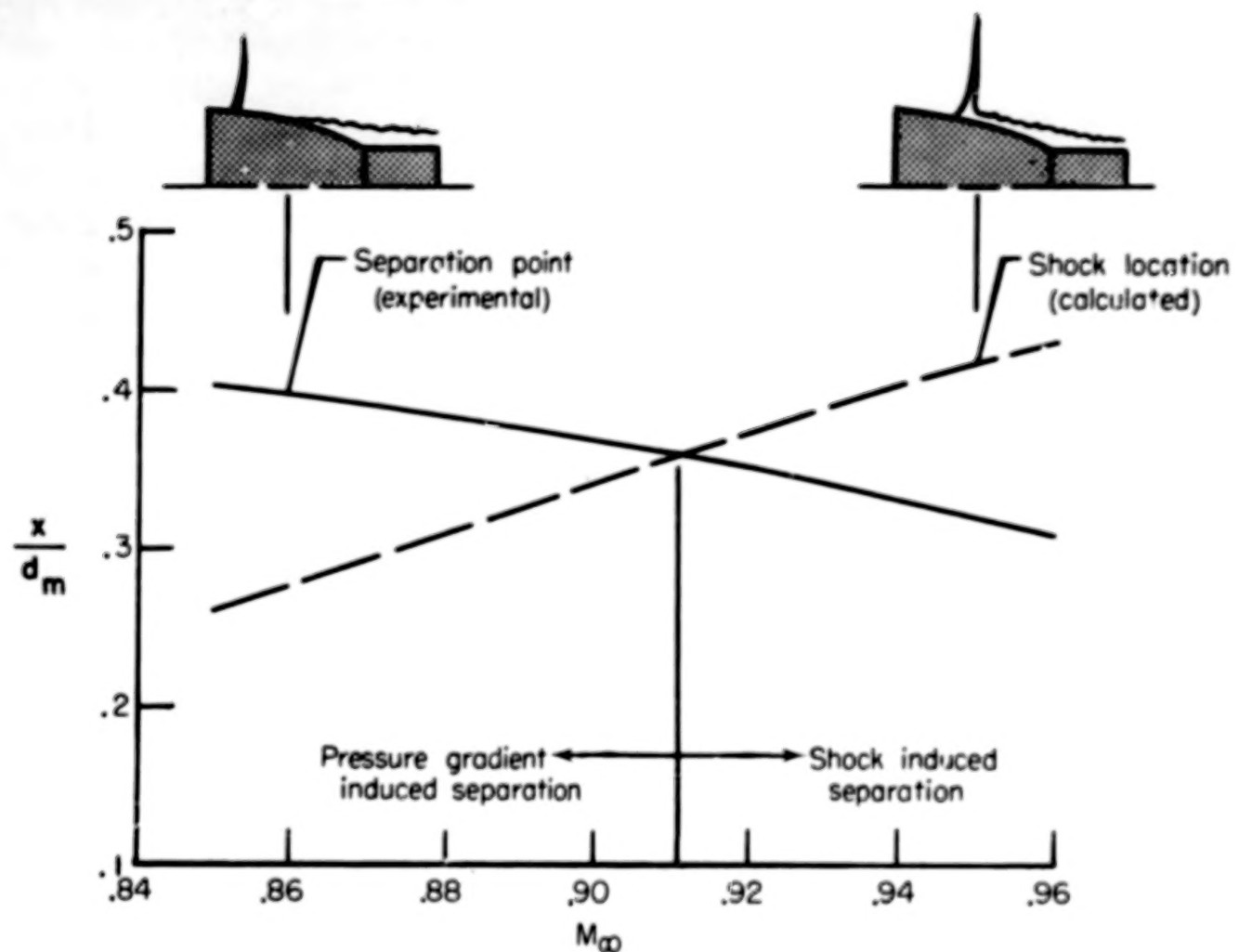
Figure 7.- Effect of free-stream Mach number on separation and shock locations. Configuration 1.

23.
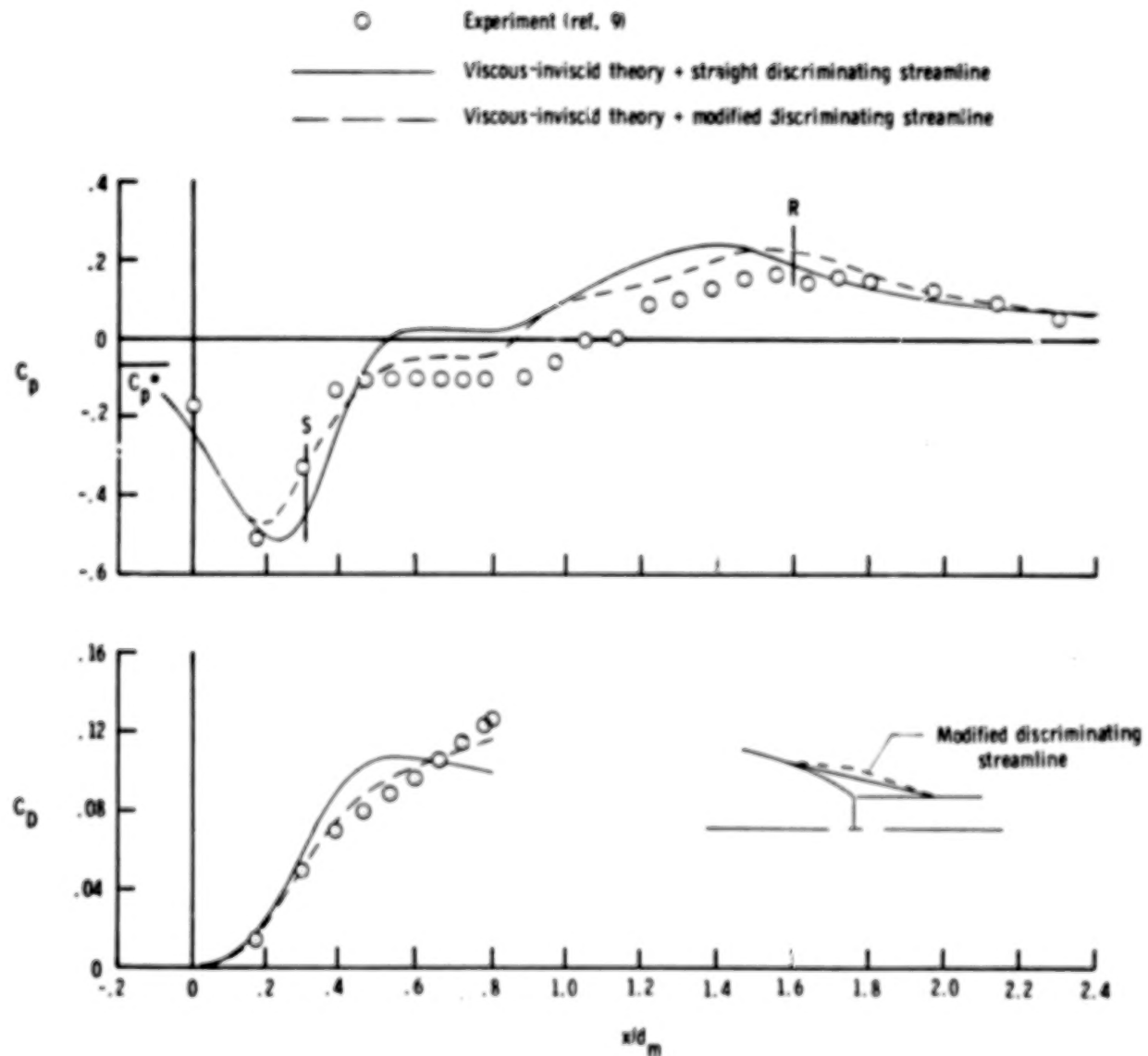
Figure 8.- Effect of discriminating streamline shape for separated flow.
Configuration 1; $M_\infty = 0.96$.

24.
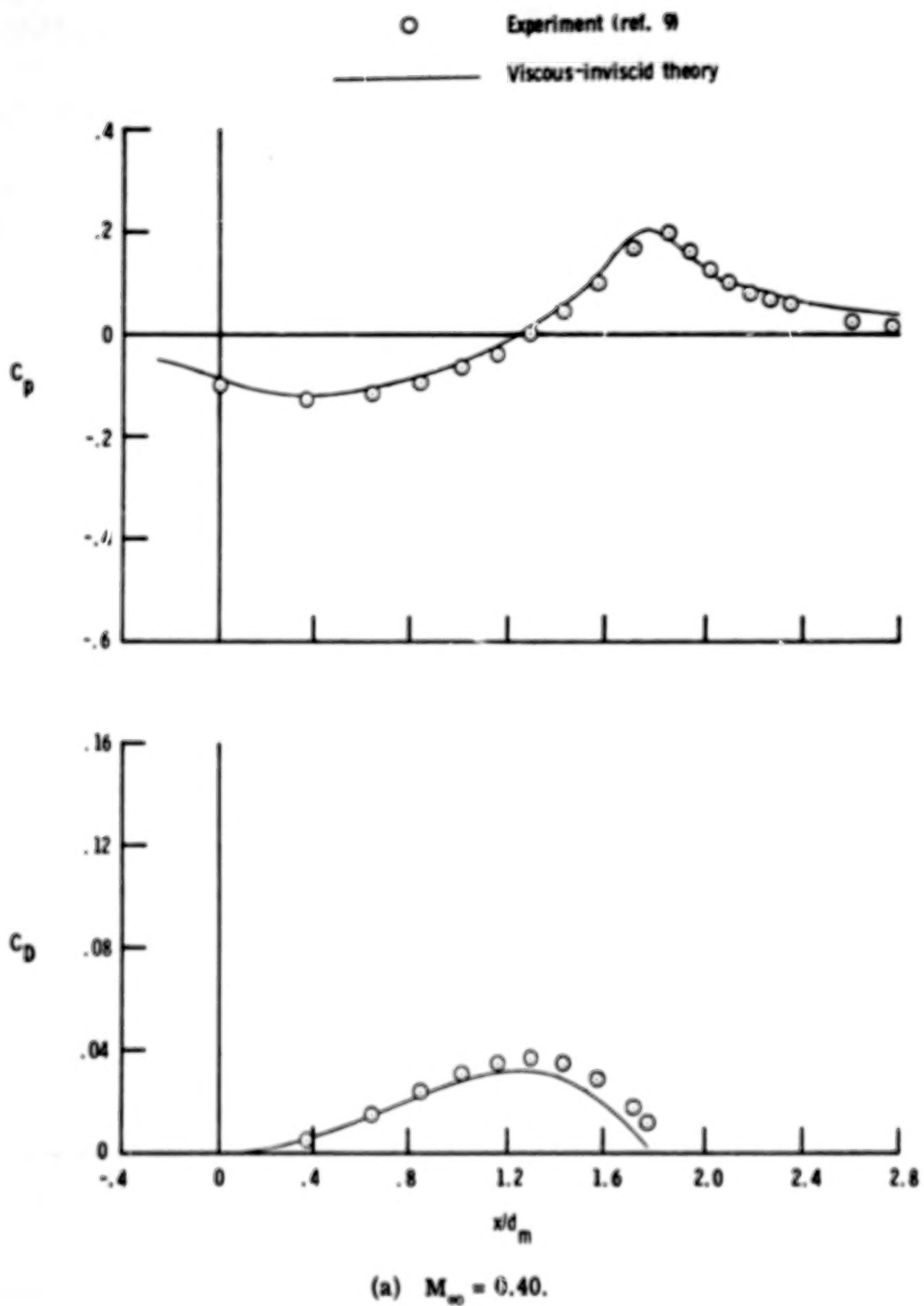
(a) $M_\infty = 0.40$.

Figure 9.- Comparison of theoretical and experimental pressure and cumulative drag distributions. Configuration 3; $x_\ell/d_m = 1.77$; $\beta_c = 7.9^\circ$.

C $\quad$ Experiment (ref. 9)

————————— Viscous-inviscid theory

(b) $M_\infty = 0.60$.

Figure 9.- Continued.

○   Experiment (ref. 9)

—————— Viscous-inviscid theory

(c) $M_\infty = 0.70$.

Figure 9.- Continued.

27

○   Experiment (ref. 9)

———— Viscous-inviscid theory
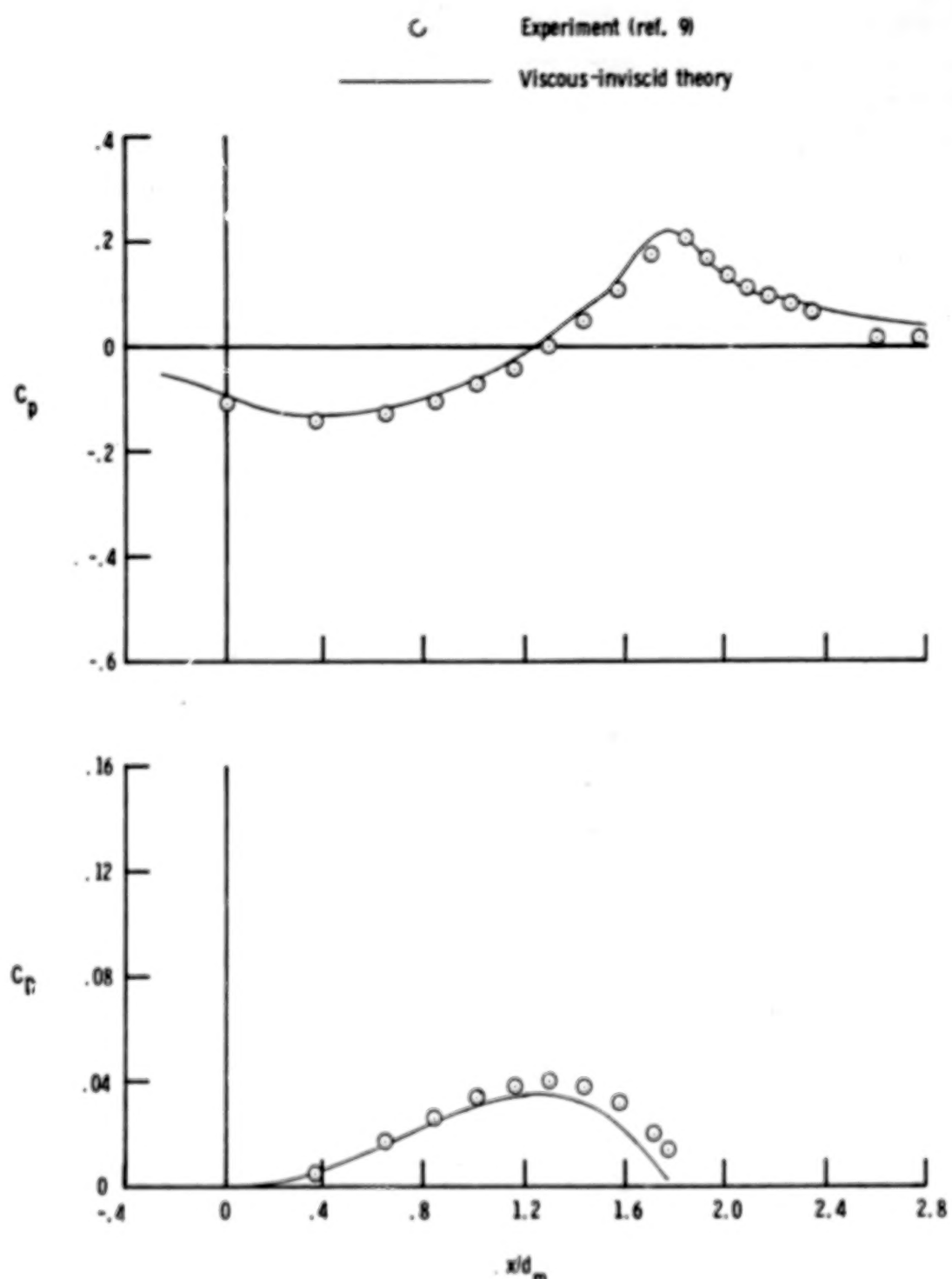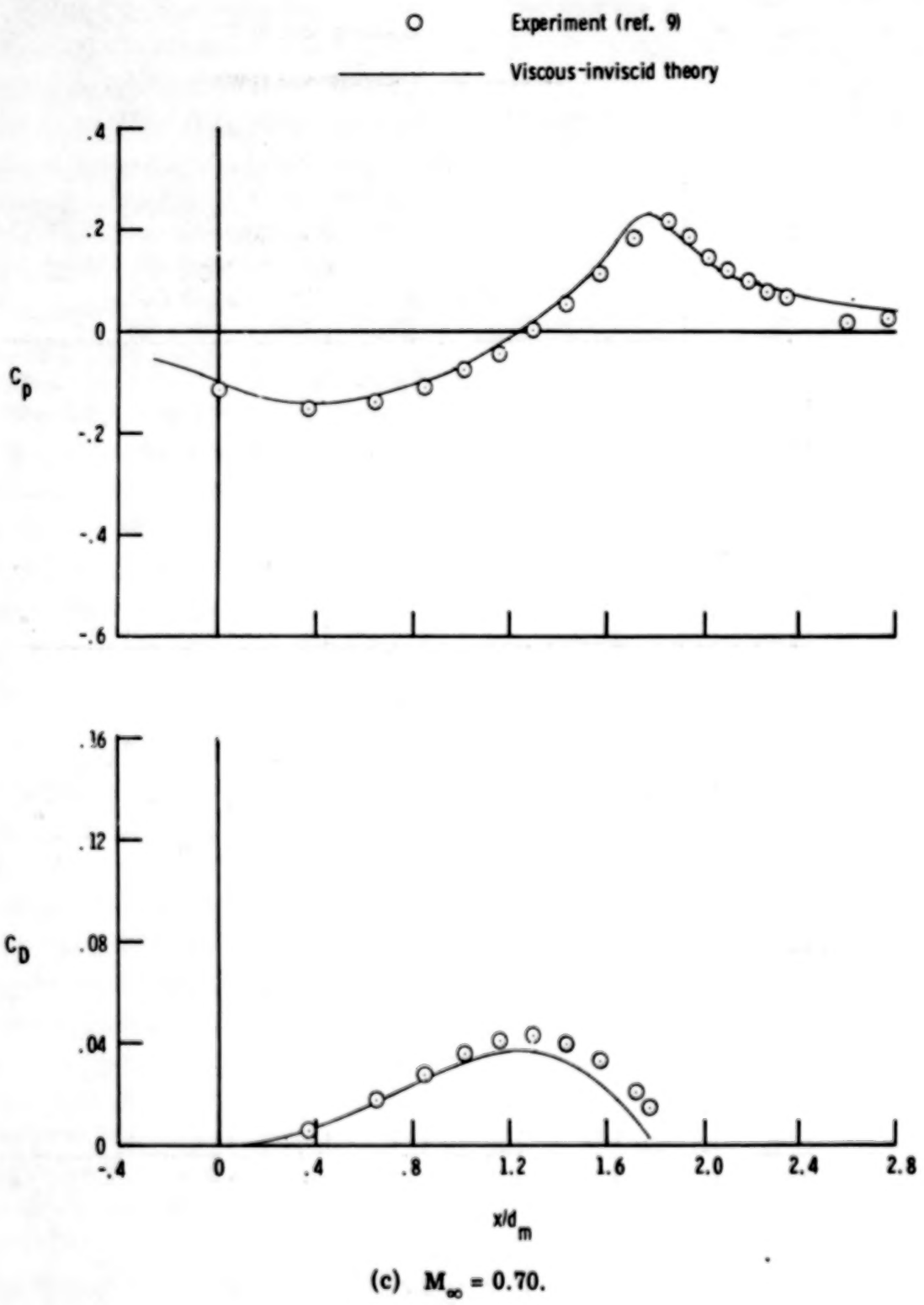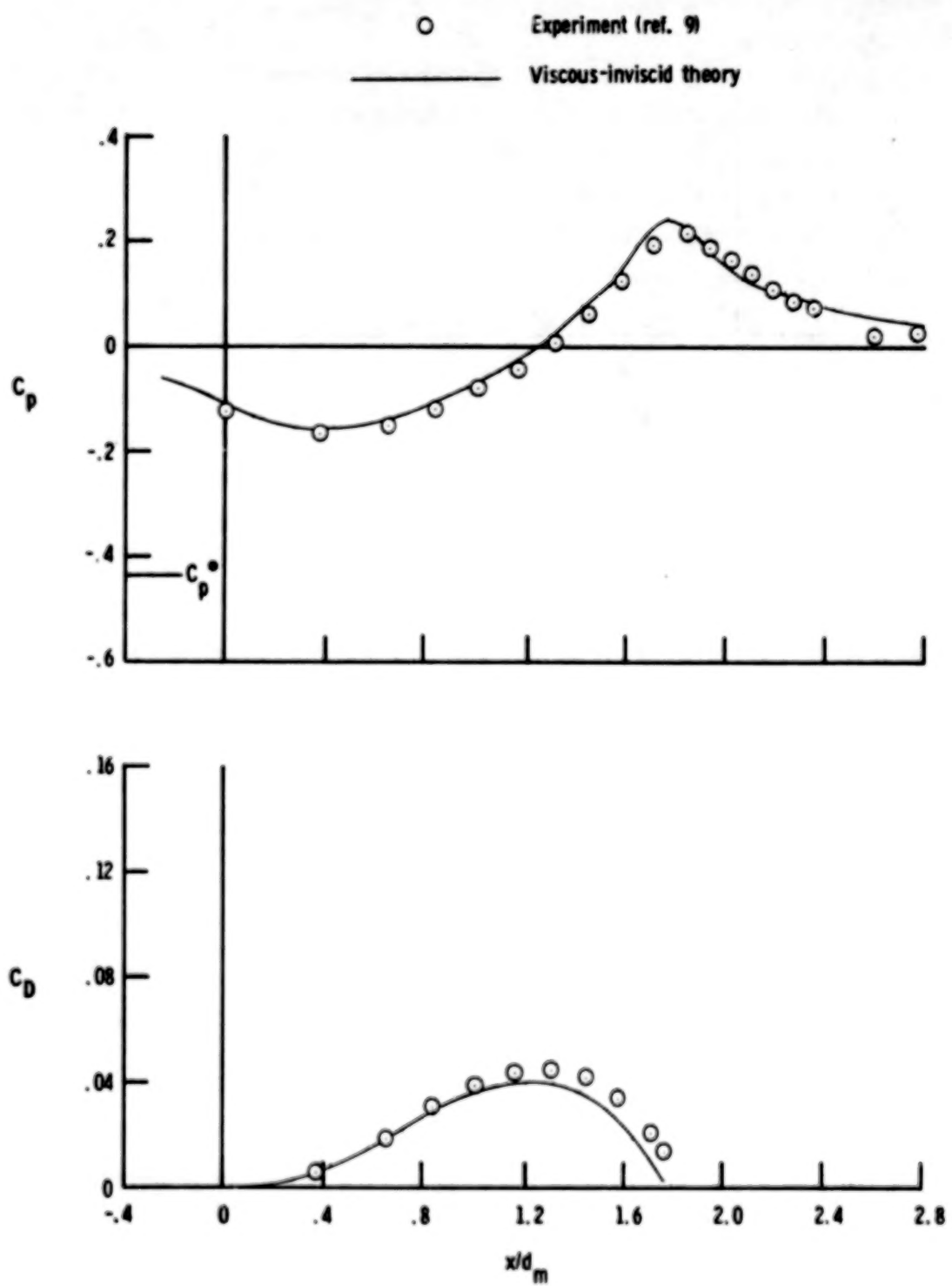
(d) $M_\infty = 0.80$.
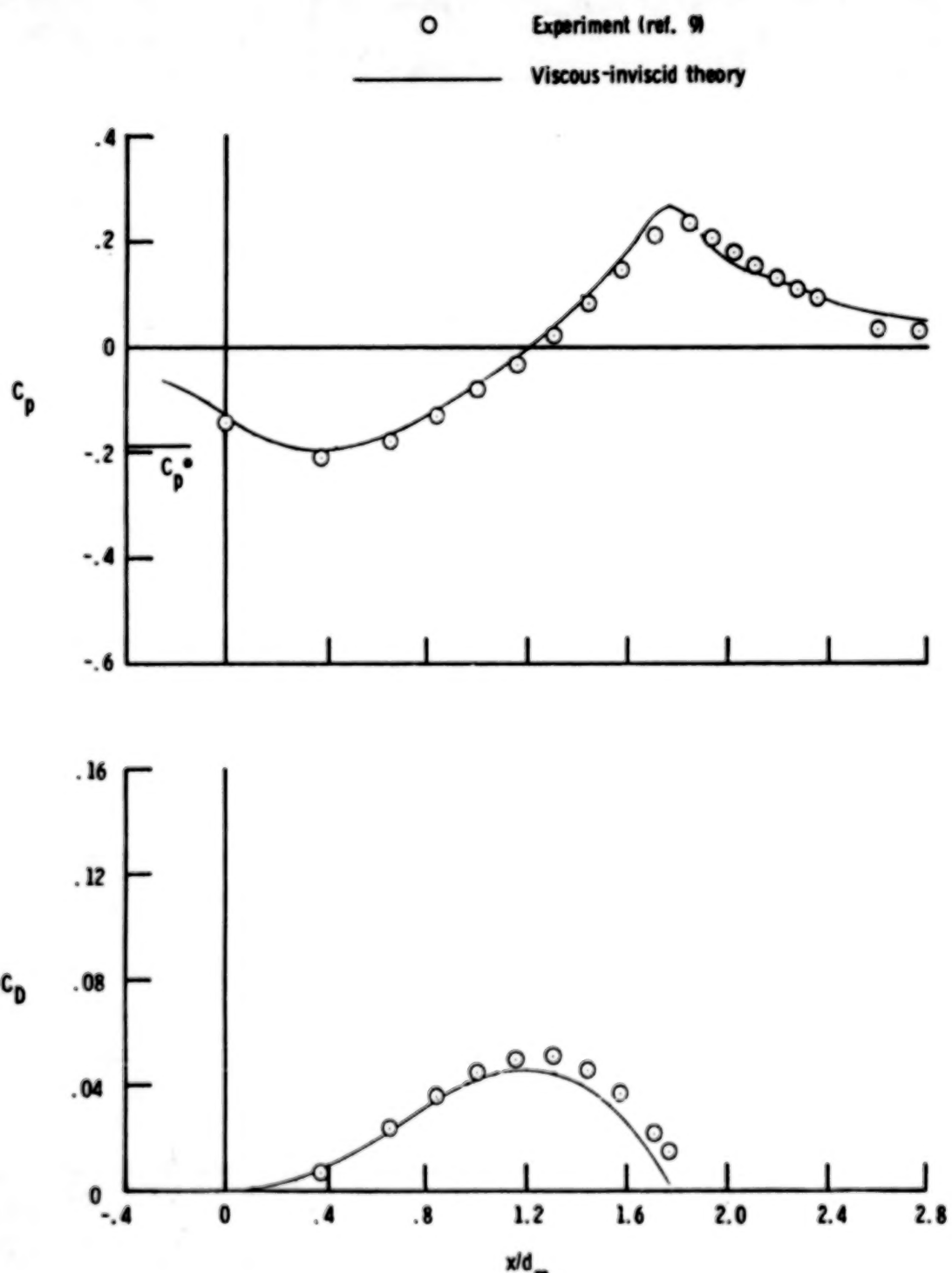
Figure 9.- Continued.

(e) $M_\infty = 0.90$.

Figure 9.- Continued.

(f) $M_\infty = 0.92$.

Figure 9.- Continued.

30

○   Experiment (ref. 9)

——————— Viscous-inviscid theory
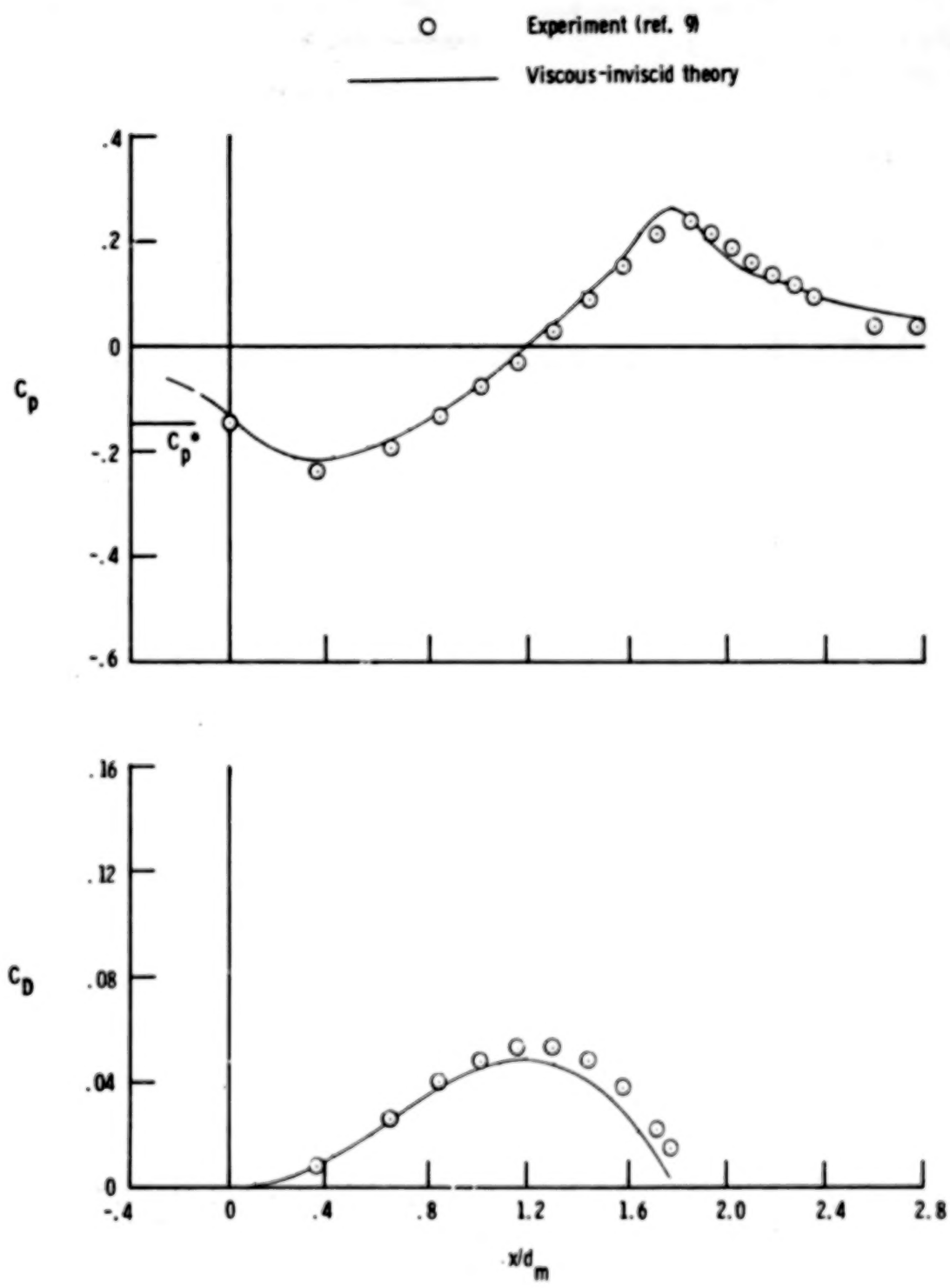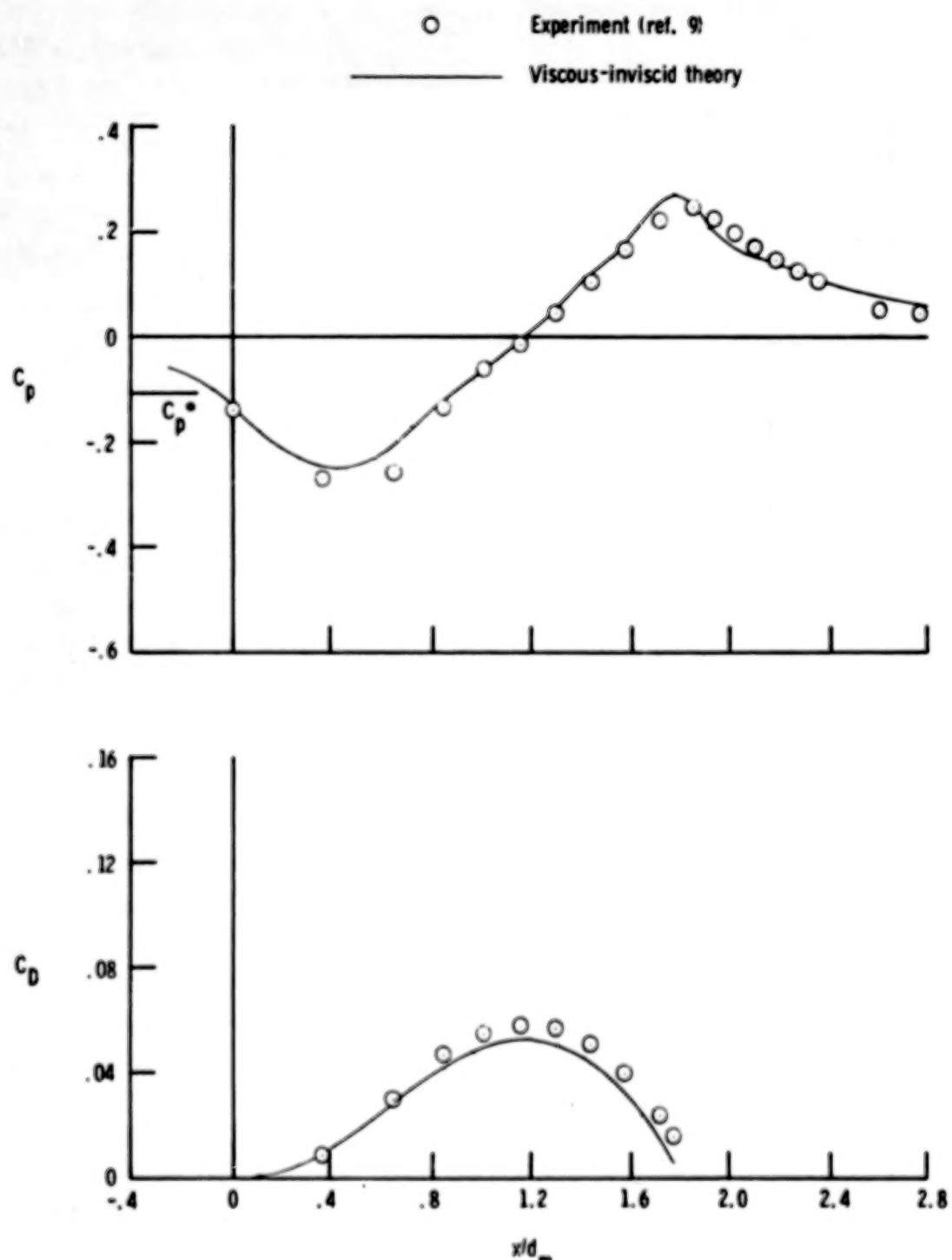
(g) $M_\infty = 0.94$.
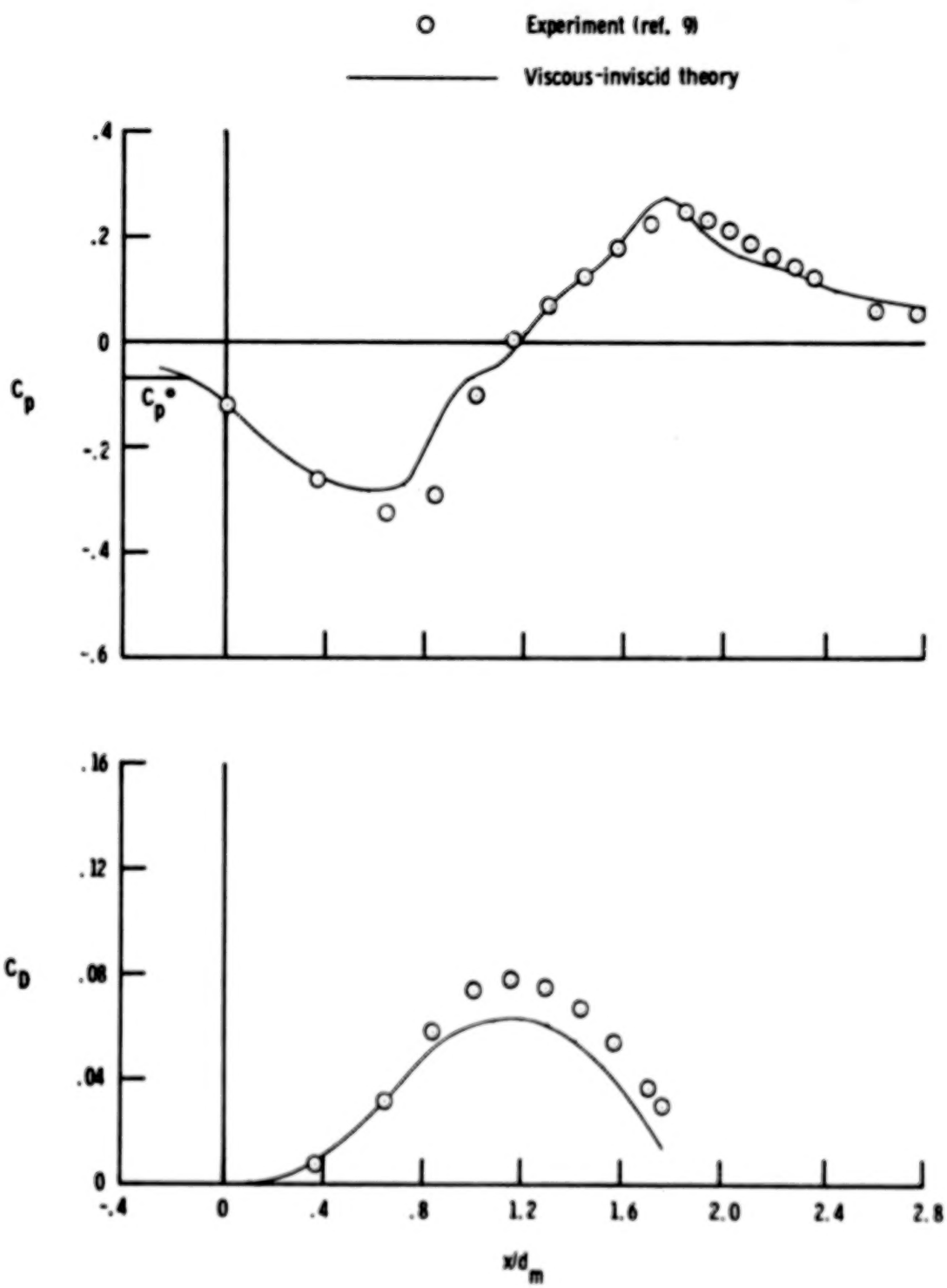
Figure 9.- Continued.

(h) $M_\infty = 0.96$.

Figure 9.- Concluded.
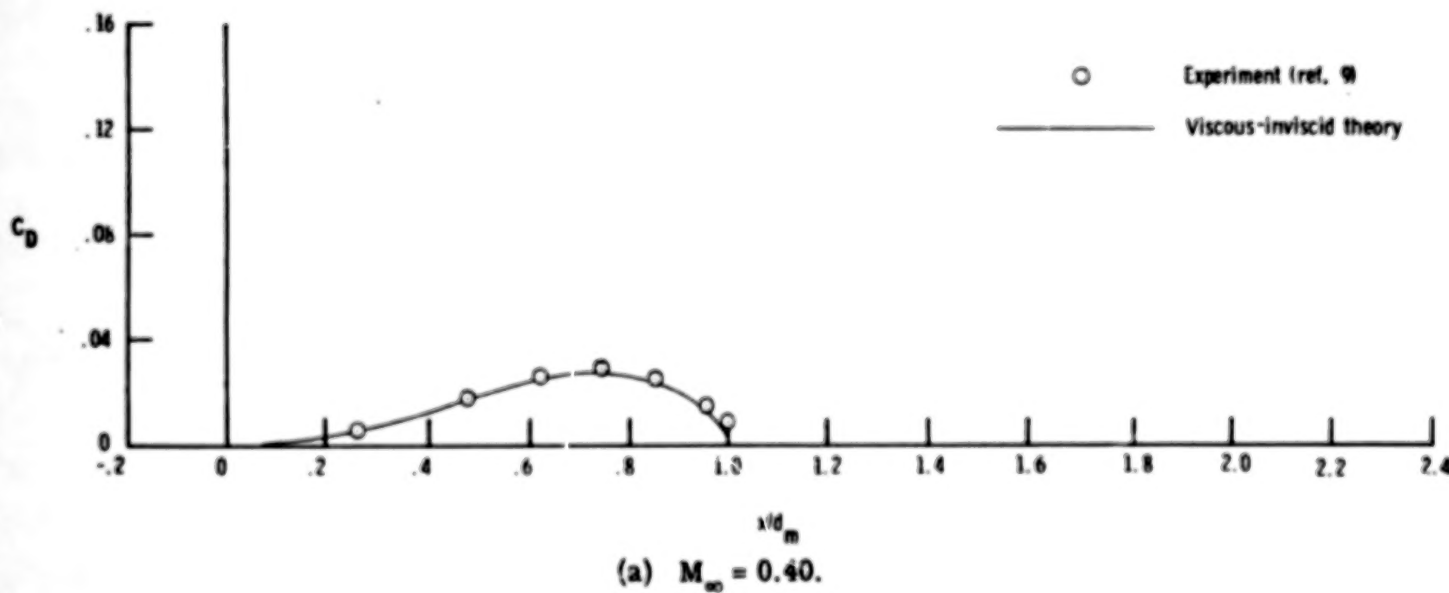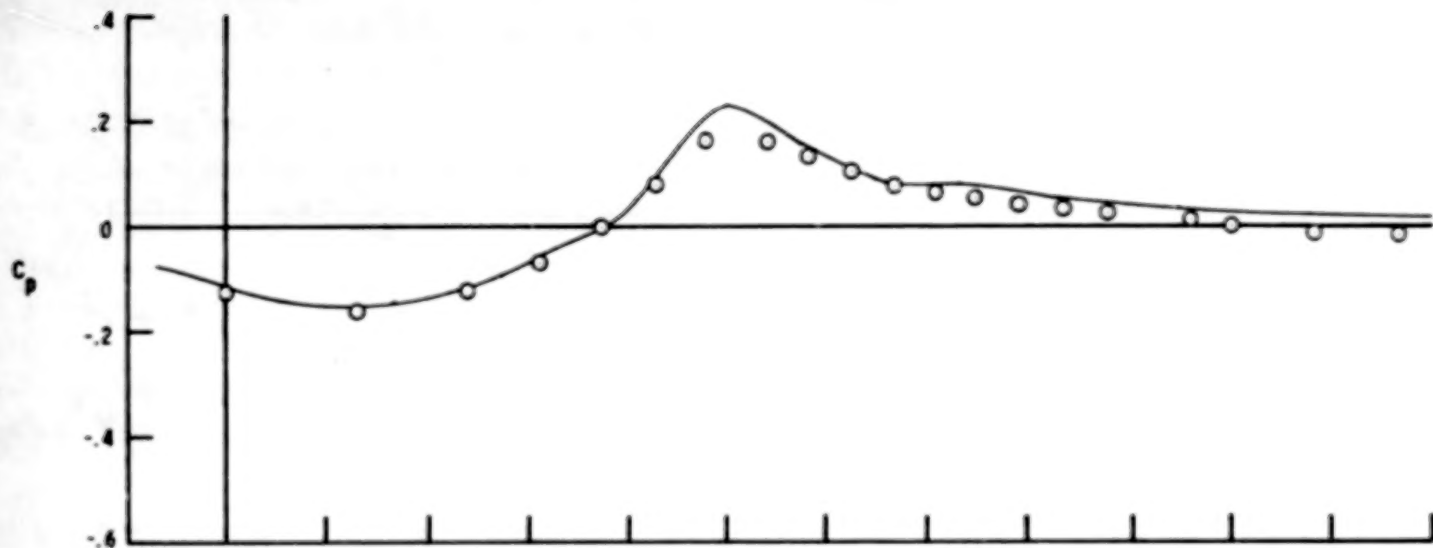
(a) $M_\infty = 0.40$.

Figure 10.- Comparison of theoretical and experimental pressure and cumulative drag distributions.
Configuration 6; $x_\ell/d_m = 1.0$; $\beta_c = 8.2^o$.

33.
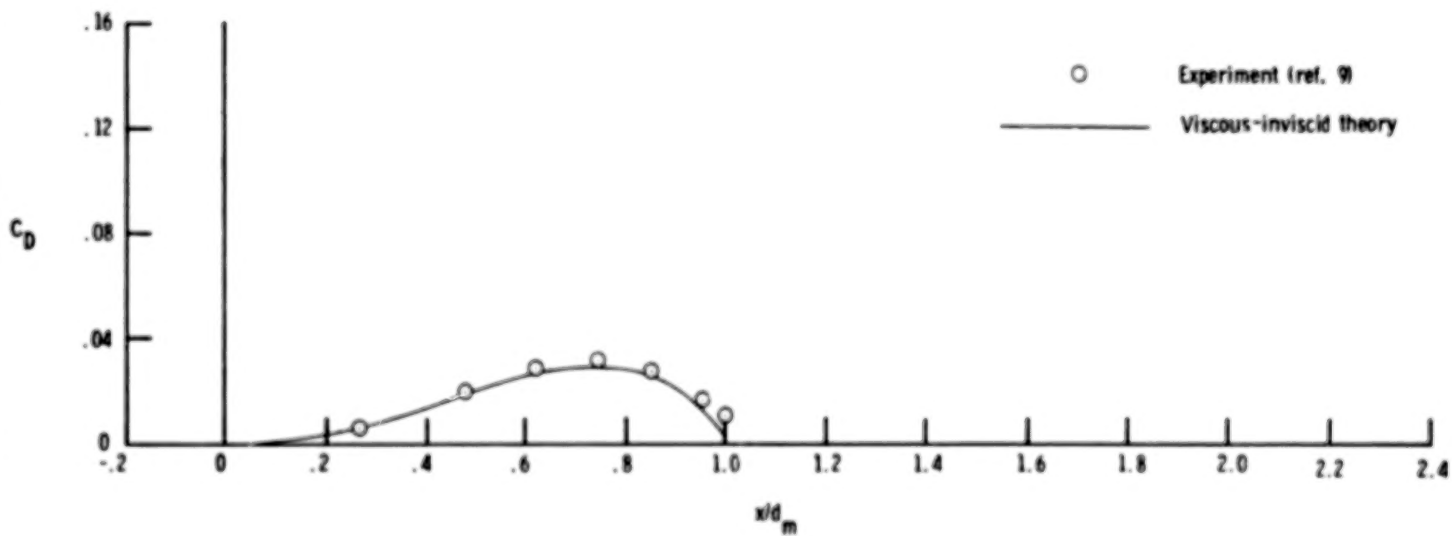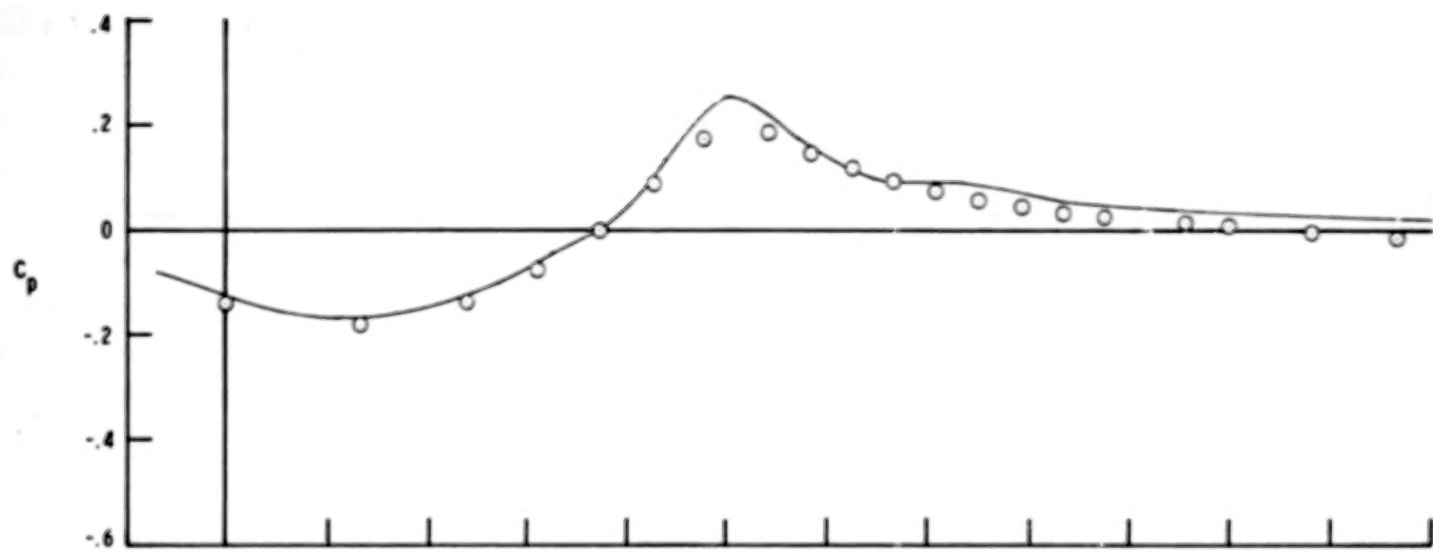
(b) $M_\infty = 0.60$.

Figure 10.- Continued.

34.
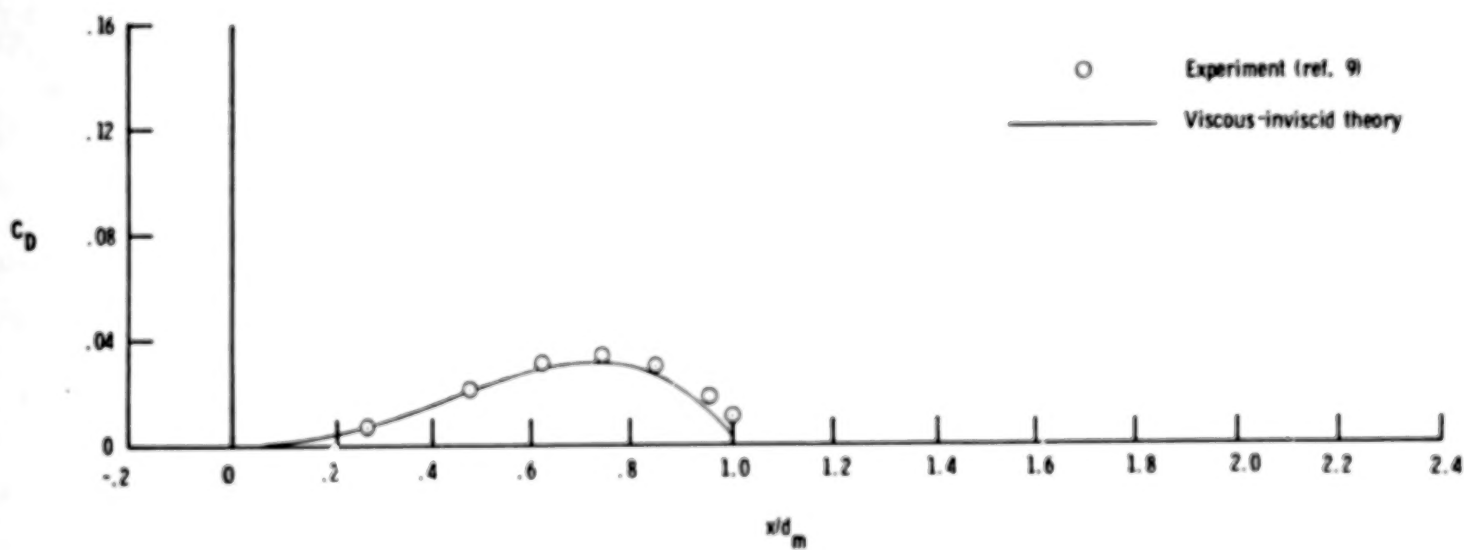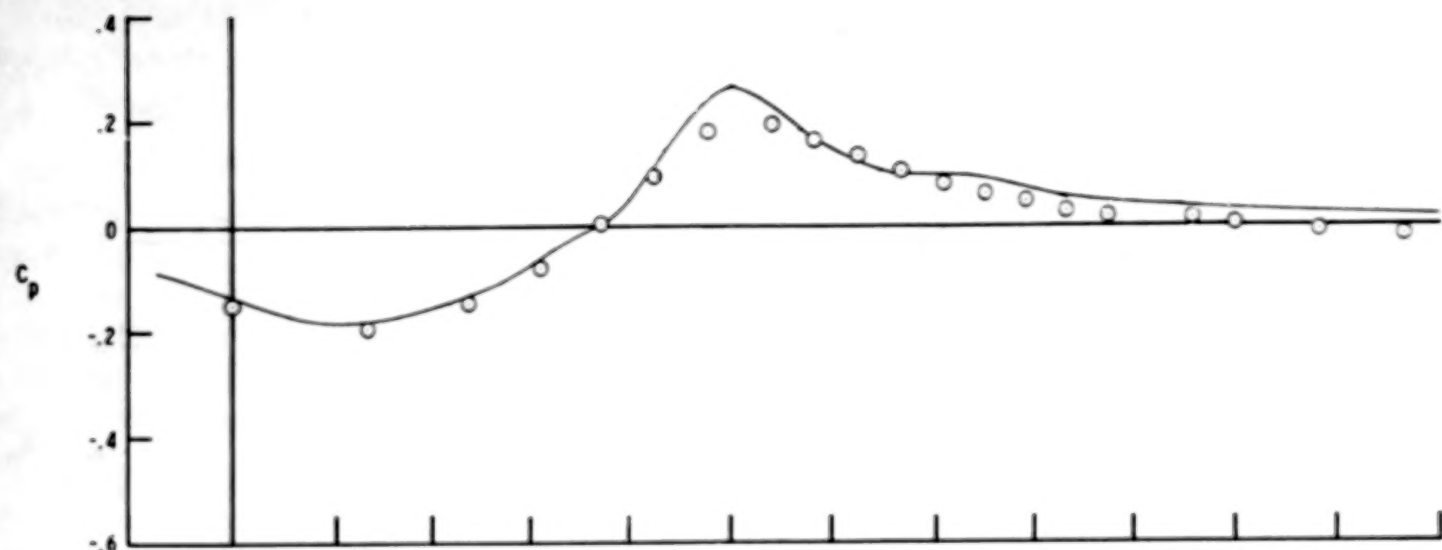
(c) $M_\infty = 0.70$.

Figure 10.- Continued.

35.
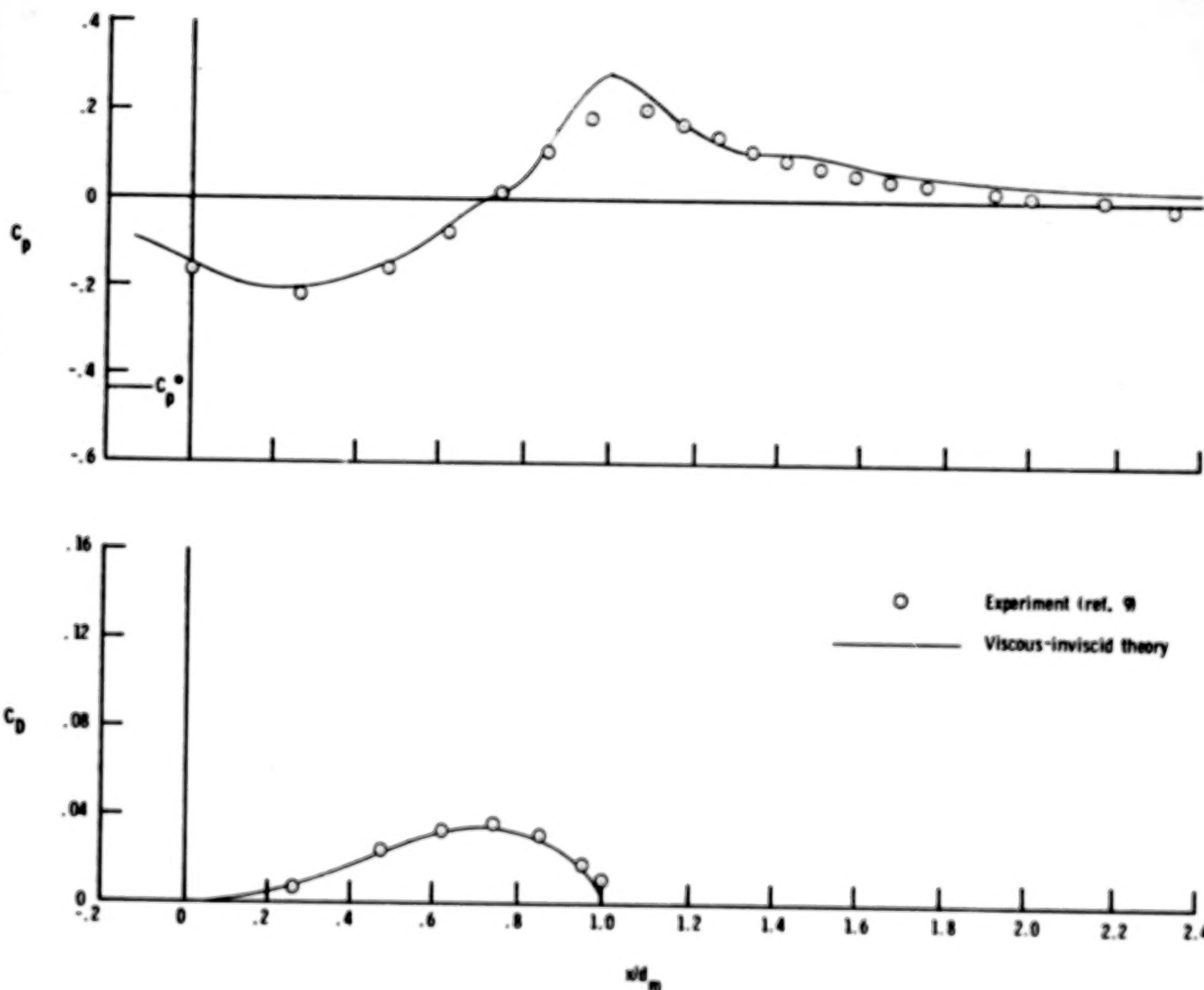
(d) $M_\infty = 0.80$.

Figure 10.- Continued.

36
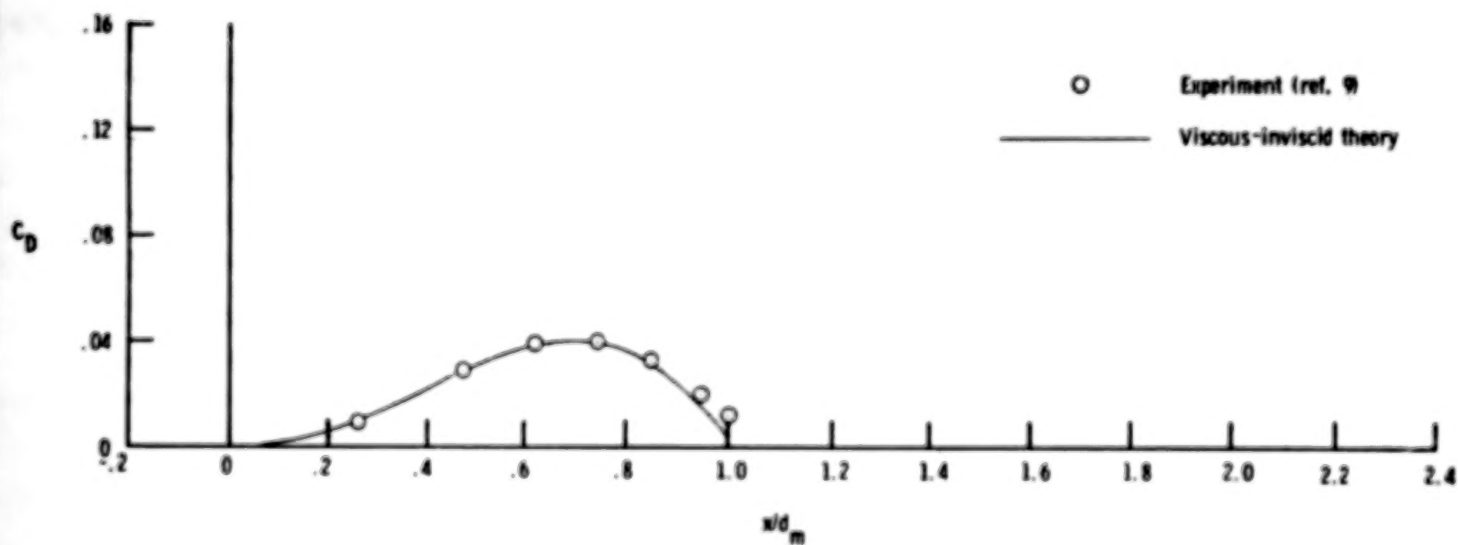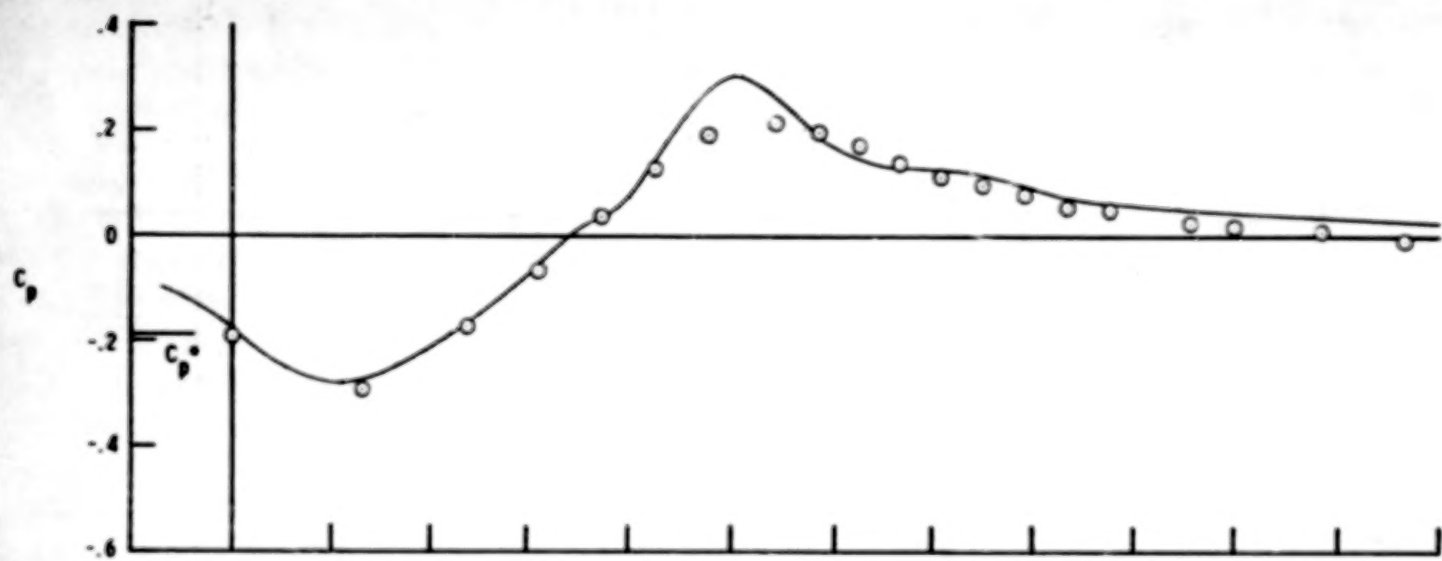
(e) $M_\infty = 0.90$.

Figure 10.- Continued.

37.
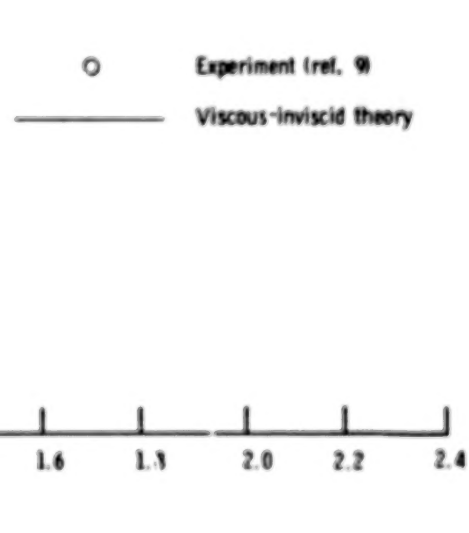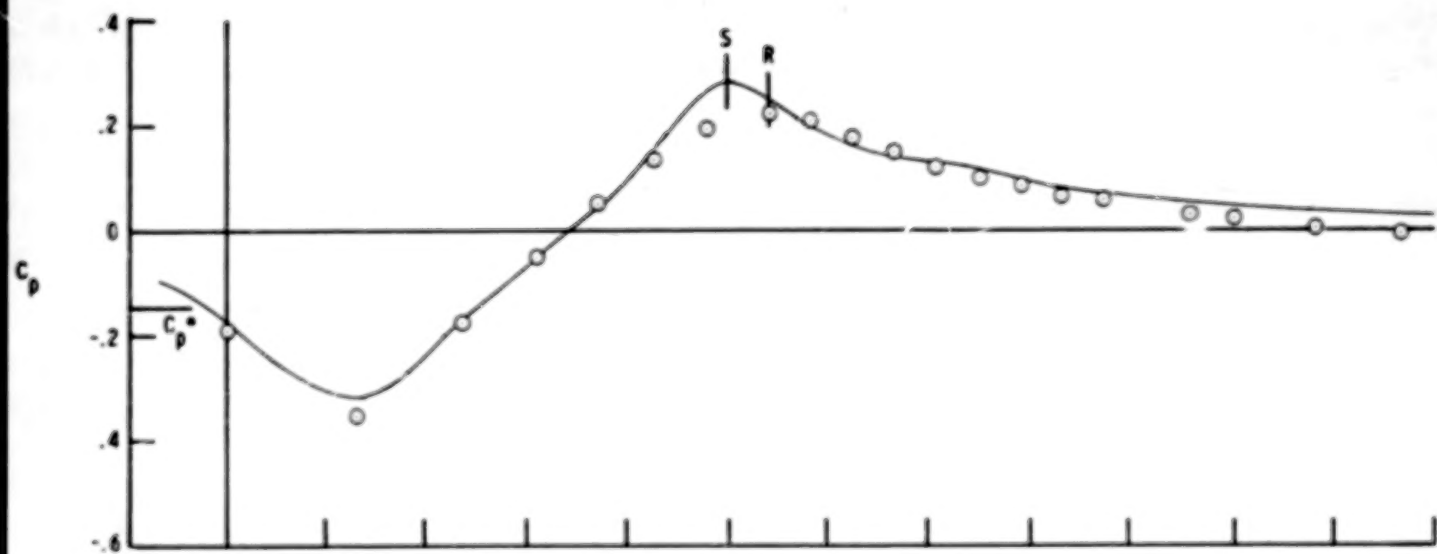
(f) $M_\infty = 0.92$.

Figure 10.- Concluded.

38
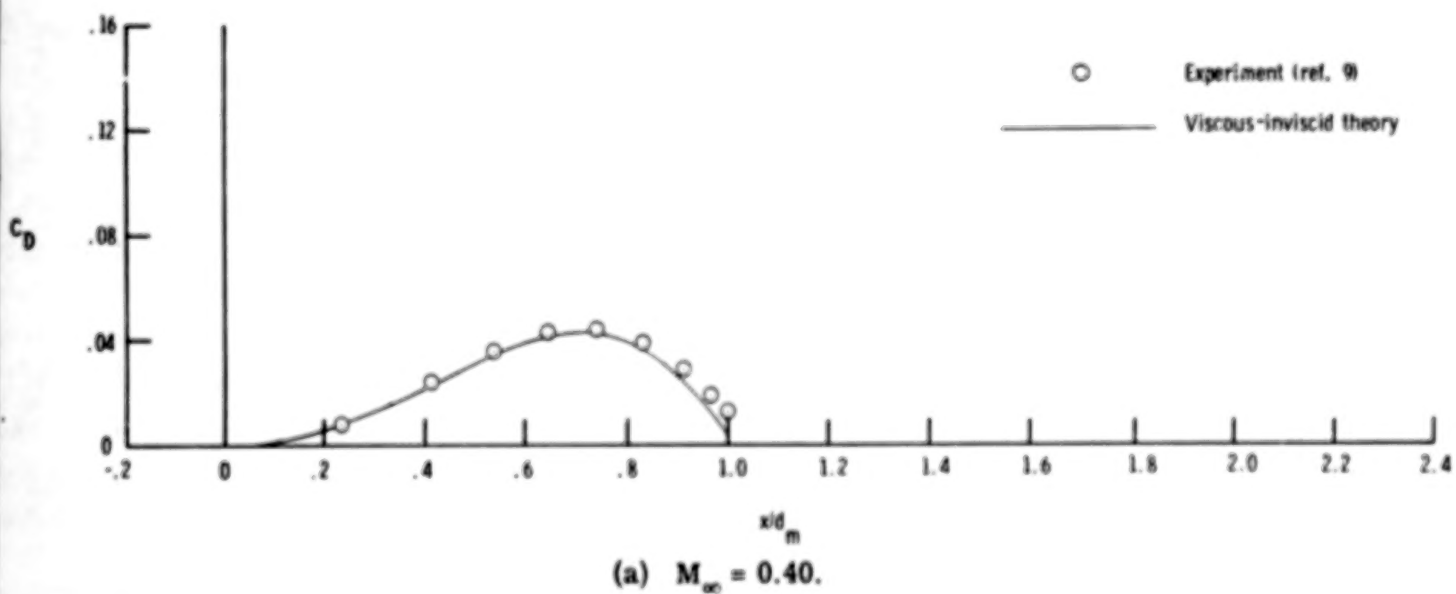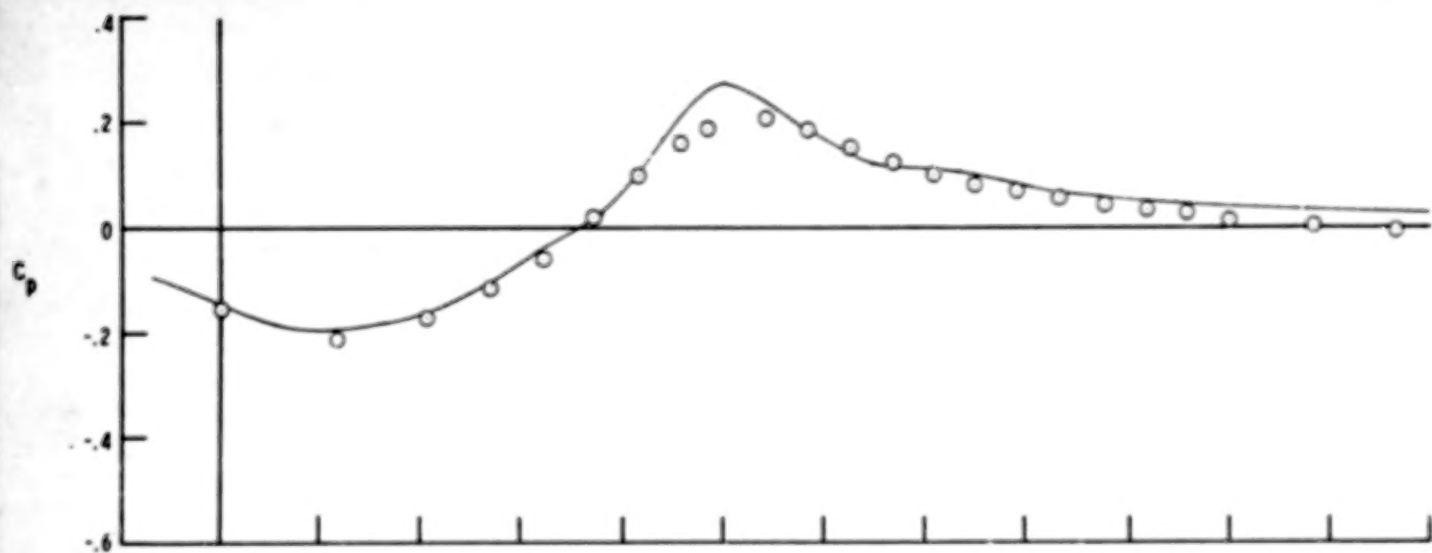
(a) $M_\infty = 0.40$.

Figure 11.- Comparison of theoretical and experimental pressure and cumulative drag distributions. Configuration 4; $x_l/d_m = 1.0$; $\beta_c = 11.0^\circ$.

39.
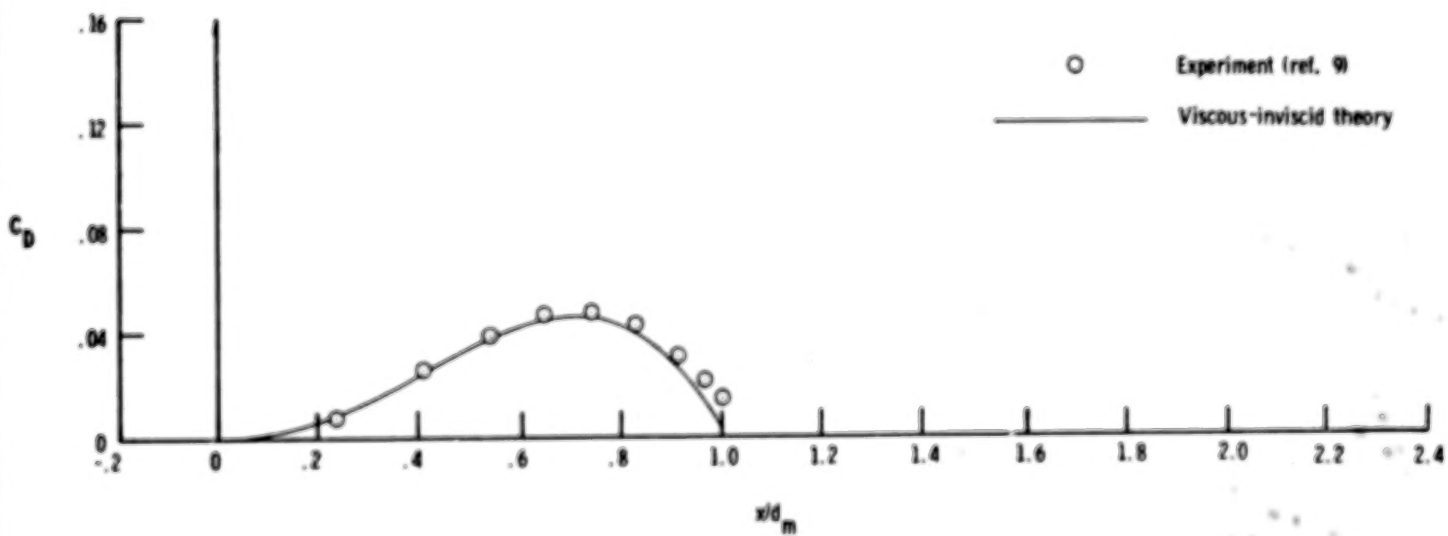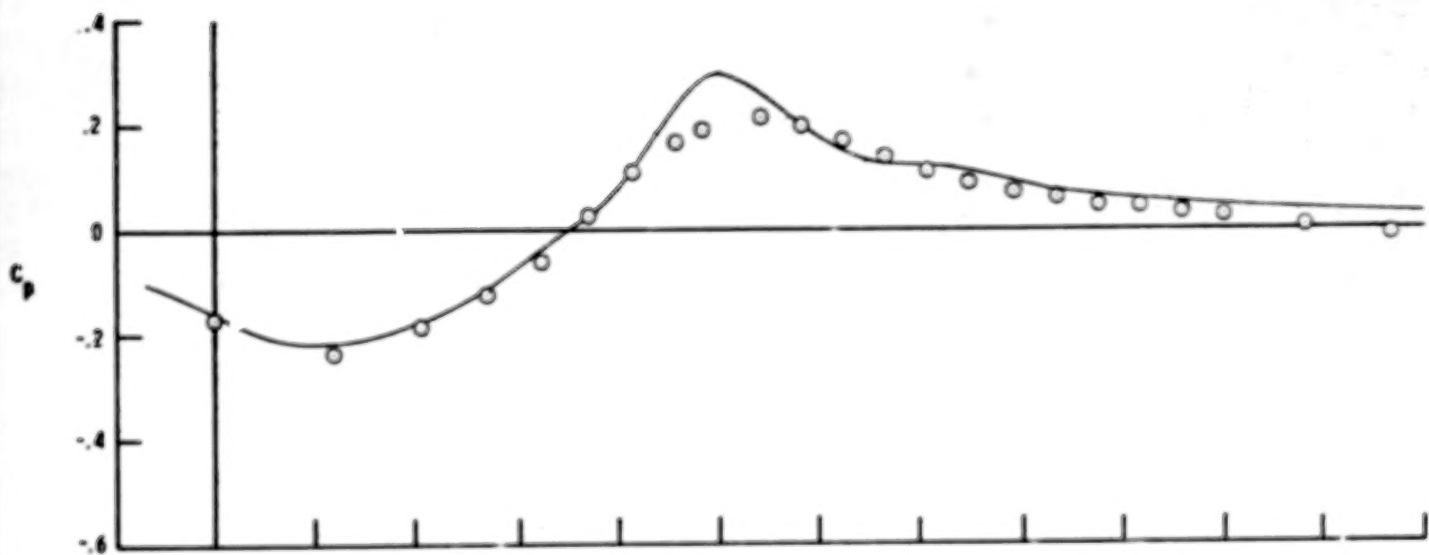
(b) $M_\infty = 0.60.$

Figure 11.- Continued.

40
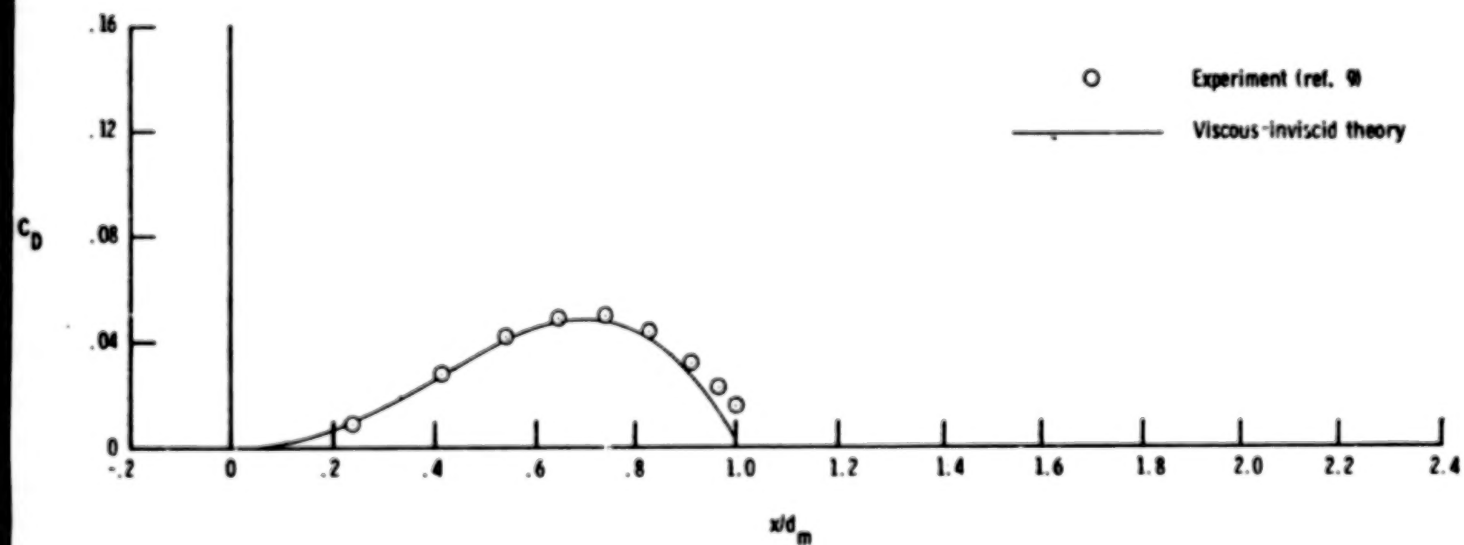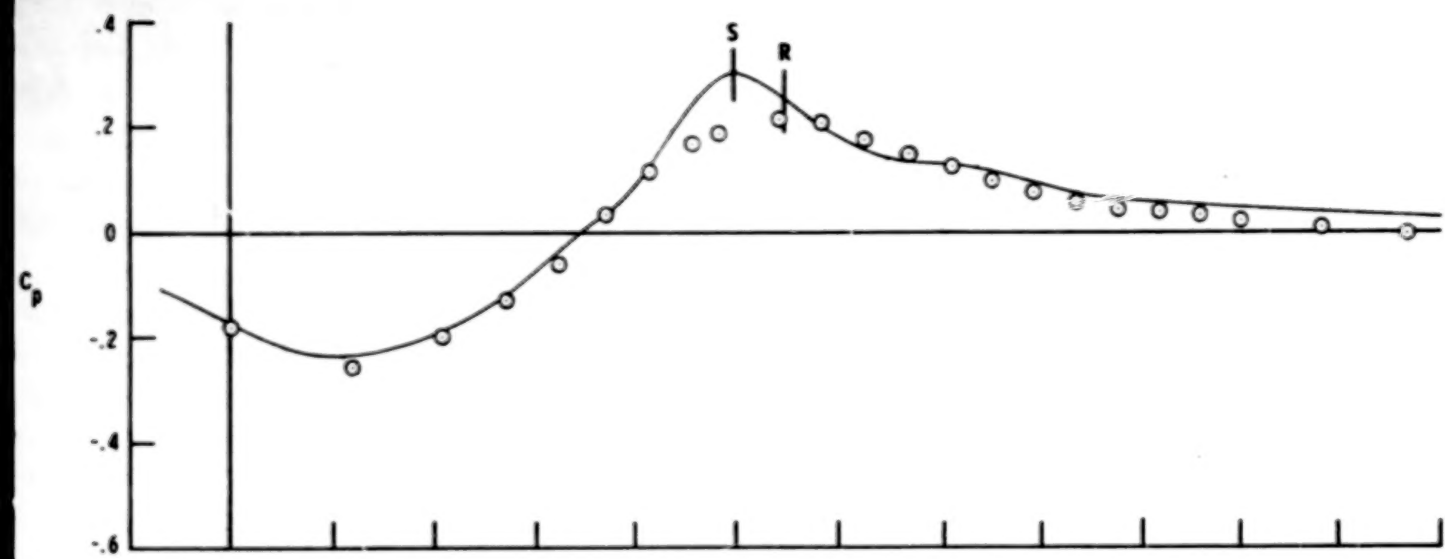
(c) $M_\infty = 0.70$.

Figure 11.- Continued.

41.
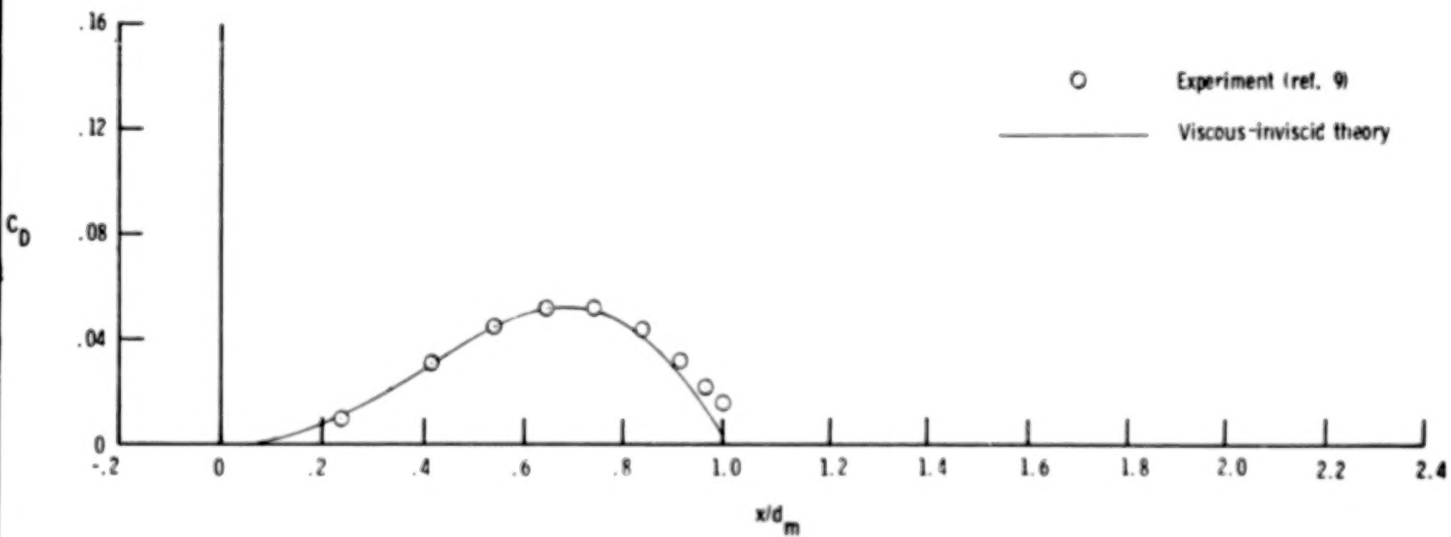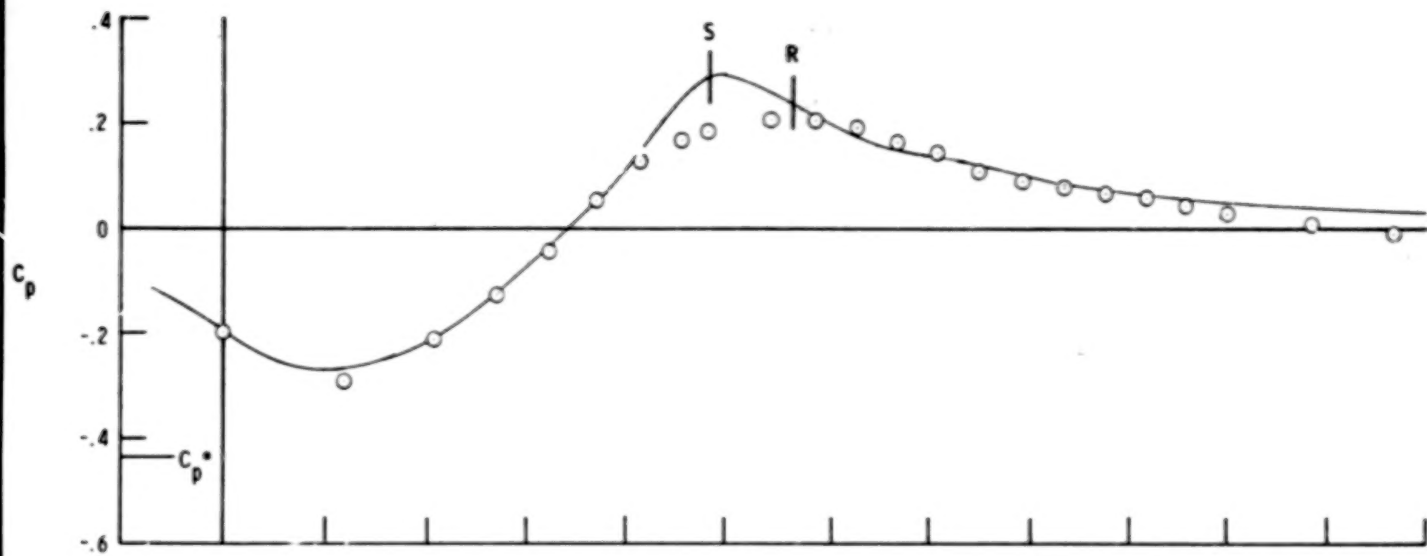
(d) $M_\infty = 0.80$.

Figure 11.- Continued.

42
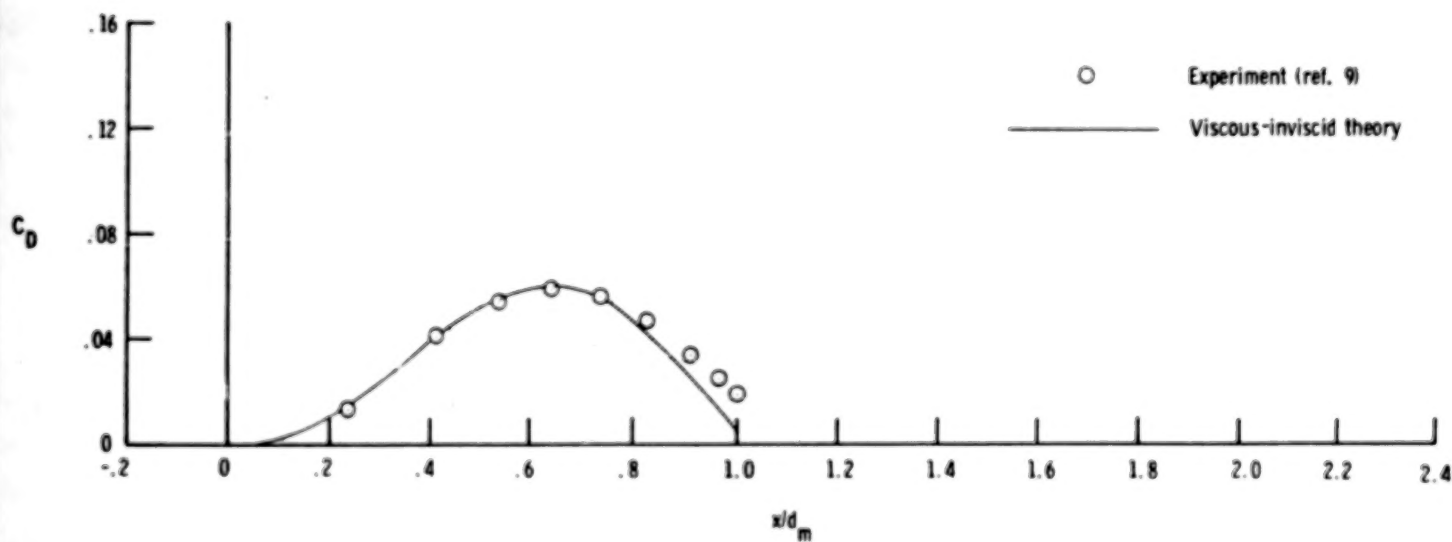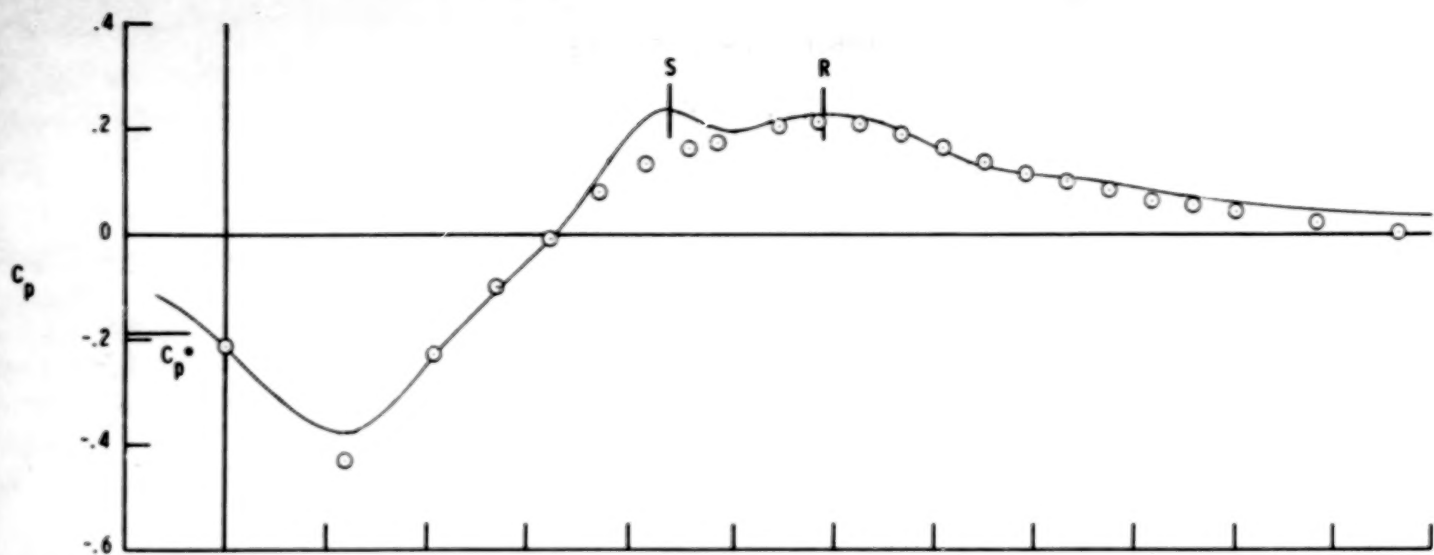
(e) $M_{\infty} = 0.90$.

Figure 11.- Continued.

43.
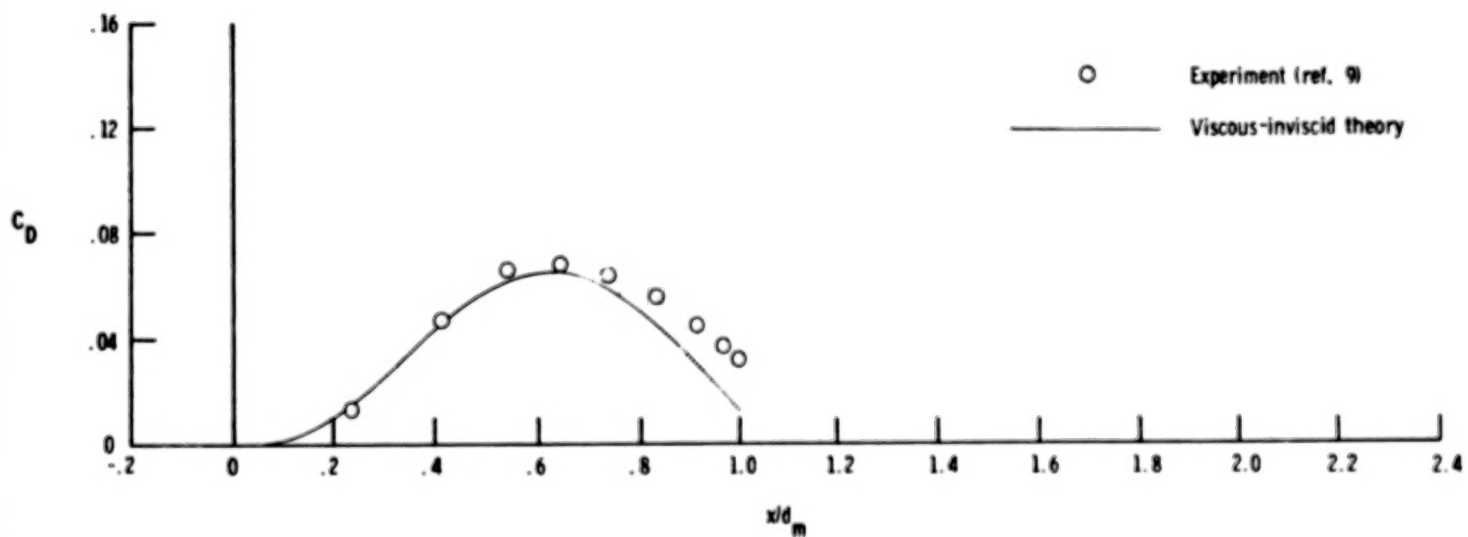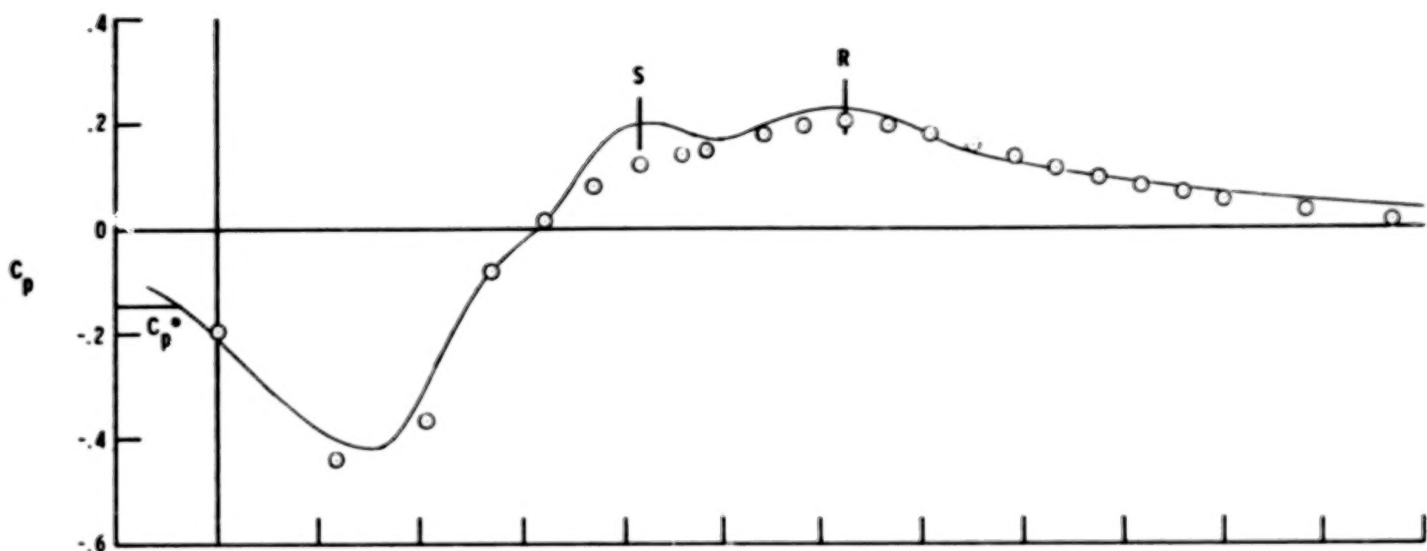
(f) $M_\infty = 0.92$.

Figure 11.- Continued.

44.
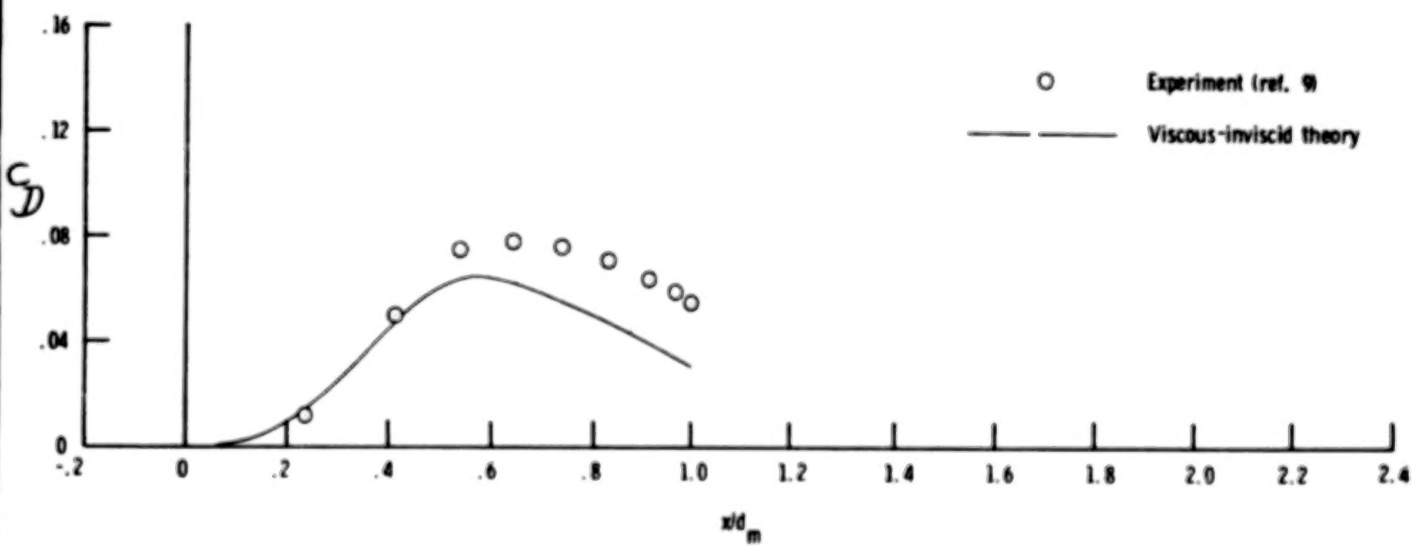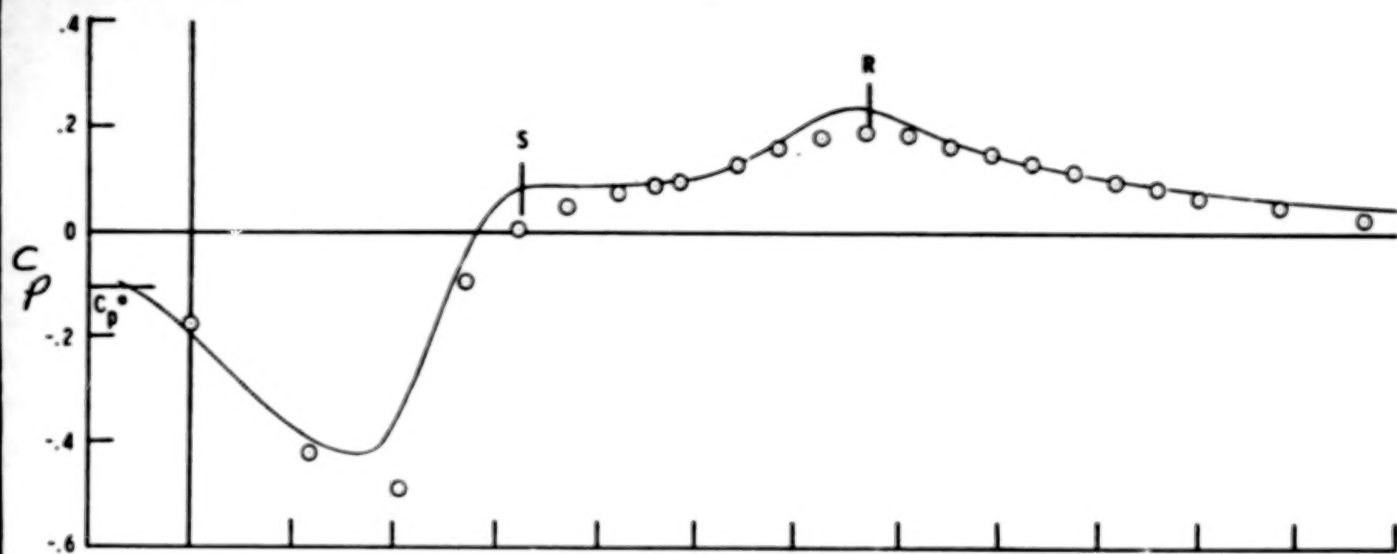
(g) $M_\infty = 0.94$.

Figure 11.- Concluded.

45.
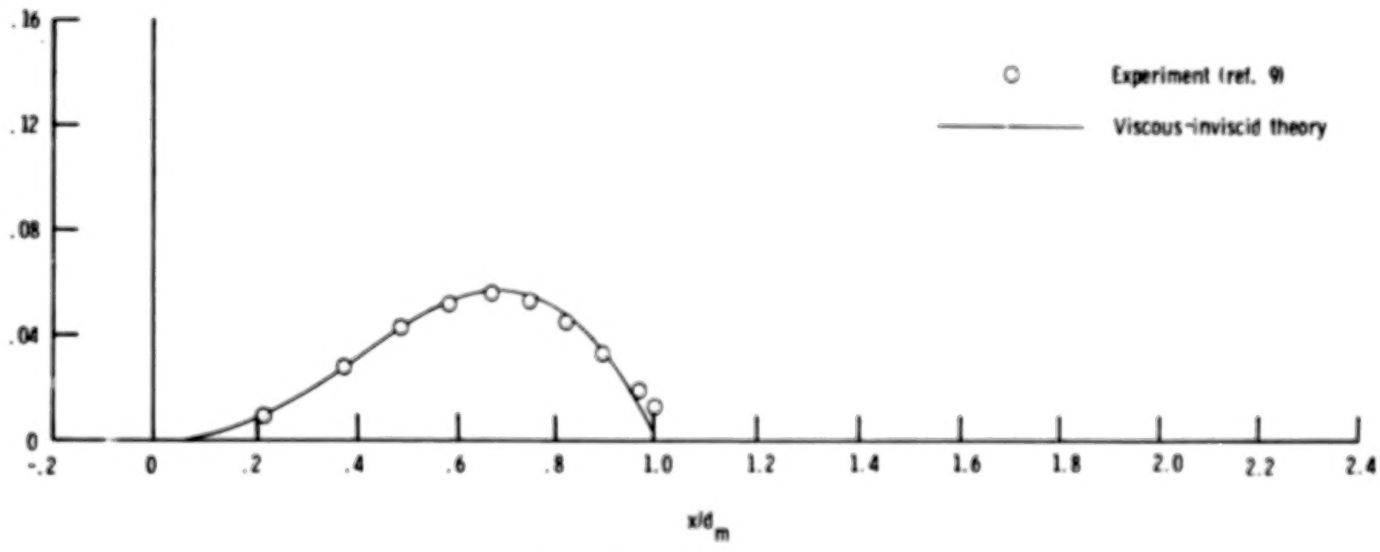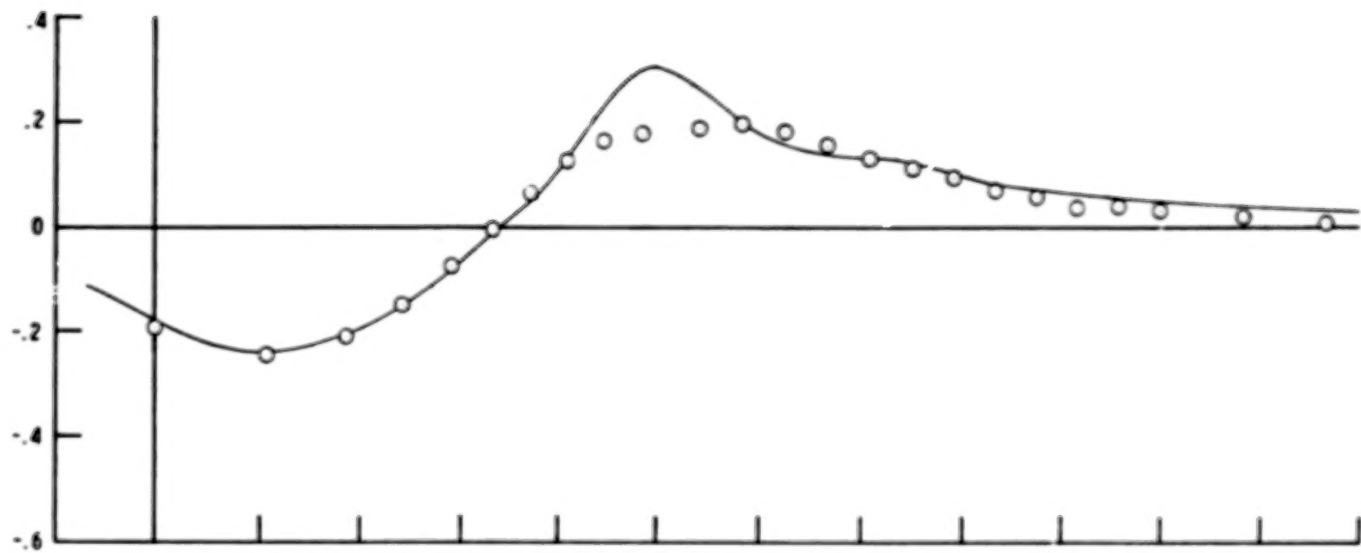
(a) $M_\infty = 0.40$.

Figure 12.- Comparison of theoretical and experimental pressure and cumulative drag distributions.
Configuration 2; $x_l/d_m = 1.0$; $\beta_c = 13.8^\circ$.
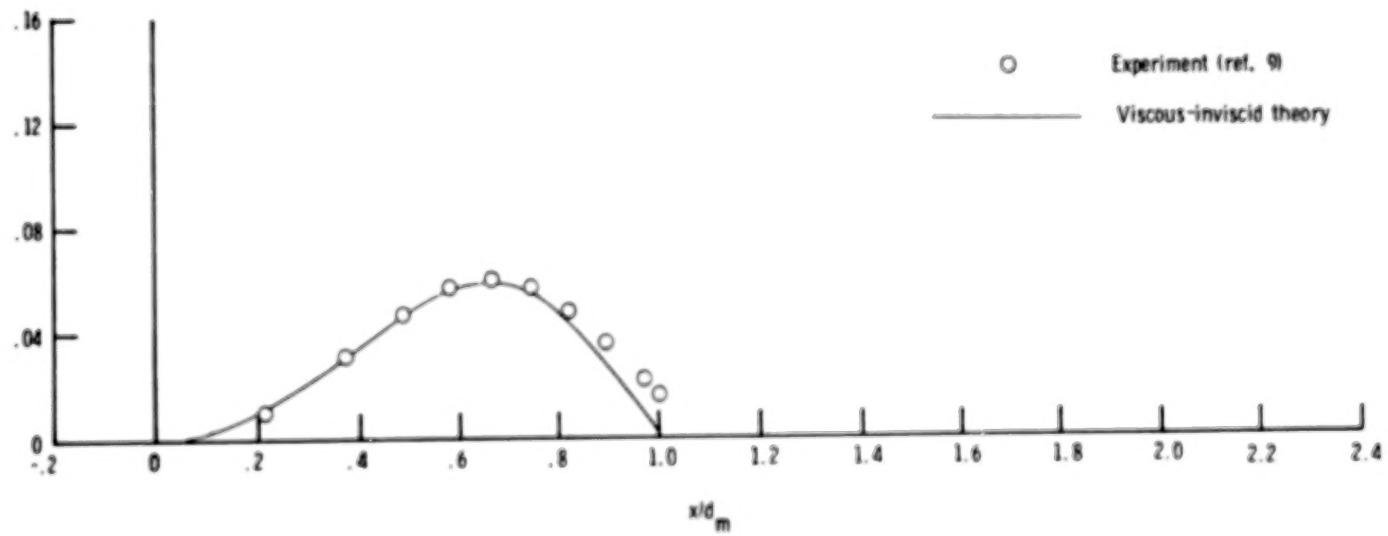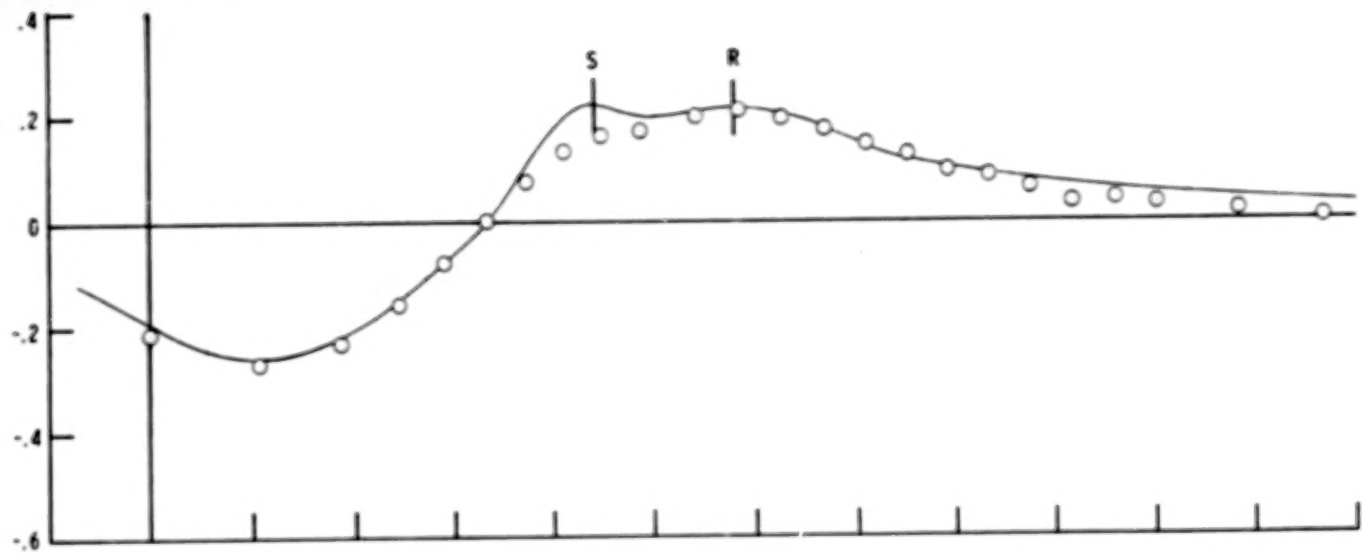
(b) $M_\infty = 0.60$.

Figure 12.- Continued.

47.
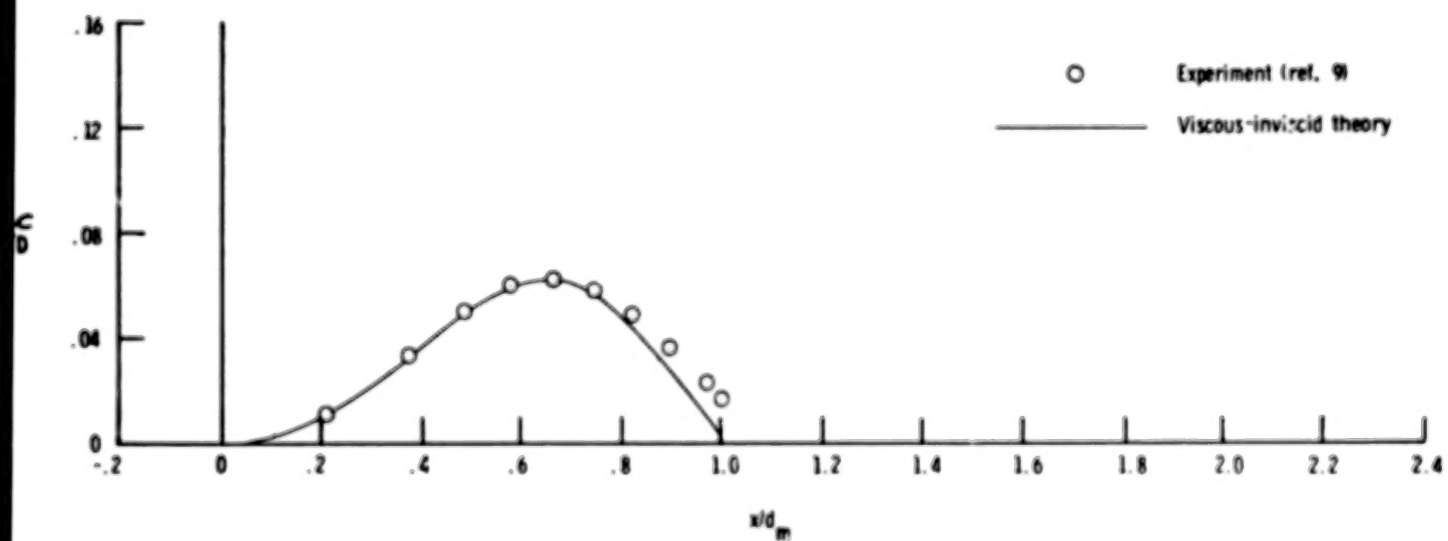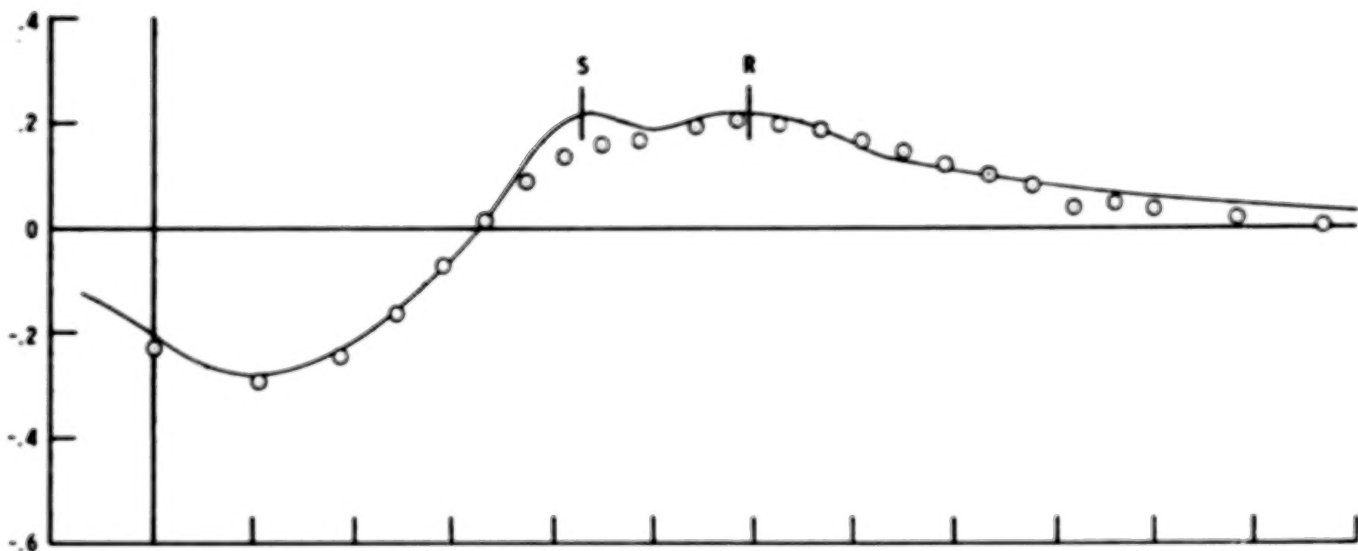
(c) $M_\infty = 0.70$.

Figure 12.- Continued.

48.
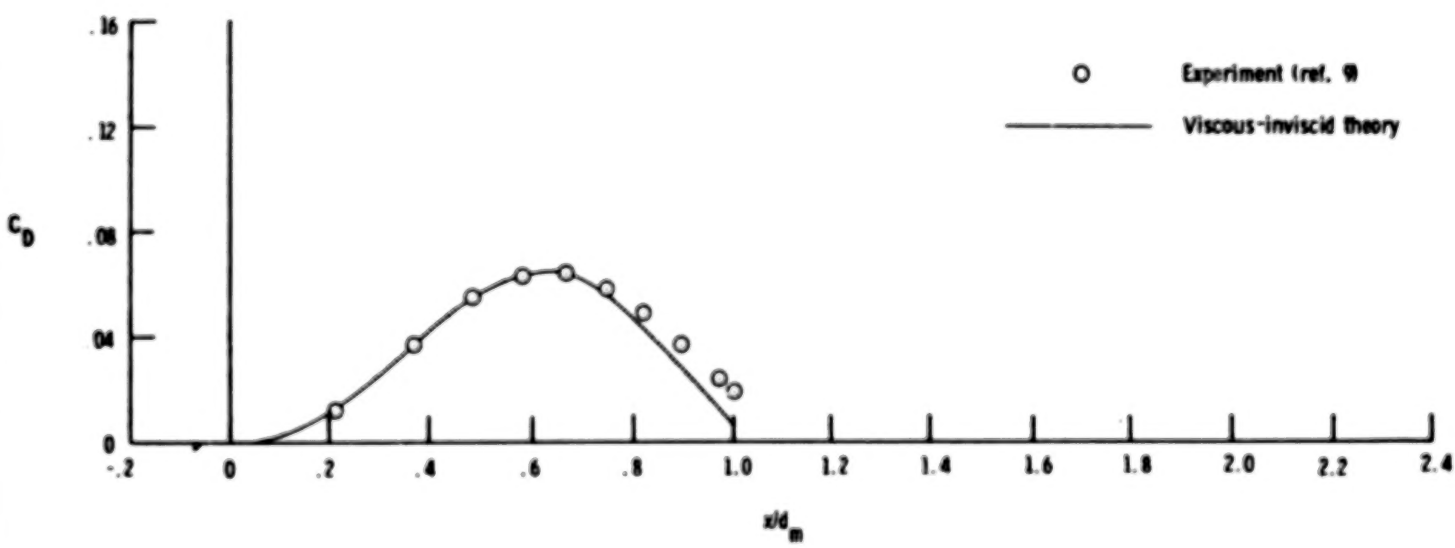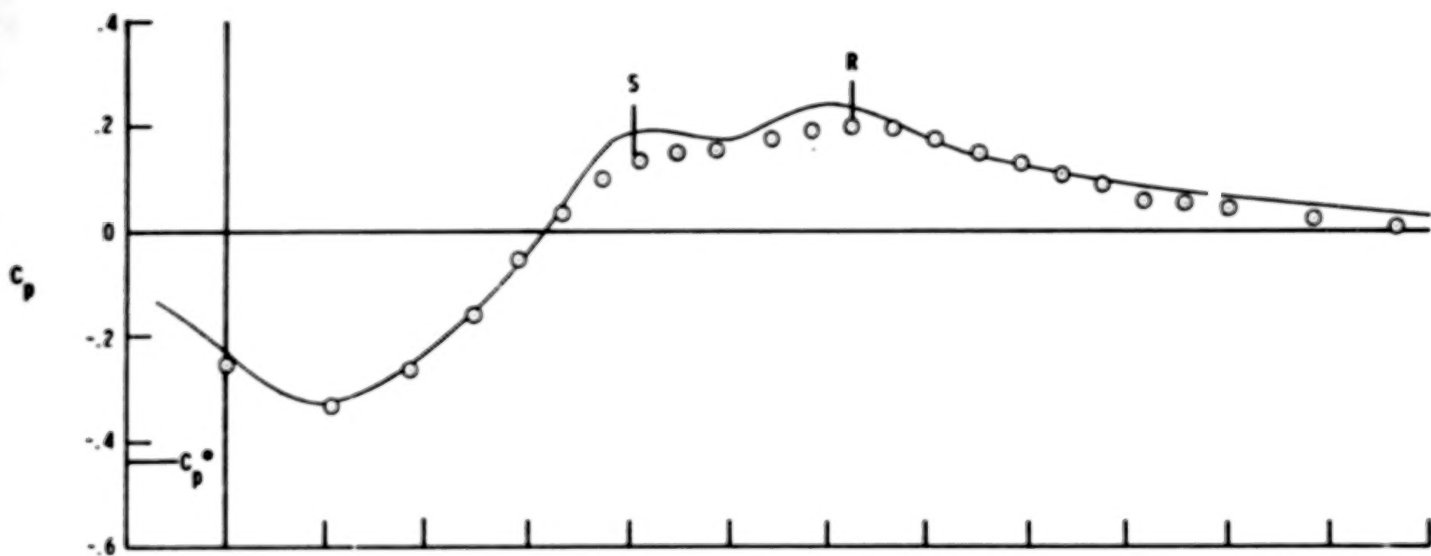
(d) $M_\infty = 0.80$.

Figure 12.- Continued.

49.
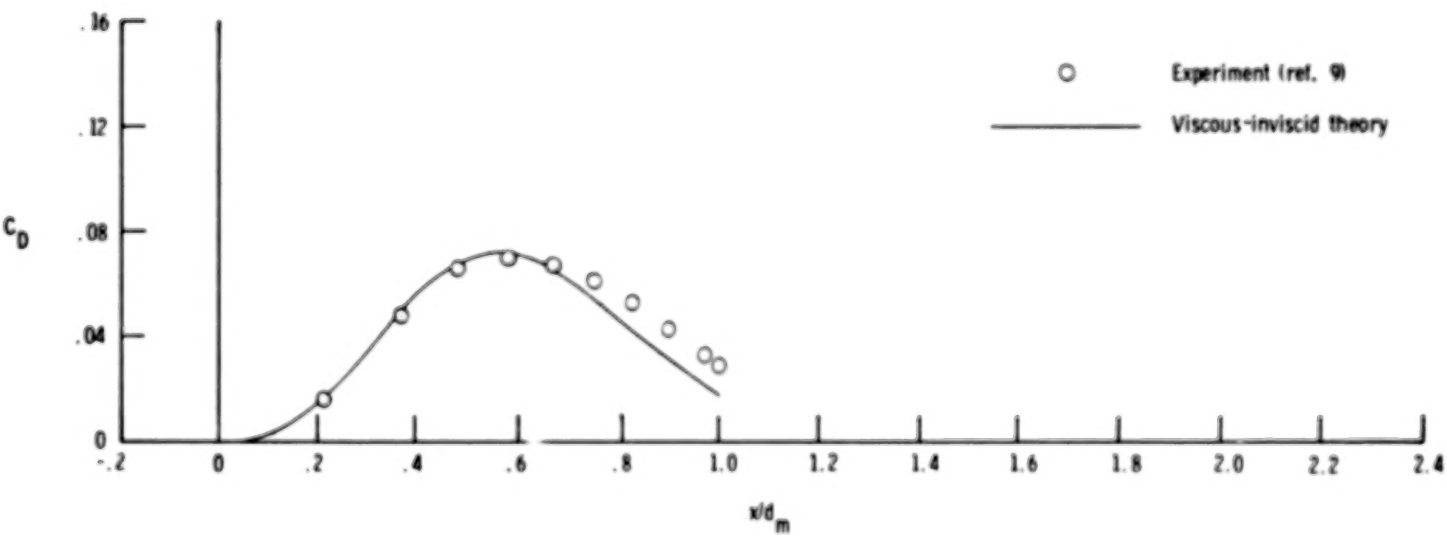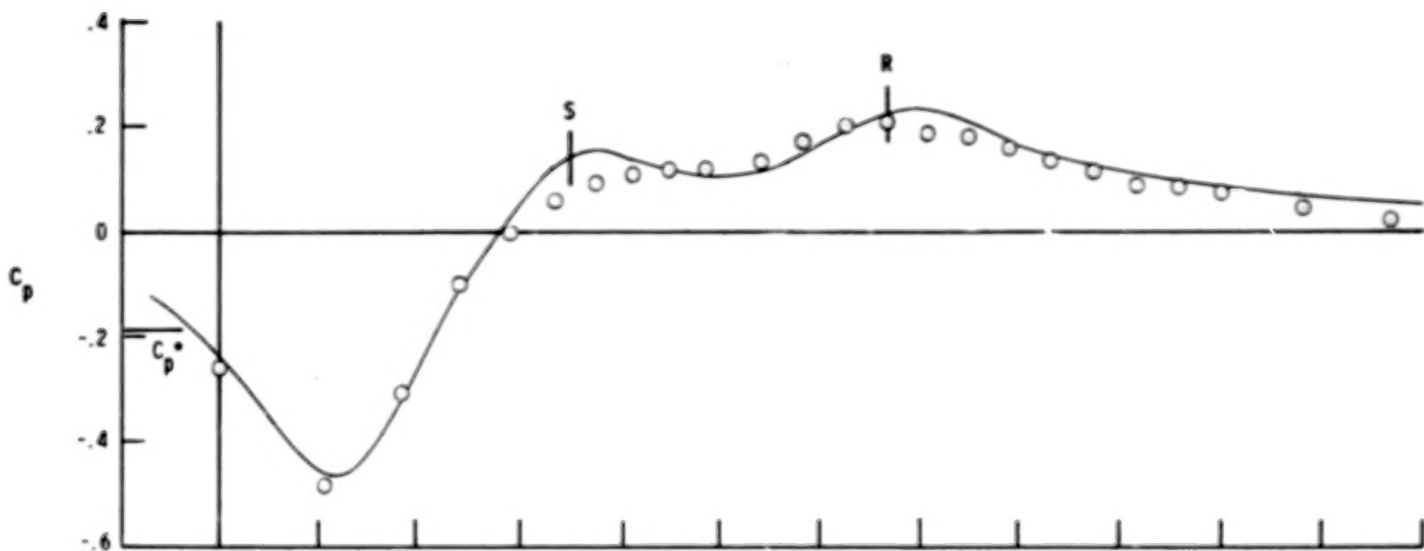
(e) $M_\infty = 0.90$.

Figure 12.- Continued.

50.
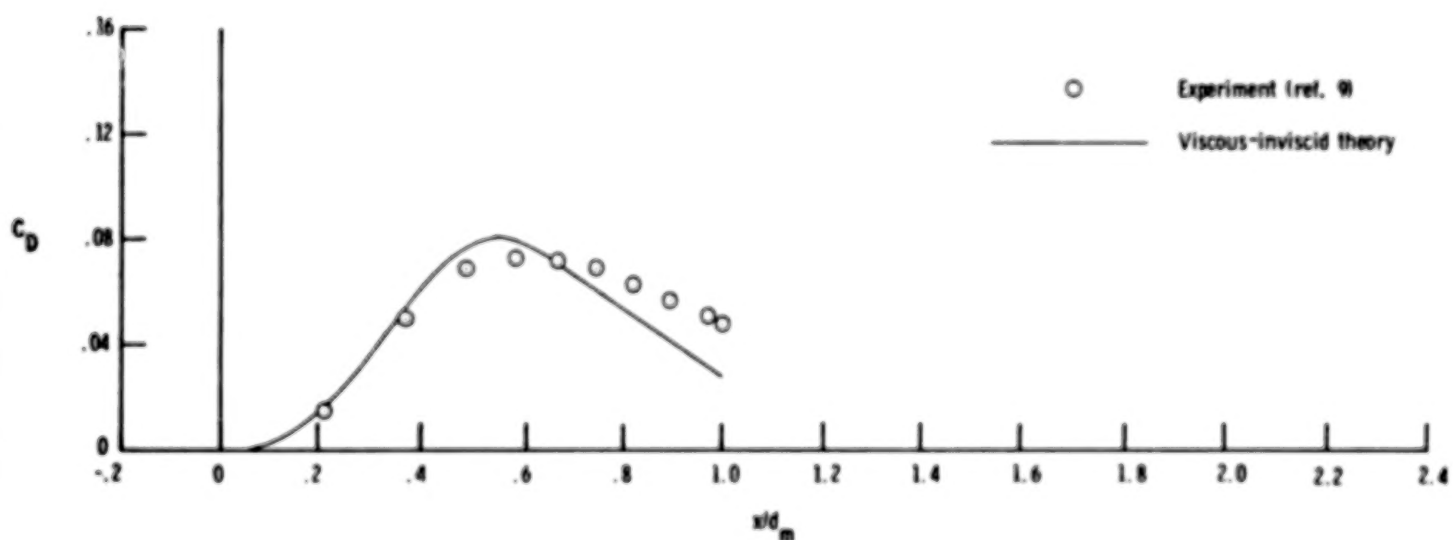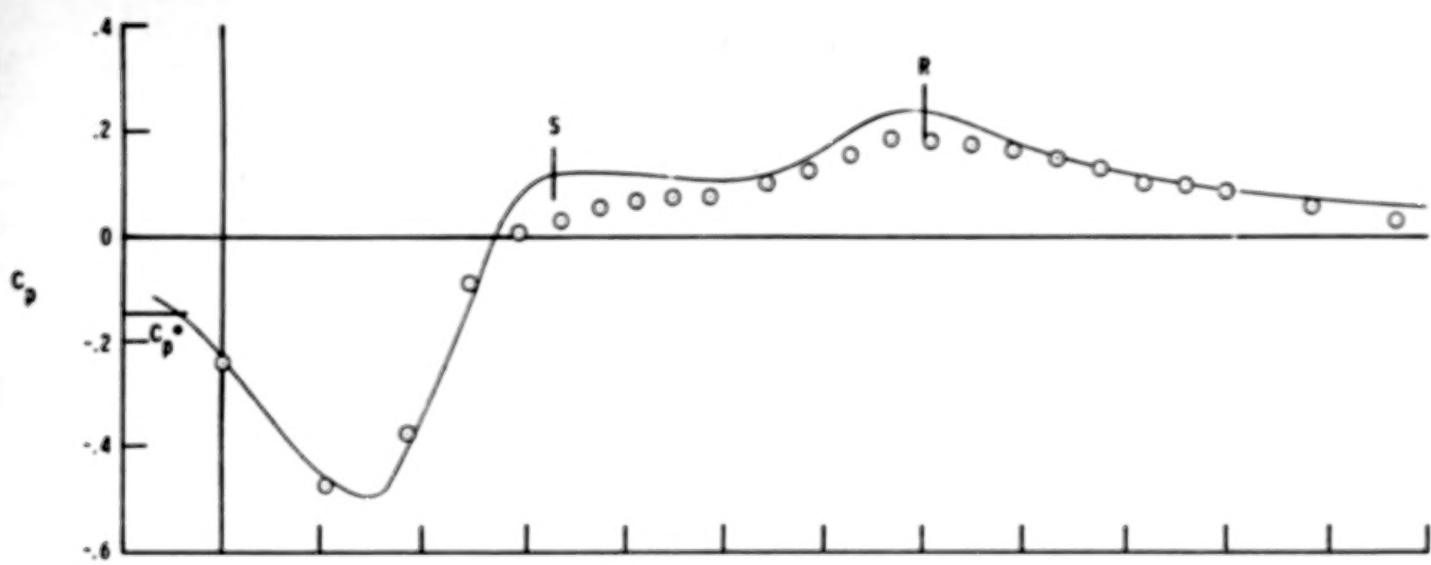
(f) $M_\infty = 0.92$.

Figure 12.- Continued.

51
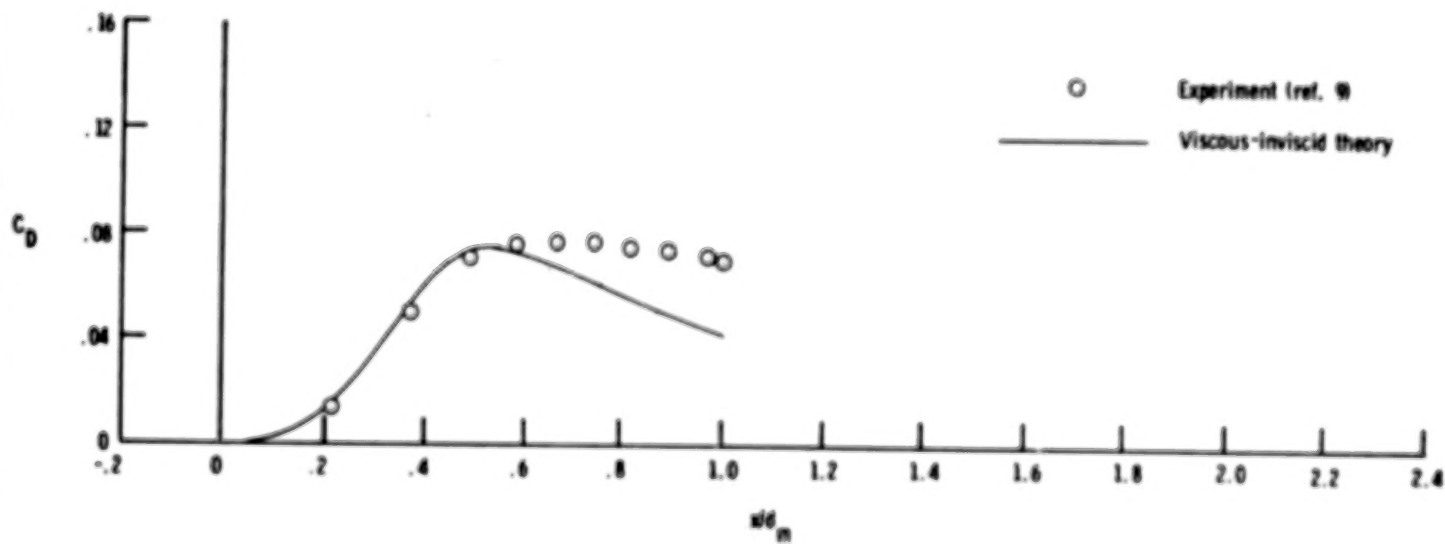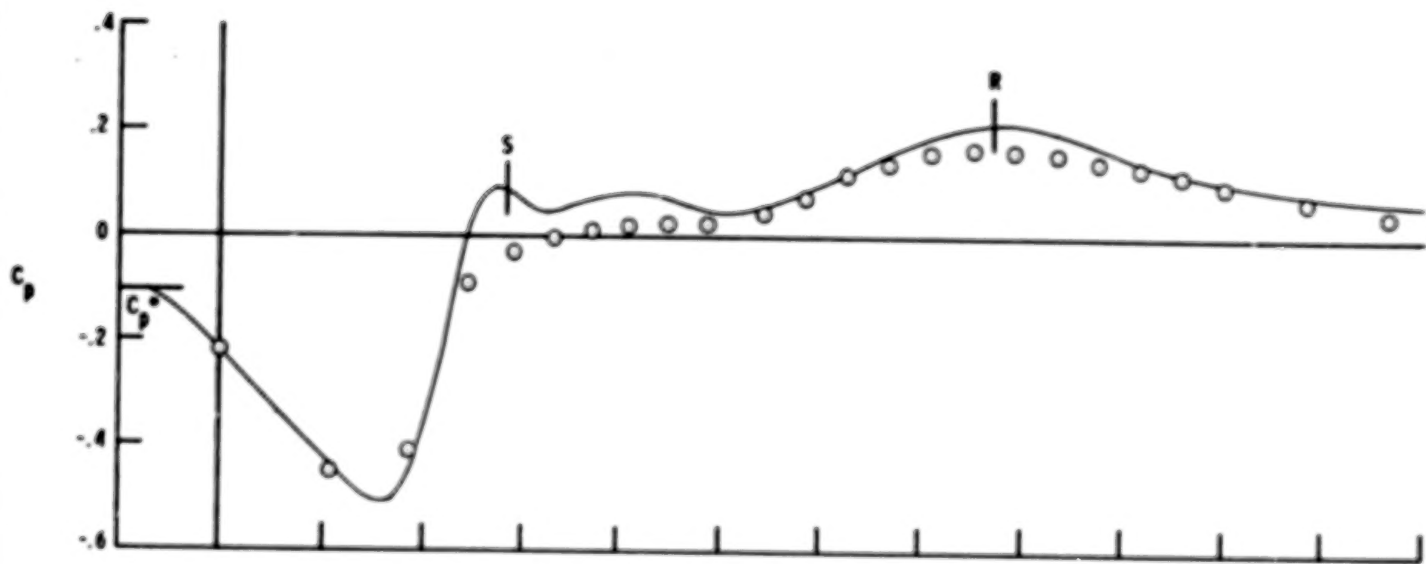
(g) $M_\infty = 0.94$.

Figure 12.- Continued.

52.
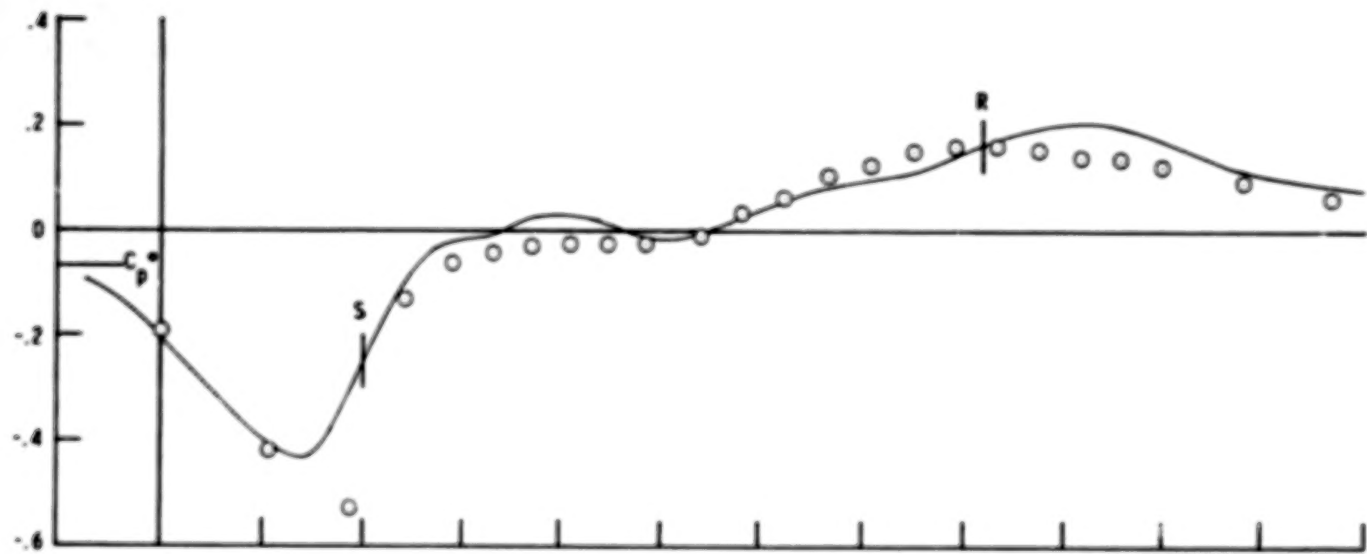
(h) $M_{\infty} = 0.96$.

Figure 12.- Concluded.

53
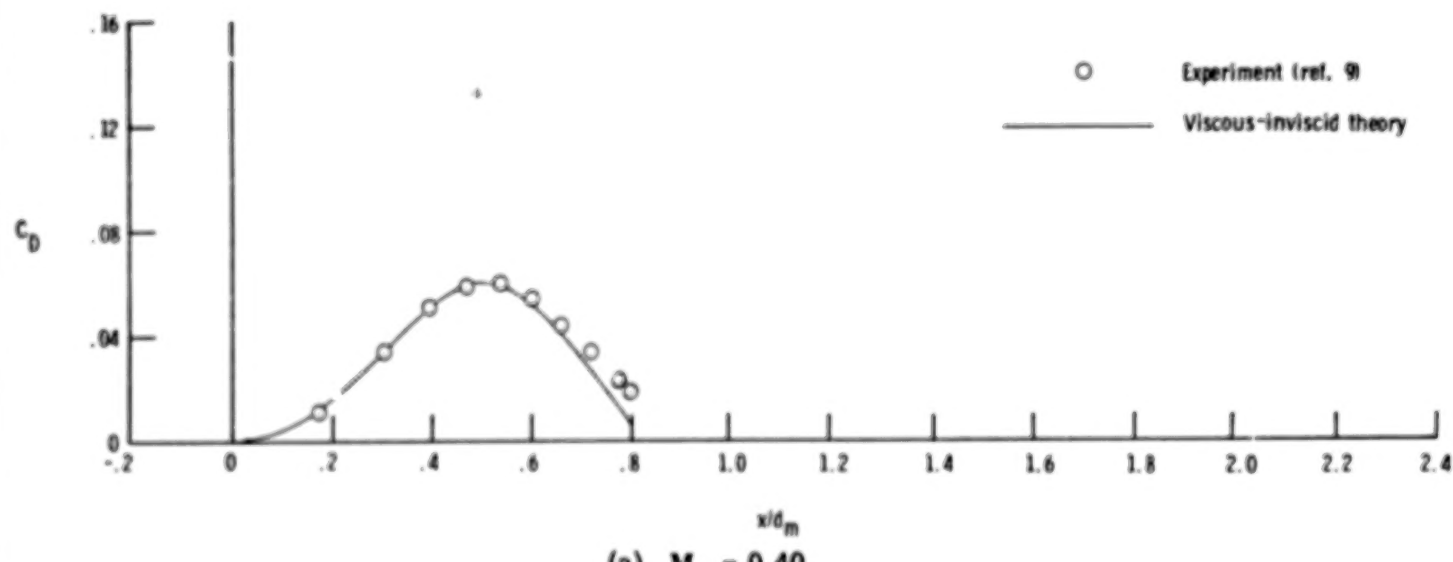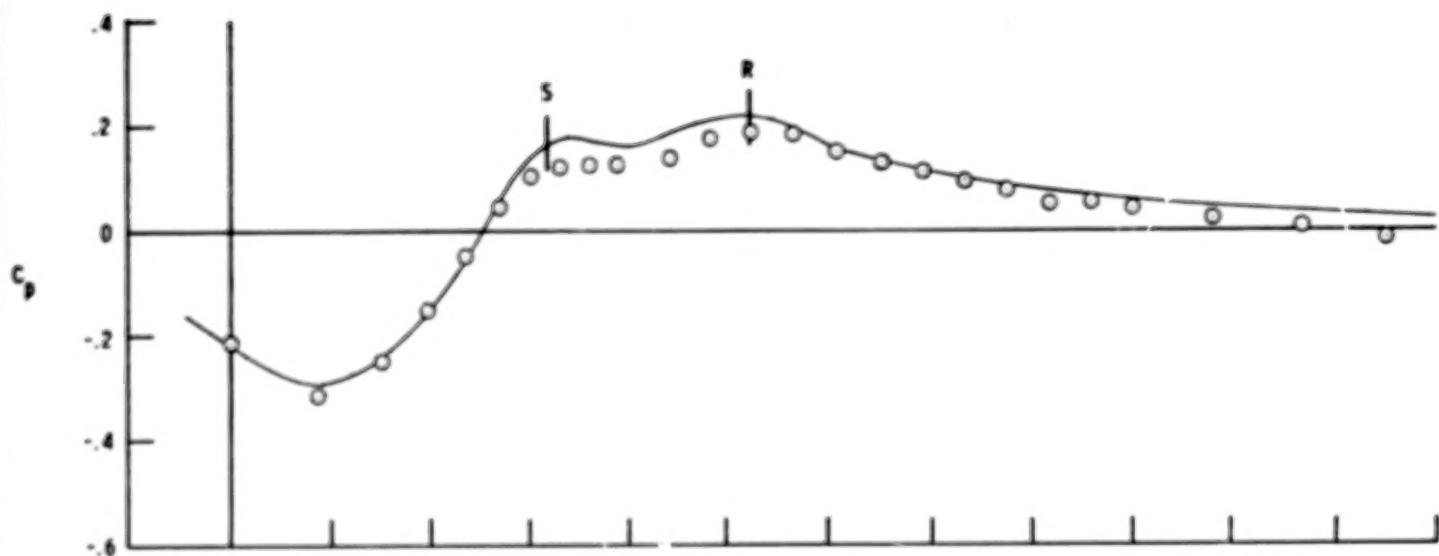
(a) $M_\infty = 0.40$.

Figure 13.- Comparison of theoretical and experimental pressure and cumulative drag distributions. Configuration 1; $x_l/d_m = 0.8$; $\beta_c = 17.0^o$.

54
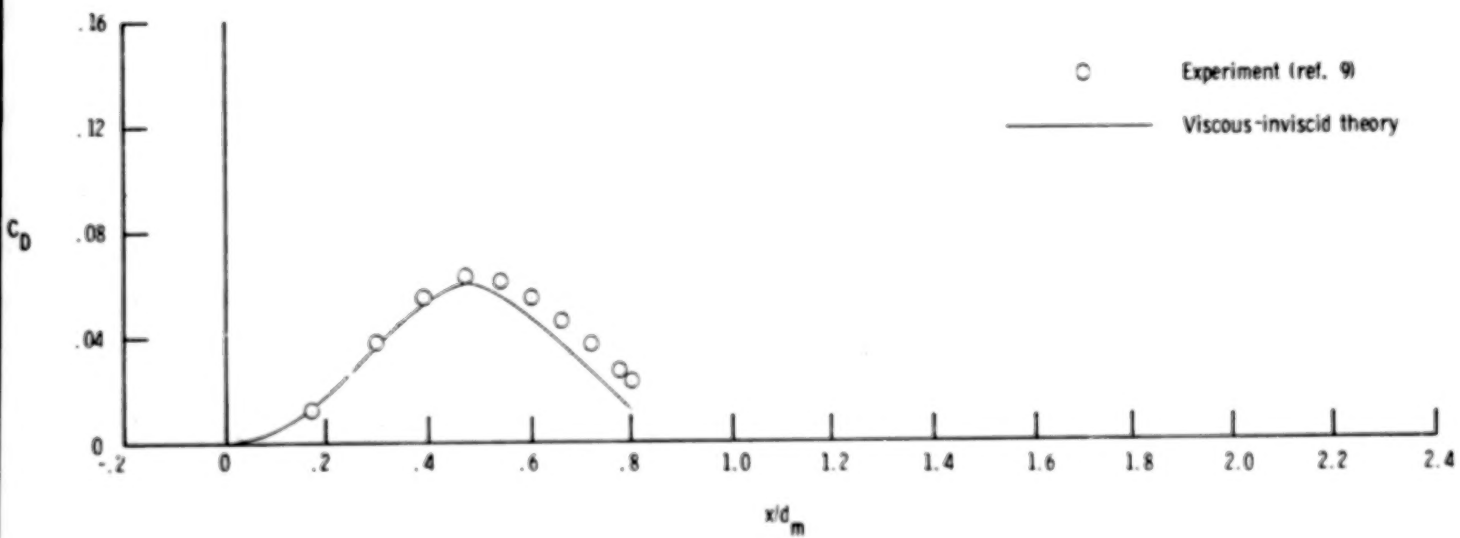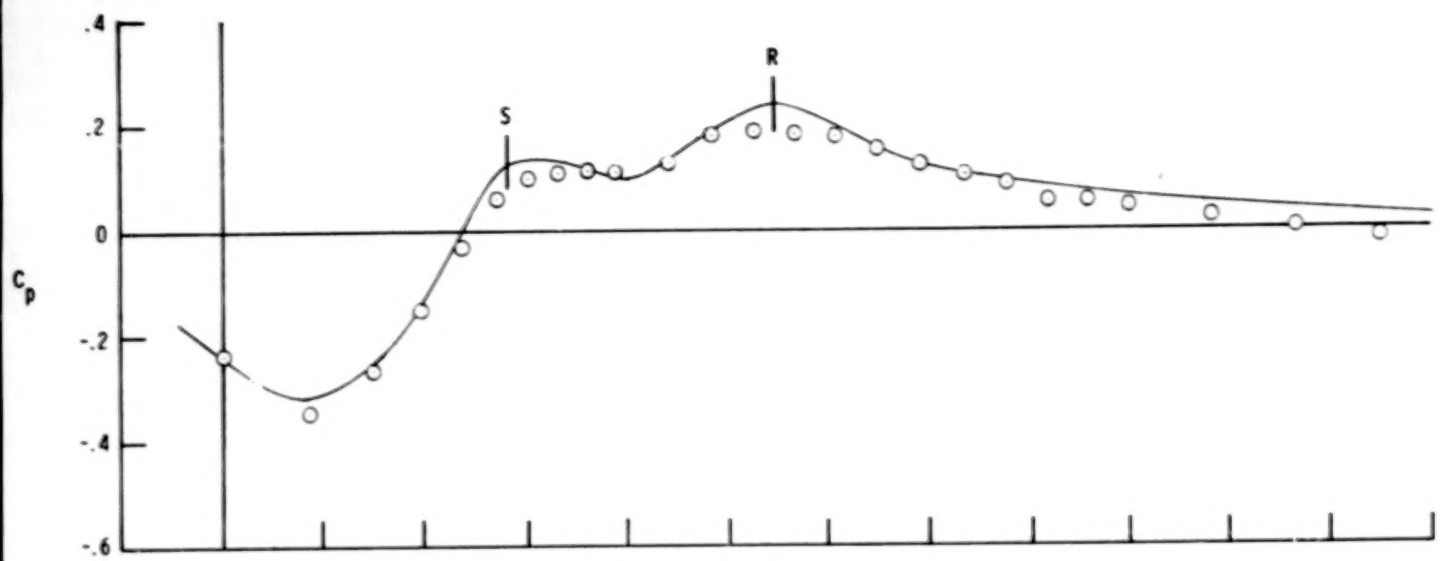
(b) $M_\infty = 0.60$.

Figure 13.- Continued.

55.
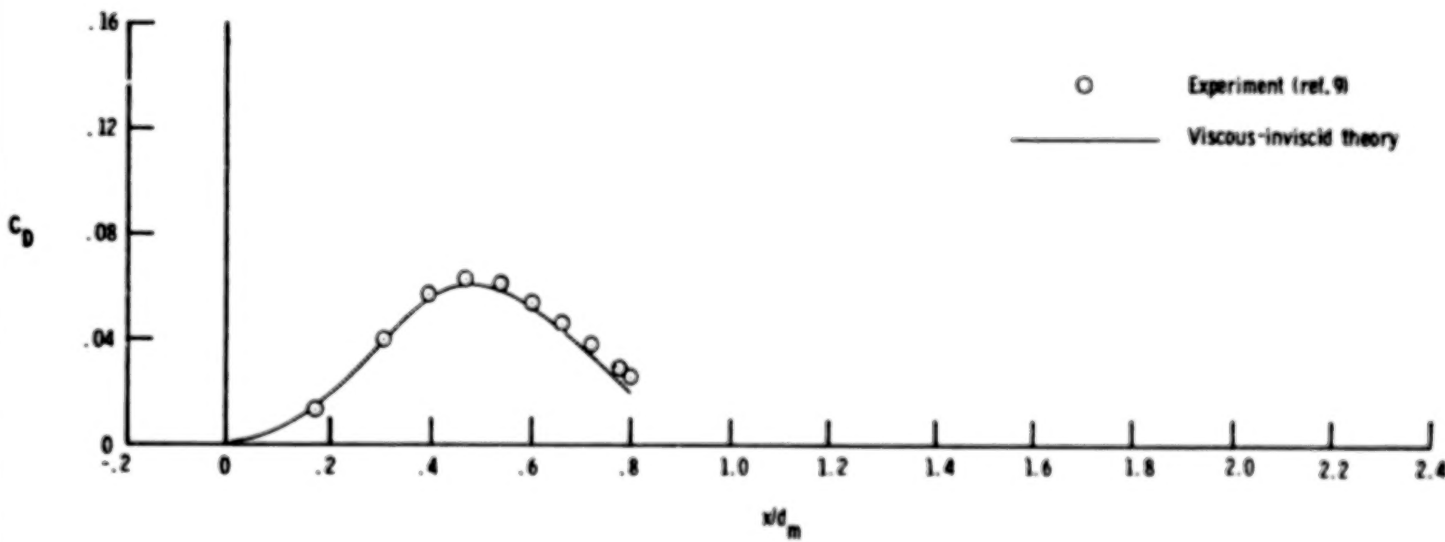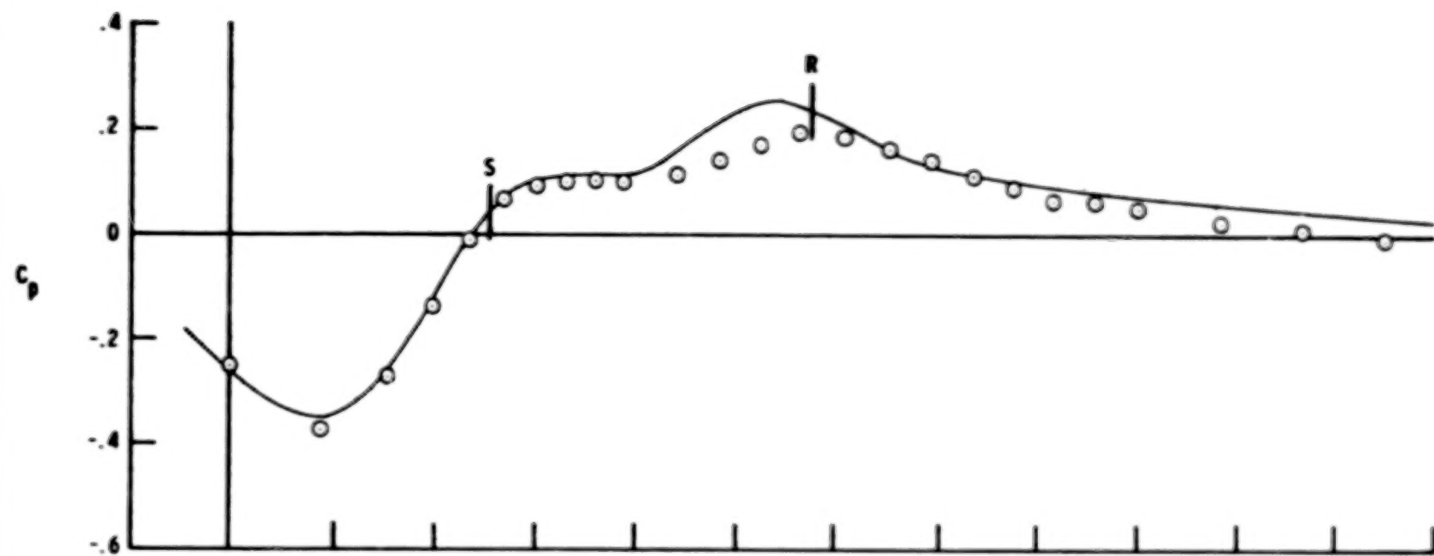
(c) $M_\infty = 0.70$.

Figure 13.- Continued.

56.
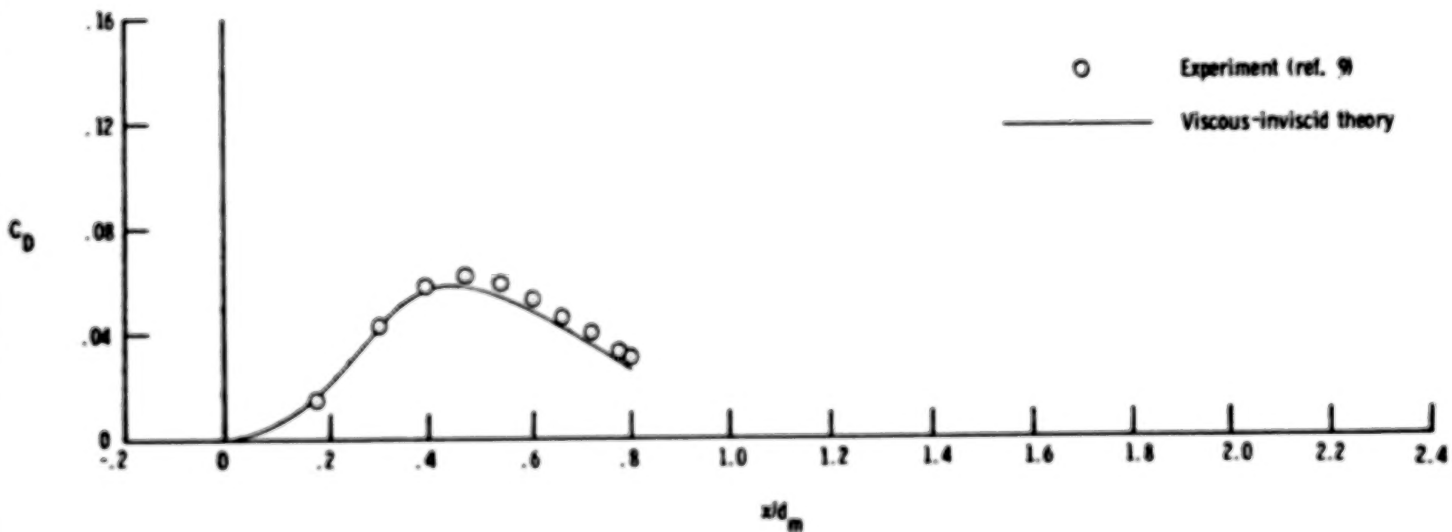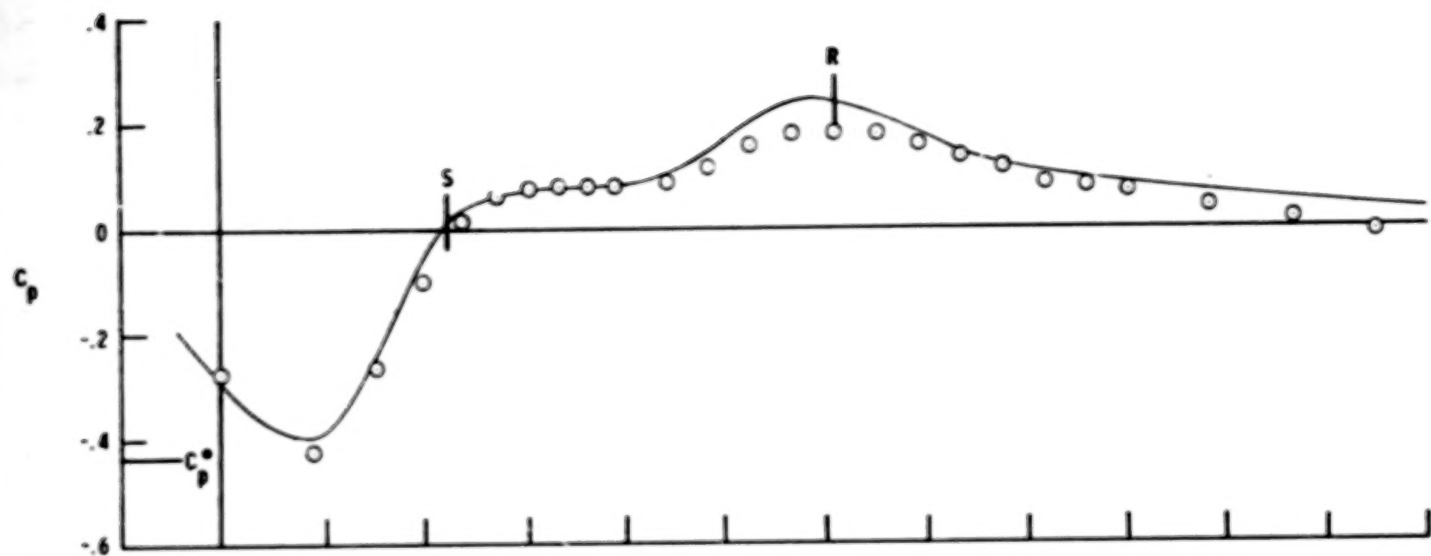
(d) $M_\infty = 0.80.$

Figure 13.- Continued.

57.
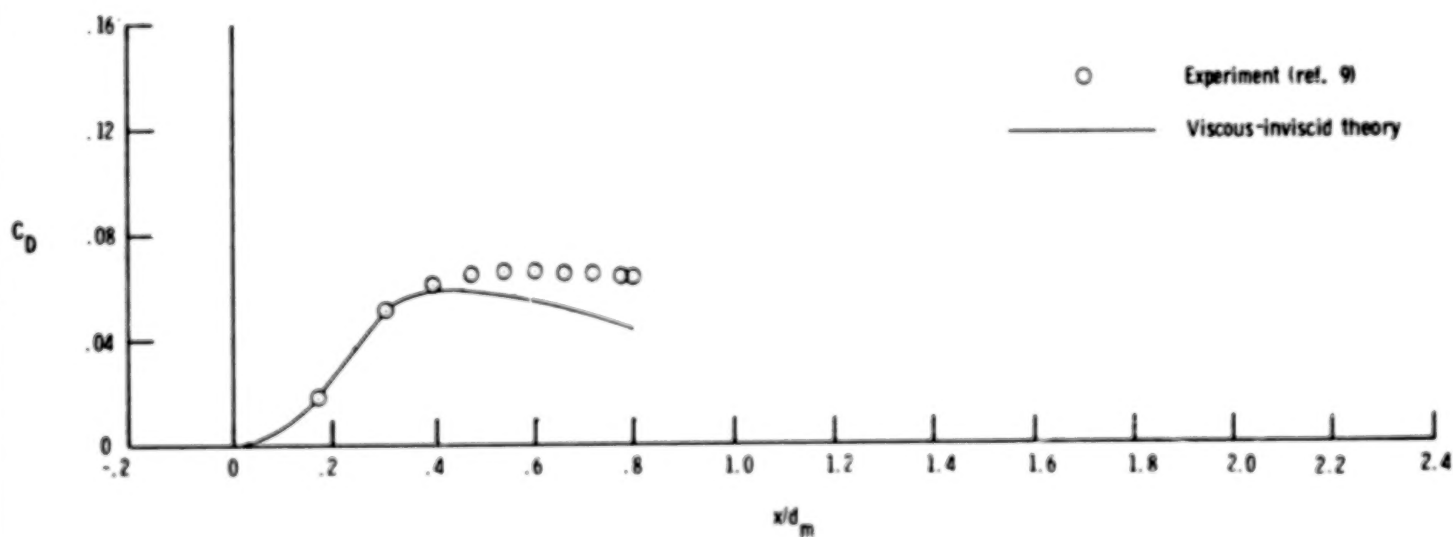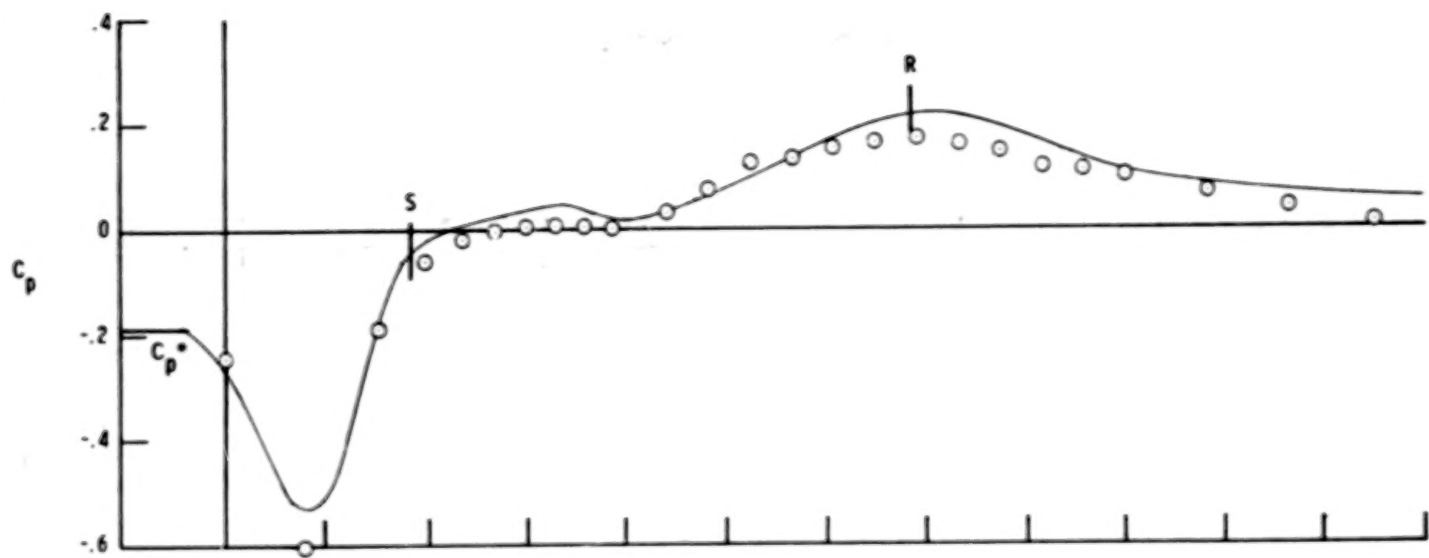
(e) $M_\infty = 0.90$.

Figure 13.- Continued.

58.
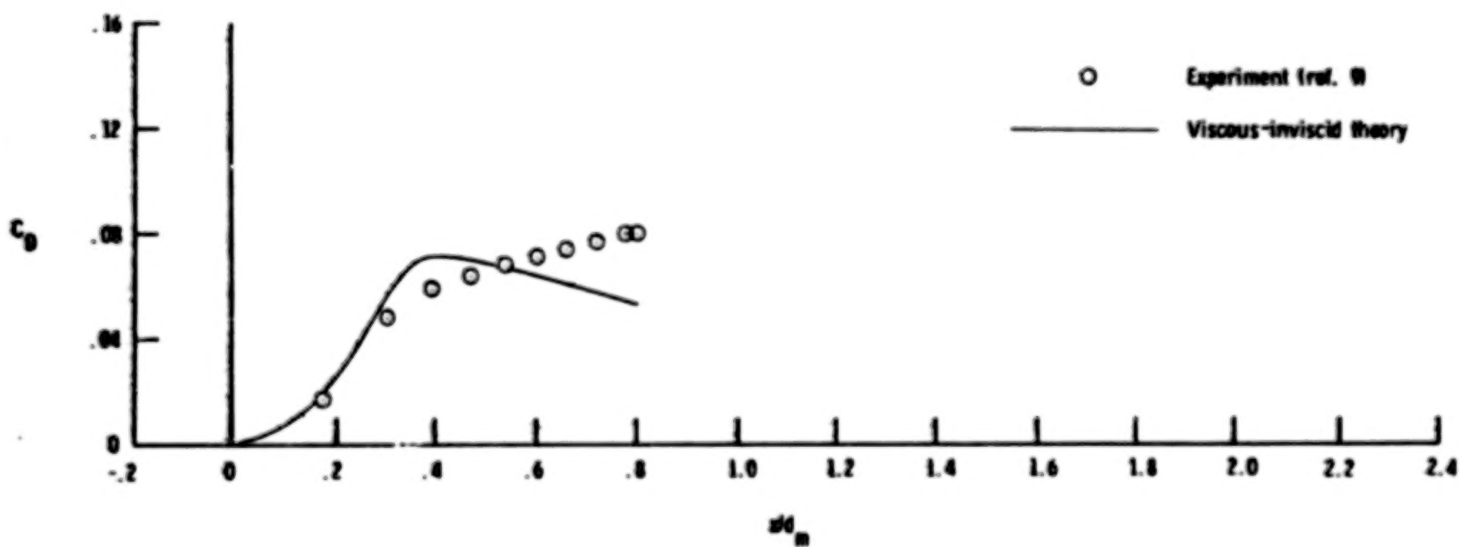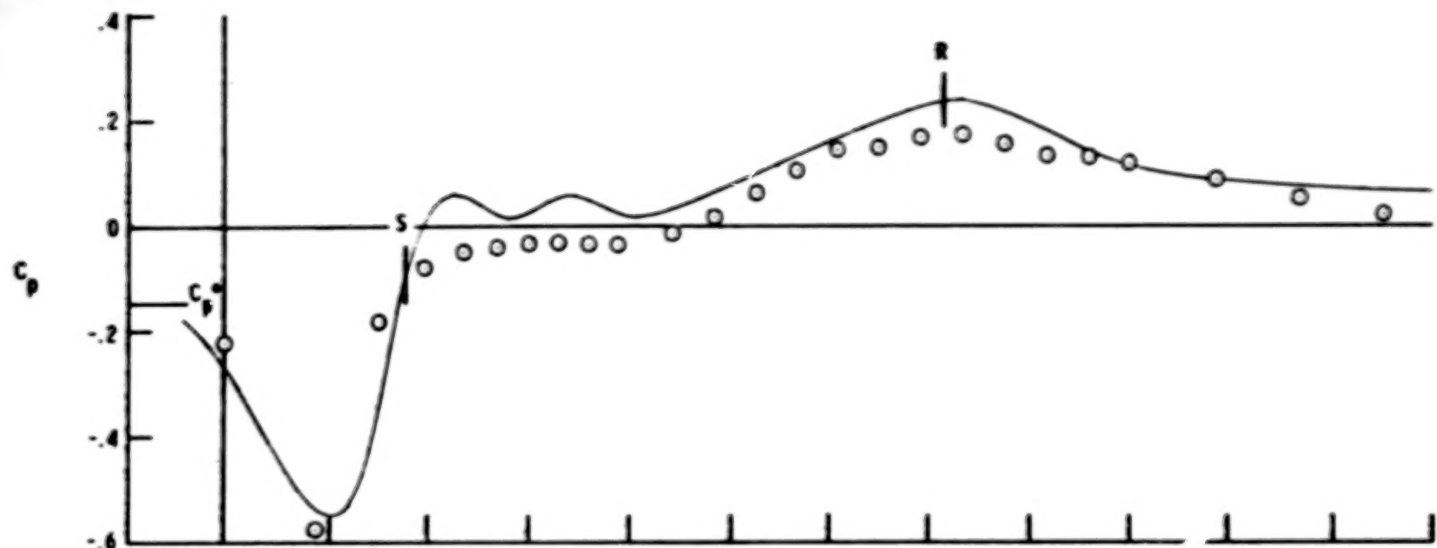
(f) $M_{\infty} = 0.92$.

Figure 13.- Continued.

59
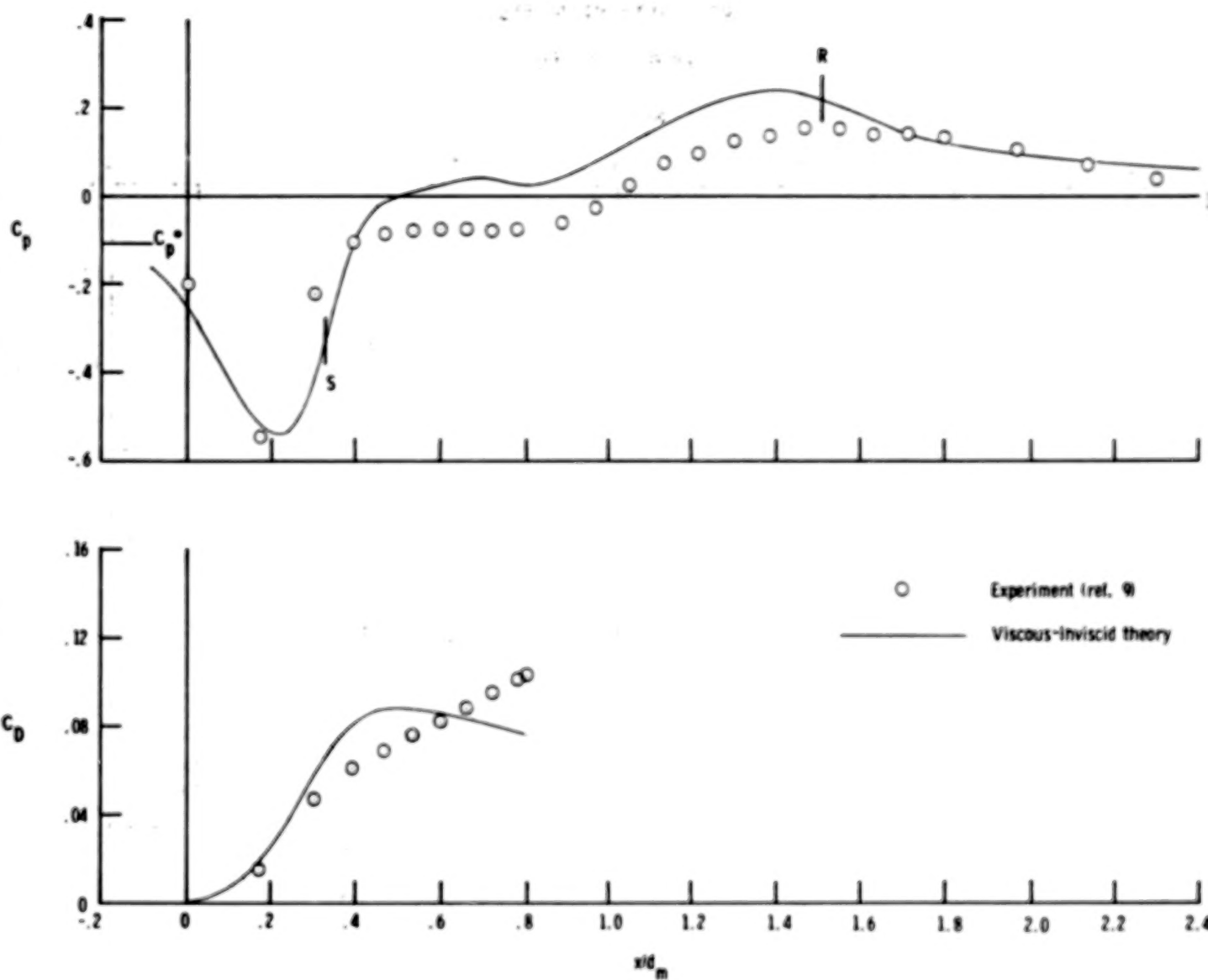
(g) $M_\infty = 0.94$.

Figure 13.- Continued.

60
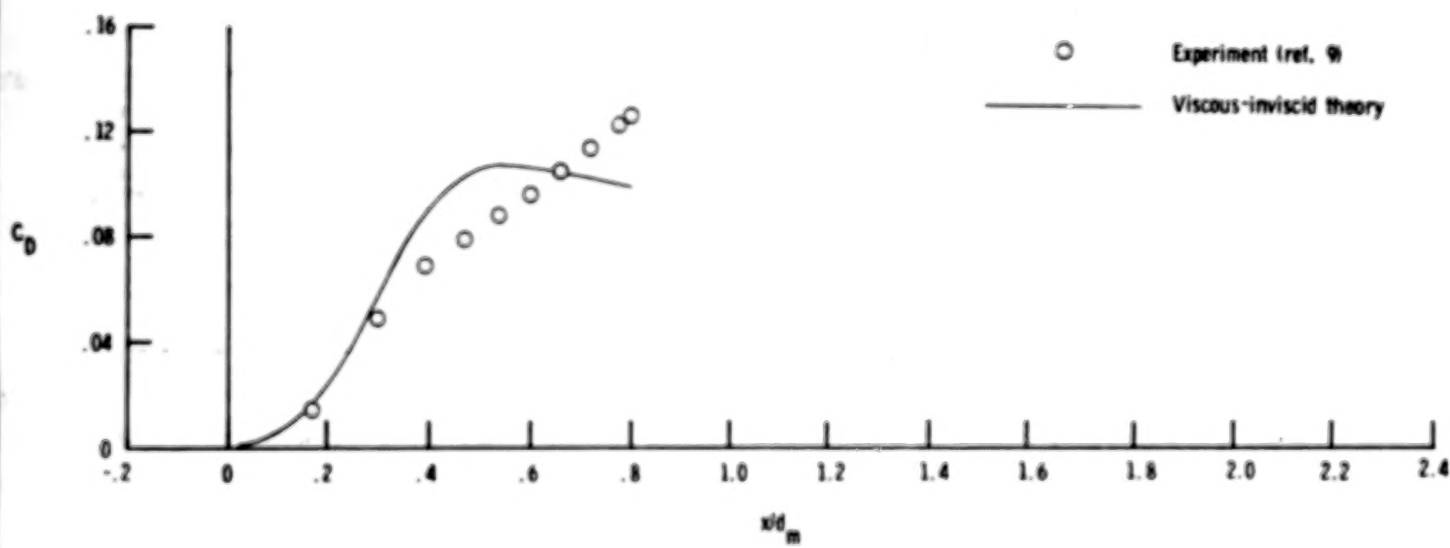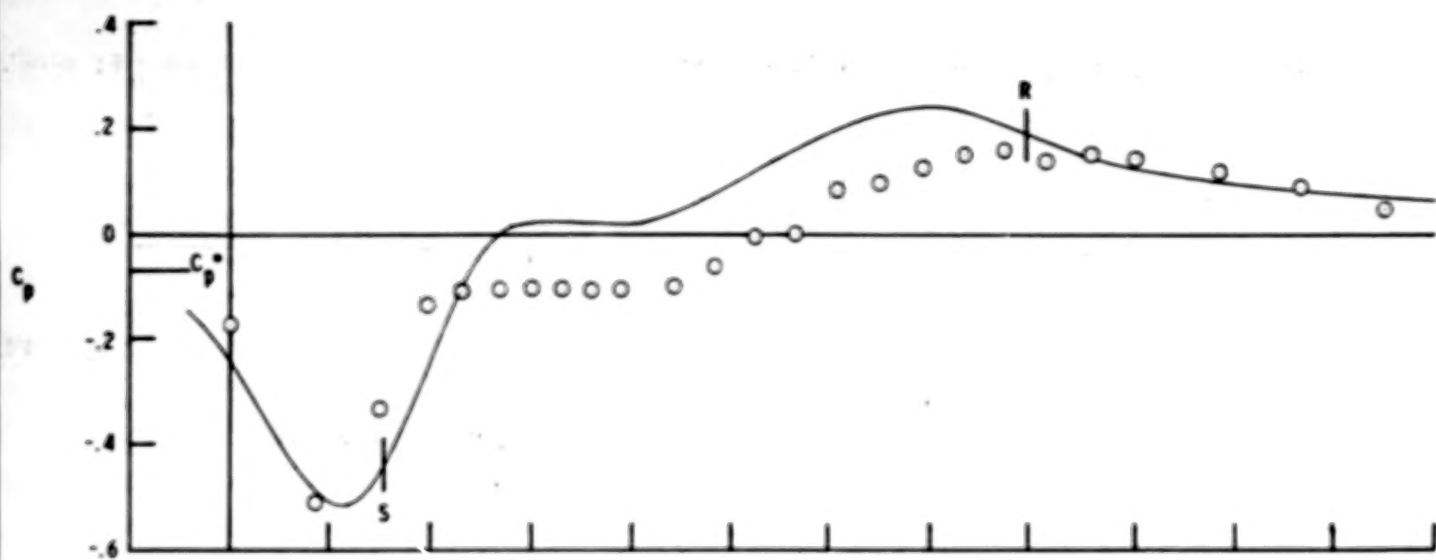
(h) $M_\infty = 0.96$.

Figure 13.- Concluded.

61.
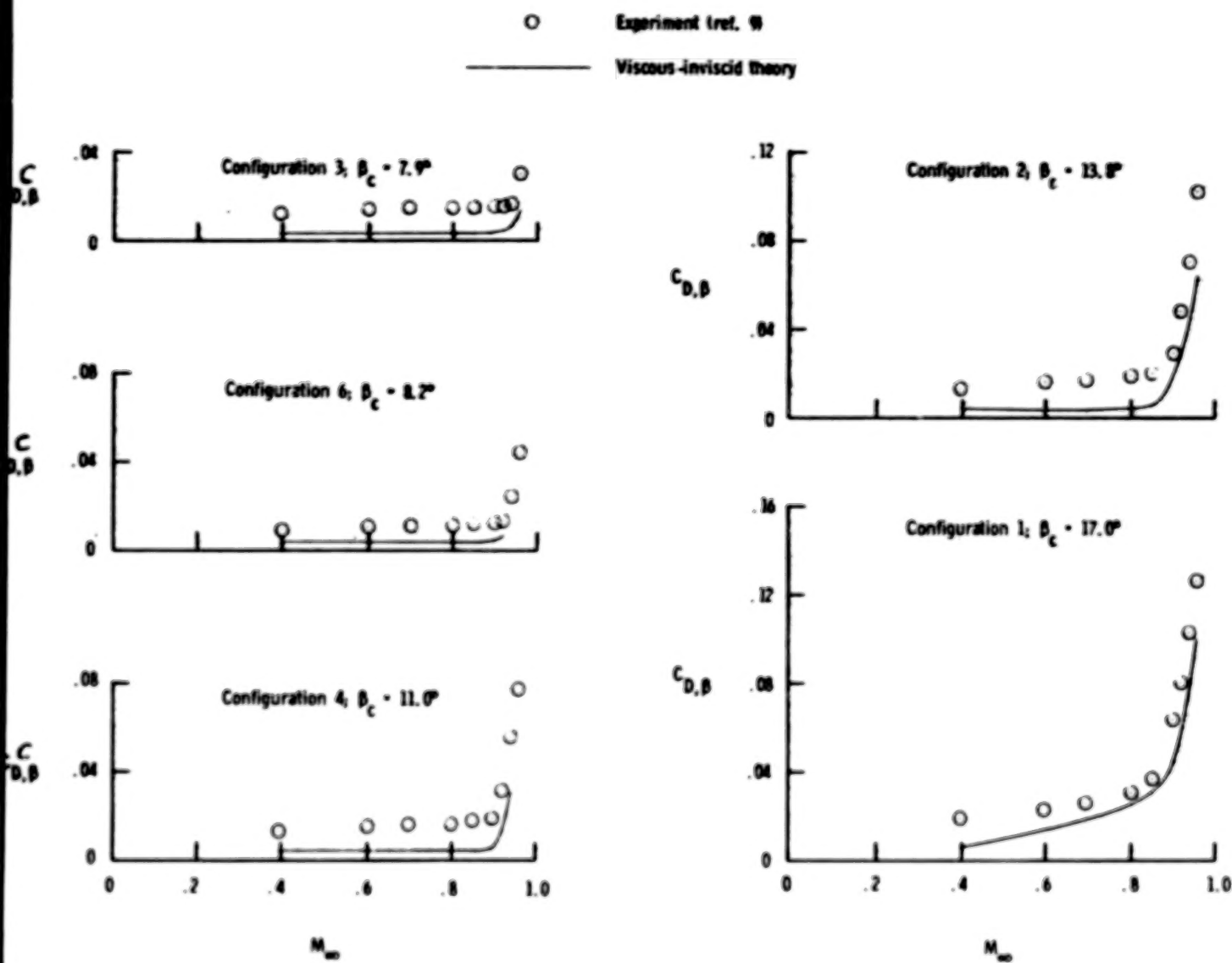
Figure 14.- Variation of theoretical and experimental total pressure drag with free-stream Mach number.
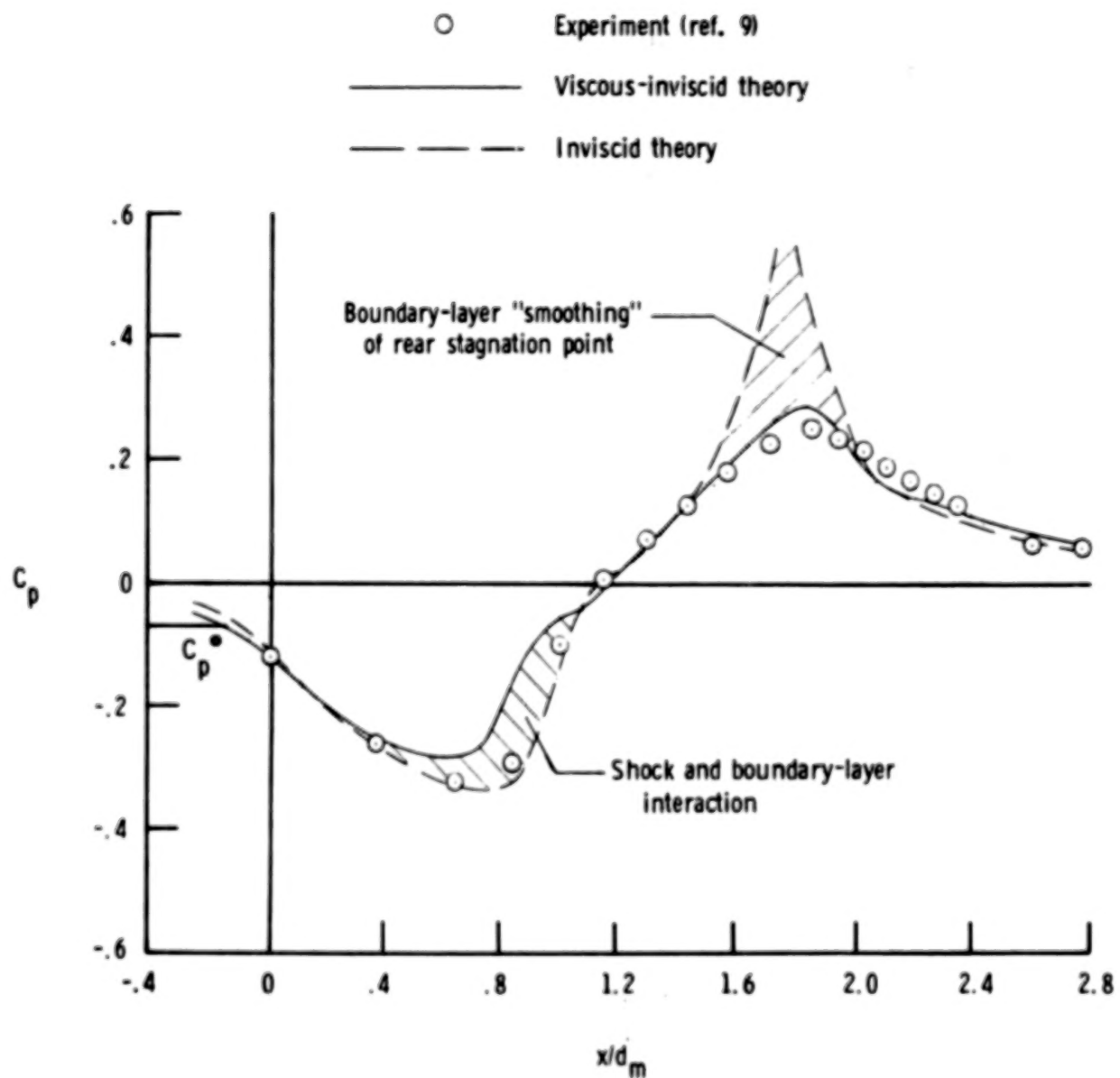
Figure 15.- Effect of viscous-inviscid interaction near shock and boattail-simulator juncture. Configuration 3; $M_\infty = 0.96$.

1. Report No. NASA TP-1070	2. Government Accession No.	3. Recipient's Catalog No.
4. Title and Subtitle COMPUTATION OF TRANSONIC BOATTAIL FLOW WITH SEPARATION		5. Report Date December 1977
		6. Performing Organization Code
7. Author(s) Richard G. Wilmoth		8. Performing Organization Report No. L-11669
9. Performing Organization Name and Address NASA Langley Research Center Hampton, VA 23665		10. Work Unit No. 505-04-11-01
		11. Contract or Grant No.
12. Sponsoring Agency Name and Address National Aeronautics and Space Administration Washington, DC 20546		13. Type of Report and Period Covered Technical Paper
		14. Sponsoring Agency Code

15. Supplementary Notes

16. Abstract

The relaxation procedure of South and Jameson for the full potential transonic flow equation has been coupled to a modified Reshotko-Tucker integral boundary-layer technique with an empirical model for separated flow. The viscous and inviscid flows are solved iteratively until convergence is obtained. This iterative method has been applied to the subsonic and transonic flow over a series of axisymmetric circular-arc boattails with solid jet plume simulators. Comparisons of theoretical and experimental surface pressures and boattail drag are presented over a free-stream Mach number range of 0.40 to 0.96. Measured and predicted pressures agree well for Mach numbers below 0.90. This numerical method correctly predicts the qualitative variation of boattail drag with free-stream Mach number and boattail angle well into the region of transonic drag rise although it significantly underpredicts the absolute drag levels. For separated flows, the empirical discriminating streamline model gives good results up to a free-stream Mach number of about 0.90 and allows reasonable predictions for shock-induced separation if the proper separation location and separation turning angle are known.

17. Key Words (Suggested by Author(s)) Boattail drag Transonic flow Separated flow Viscous-inviscid interactions	18. Distribution Statement Unclassified – Unlimited Subject Category 02		
19. Security Classif. (of this report) Unclassified	20. Security Classif. (of this page) Unclassified	21. No. of Pages 63	22. Price* $5.25